Title
Constraints on slow slip from landsliding and faulting

Permalink
https://escholarship.org/uc/item/1dv2x1sk

Author
Delbridge, Brent Gregory

Publication Date
2017

Constraints on slow slip from landsliding and faulting

By

Brent Gregory Delbridge

A dissertation submitted in partial satisfaction of the

requirements for the degree of

Doctor of Philosophy

in

Earth and Planetary Science

in the

Graduate Division

of the

University of California, Berkeley

Committee in charge:

Professor Roland Bürgmann, Chair
Professor Bruce Buffett
Professor Philip Marcus

Fall 2017

Constraints on slow slip from landsliding and faulting

Abstract

Constraints on slow slip from landsliding and faulting

by

Brent Gregory Delbridge

Doctor of Philosophy in Earth and Planetary Science

University of California, Berkeley

Professor Roland Bürgmann, Chair

The discovery of slow-slip has radically changed the way we understand the relative movement of Earth's tectonic plates and the accumulation of stress in fault zones that fail in large earthquakes. Prior to the discovery of slow-slip, faults were thought to relieve stress either through continuous aseismic sliding, as is the case for continental creeping faults, or in near instantaneous failure. Aseismic deformation reflects fault slip that is slow enough that both inertial forces and seismic radiation are negligible. The durations of observed aseismic slip events range from days to years, with displacements of up to tens of centimeters. These events are not unique to a specific depth range and occur on faults in a variety of tectonic settings. This aseismic slip can sometimes also trigger more rapid slip somewhere else on the fault, such as small embedded asperities. This is thought to be the mechanism generating observed Low Frequency Earthquakes (LFEs) and small repeating earthquakes.

I have preformed a series of studies to better understanding the nature of tectonic faulting which are compiled here. The first is entitled "3D surface deformation derived from airborne interferometric UAVSAR: Application to the Slumgullion Landslide", and was originally published in the Journal of Geophysical Research in 2016. In order to understand how landslides respond to environmental forcing, we quantify how the hydro-mechanical forces controlling the Slumgullion Landslide express themselves kinematically in response to the infiltration of seasonal snowmelt. The well-studied Slumgullion Landslide, which is 3.9 km long and moves persistently at rates up to ∼2 cm/day is an ideal natural laboratory due to its large spatial extent and rapid deformation rates. The lateral boundaries of the landslide consist of strike-slip fault features, which over time have built up large flank ridges.

The second study compiled here is entitled "Temporal variation of intermediate-depth earthquakes around the time of the M9.0 Tohoku-oki earthquake" and was originally published in Geophysical Research Letters in 2017. The temporal evolution of intermediate depth seismicity before and after the 2011 M 9.0 Tohoku-oki earthquake reveals interactions between plate interface slip and deformation in the subducting slab. I investigate seismicity rate changes in the upper and lower planes of the double seismic zone beneath northeast

Japan. The average ratio of upper plane to lower plane activity and the mean deep aseismic slip rate both increased by factor of two. An increase of down-dip compression in the slab resulting from coseismic and postseismic deformation enhanced seismicity in the upper plane, which is dominated by events accommodating down-dip shortening from plate unbending.

In the third and final study included here I use geodetic measurements to place a quantitative upper bound on the size of the slow slip accompanying large bursts of quasi-periodic tremors and LFEs on the Parkfield section of the SAF. We use a host of analysis methods to try to isolate the small signal due to the slow slip and characterize noise properties. We find that in addition to subduction zones, transform faults are also capable of producing ETSs. However, given the upper-bounds from our analysis, surface geodetic measurements of this slow slip is likely to remain highly challenging.

For my family

Contents

Acknowledgments

It takes a village to raise a child, and I am incredibly grateful for the guidance, insight and help I received during my scientific adolescence and development at UC Berkeley.

First and foremost, I want to thank my advisor, Roland Bürgmann. Roland is a scientist of incredible breadth and contains a depth of knowledge that I was only able to glimpse the surface of. Luckily for him, deadlines exist, else I would have happily mined his brain, and worked with him for as long as I was given the honor. In addition to his ability to tackle scientific problems, Roland has an incredible efficiency that has set the bar for how to balance family, the well-being of his students and post-docs, teaching, and writing grants, while simultaneously pursuing his own research agenda. When I called upon him in moments of desperation and pleaded, “Help me Roland Wan Kenobi, you’re my only hope”, he responded “We will get this droid to Alderaan”, every time. All the mistakes I made along the way were of my own doing, and I can’t thank him enough for allowing me the freedom to make them.

I would like to thank Bruce Buffett for freely giving so much of his time and expertise. Bruce has a canny ability to take a complicated problem and boil it down to its component atoms, and get to heart of the physical process that is important. I am forever indebted to him for teaching me how to simplify a set of mathematical equations to a set of scientific and physical insights, or more simply, thank you for teaching me fluid mechanics.

I would like to thank to Michael Manga, who taught me so many things about science, academia, and what it means to be a professional scientist. I would like to thank him for allowing me to follow oddball ideas in his laboratory, including both shooting metal balls using compressed air into sand to understand observations of volcanic bomb sags on Mars, and using insane amounts of gelatin to understand the ascension processes of volcanic dikes, but most importantly, for teaching me how these can be made valuable scientific contributions.

Thanks furthermore to Philip Marcus and David Brillinger for teaching me about fluid instabilities and the statistics of timeseries respectively. Thanks to Eric Fielding for teaching me to process Interferometric Synthetic Aperture Radar, and for kindly hosting me at the Nasa Jet Propulsion Laboratory. I would like to thank Heidi Houston who introduced me to seismology, this document certainly wouldn’t have existed without her insistence and support that began years ago at the Univ. of Washington, and whose mentorship has continued over the years. I would also like to thank Ken Creager for allowing me to join him and hike in

the Olympic Mountains to install seismometers for the “Array of Arrays Experiment” at the very beginning.

I want to thank Ian, David, Pam, Danielle, Amanda, Seth, Tushar, Noah, Jesse, Chris, Katherine, Mong-han, and, Chelsea, for being both colleagues and friends. Thanks to Paul for encouraging me to convert from Physics to Earth Science at UW so many years ago, and for the annual AGU traditions since. Thanks to Kristina and Sonny for supporting me, and sometimes carrying me, for so many years. Thanks to Tripti for teaching how to be kind to myself, and how to be a human in science, I can’t tell you how much you’ve taught me. Thanks to Joe for being my friend and family, I can’t imagine living in Berkeley without you. Thanks to Erik, one of my oldest friends, and constant lifeline, I can’t thank you enough. Thanks to Anthony and Matt, for without our innumerous games of chess, I would have surely lost my mind. Thanks to Cory, Collin, Carley, Kalie, Brandon, Allyson, and Cody, I can’t imagine having survived without your support and encouragement from afar. Thanks to Caroline, Inaki, Leah, and Greg for adopting me into the Carleton family, your kindness and friendship are without measure. There are so many names not included here that should be, please know that I could not be more grateful. Finally, my family has been an unending source of unconditional love and support. Mom, Dad, and Grant, I would not be here without you. Thank you.

Chapter 1

3D surface deformation derived from airborne interferometric UAVSAR: Application to the Slumgullion Landslide

1.1 Abstract

In order to provide surface geodetic measurements with “landslide-wide” spatial coverage we develop and validate a method for the characterization of 3D surface deformation using the unique capabilities of the UAVSAR airborne repeat-pass radar interferometry system. We apply our method at the well-studied Slumgullion Landslide, which is 3.9 km long and moves persistently at rates up to $\sim 2\ cm/day$. A comparison with concurrent GPS measurements validates this method and shows that it provides reliable and accurate 3D surface deformation measurements. The UAVSAR-derived vector velocity field measurements accurately capture the sharp boundaries defining previously identified kinematic units and geomorphic domains within the landslide. We acquired data across the landslide during spring and summer and identify that the landslide moves more slowly during summer except at its head, presumably in response to spatiotemporal variations in snow melt infiltration.

In order to constrain the mechanics controlling landslide motion from surface velocity measurements, we present an inversion framework for the extraction of slide thickness and basal geometry from dense 3D surface velocity fields. We find that that the average depth of the Slumgullion Landslide is 7.5 meters, several meters less than previous depth estimates.

We show that by considering a visco-plastic rheology we can derive tighter theoretical bounds on the rheological parameter relating mean horizontal flow rate to surface velocity. Using inclinometer data for slow-moving, clay-rich landslides across the globe we find a consistent value for the rheological parameter of 0.85 ± 0.08.

1.2 Introduction

In order to measure landslide response to environmental forcing we utilize the unique capabilities of the Uninhabited Aerial Vehicle Synthetic Aperture Radar (UAVSAR) airborne repeat-pass SAR interferometry system to provide surface geodetic measurements with "landslide-wide" spatial coverage. Deformation measurements provided by the UAVSAR system have advantages over space-based Interferometric Synthetic Aperture Radar (InSAR) measurements in that the user can adapt acquisition plans to the desired target with optimal imaging geometries, and temporal sampling. Unlike spaceborne InSAR, the UAVSAR system is not restricted to fixed viewing geometries and repeat times constrained by satellite orbit. Our observations obtained using the UAVSAR system complement ongoing survey-mode measurements of 19 GPS sites and in situ observations of pore pressure and atmospheric parameters acquired by the U.S. Geological Survey (USGS) (Schulz et al., 2007; Coe et al., 2003; Schulz et al., 2009b,a; Coe, 2012). These ground-based measurements have a limited spatial coverage, which does not enable characterization of the landslide-wide behavior and response to forcing by precipitation and snowmelt.

We develop and validate a new imaging technique to take full advantage of the unique airborne-geodetic UAVSAR system capabilities. We combine four look directions chosen based on the landslide geometry and invert for the full 3D landslide-wide surface deformation. We test, validate, and estimate the noise of the obtained displacement field by comparing our results with GPS measurements acquired during overlapping time periods. After validation, we examine the changes of the 3D velocity field between three week-long acquisitions during snowmelt in the spring and summer of 2012. We quantify how distinct domains of a landslide interact with each other and respond to hydrologic perturbations, and evaluate how the kinematics of the entire landslide changes over the course of a water year.

To highlight the advantage of the "landslide-wide" spatial coverage provided by InSAR we develop a method for inverting landslide thickness and basal geometry from kinematic observations. The imaging and inversion methods presented here provide a future tool for the rapid characterization of landslide hazards by quickly giving rough estimates of landslide deformation rates, volume and geometry.

1.3 Study Site and Motivation: The Slumgullion Landslide

The Slumgullion Landslide is deep-seated ($> 5m$ depth) and slow-moving ($\sim cm/day$); its persistent movement for $\sim 300 yrs$ (Varnes and Savage, 1996) has resulted in a geomorphic form often referred to as an "earthflow" (e.g. Keefer and Johnson, 1983). However, Slumgullion primarily moves by sliding along discrete, bounding and internal shear surfaces (e.g. Varnes and Savage, 1996; Fleming et al., 1999; Coe et al., 2009) so is properly classified as a slide (Cruden and Varnes, 1996). Slumgullion and similar landslides, which are sometimes referred to as earthflows (e.g. Keefer and Johnson, 1983; Iverson and Major, 1987; Mackey and Roering, 2011; Handwerger et al., 2013), are primarily composed of fine-grained materials which macroscopically exhibit a plastic or visco-plastic rheology (e.g. Keefer and Johnson, 1983; Iverson and Major, 1987). Slumgullion is composed of Tertiary volcanic rocks mostly derived from andesitic lava flows nearly completely altered by acid-sulfate hydrothermal reactions, which converted the primary minerals of plagioclase and biotite to clays composed of kaolinite and smectite and iron-rich potassium sulfate minerals such as alunite and jarosite (Diehl and Schuster, 1996). These clay minerals, which make up most of the landslide material, have a medium to high plasticity and high swelling potential (Chleborad et al., 1996).

The persistent rapid deformation rates of $2cm/day$ and the large spatial extent $(1.46km^2)$ of Slumgullion make it ideal to study the complex interaction of different kinematic elements and the underlying mechanics. The currently active portion of the landslide has been deforming for the past 300 years (Fleming et al., 1999) with total displacements on the order of several hundred meters (Coe et al., 2003). The slide sits on top of an older, inactive landslide deposit dated to have failed catastrophically $\sim$ 700 years ago (Crandell and Varnes, 1960a,b). This catastrophic failure dammed the Lake Fork of the Gunnison River forming the second largest natural lake in Colorado, Lake San Cristobal. The older inactive deposit is 6.8 km long, 400 m wide, and the depth is estimated from seismic reflection and refraction surveys to be $\sim$ 100 m (Williams and Pratt, 1996). The currently active portion of Slumgullion is $\sim 3.9km$ long, $\sim$ 300 m wide and has an average depth of $\sim$ 13 m based on extrapolation of observations of the toe thickness and several point-velocity measurements using a flux calculation (Parise and Guzzi, 1992). Schulz et al. (2012) used detailed maps of the landslide(Fleming et al., 1999) and ∼300 displacement measurements (Smith, 1993) to discretize it into 11 kinematic units separated by narrow fracture, fold, and fault zones. The upper portion of the landslide is in extension as indicated by normal faults and tension cracks (Figure 1.1. Kinematic units 1-5 containing GPS monitoring points 2-7), and the lower part is in contraction as indicated by thrust faults (Figure 1.1. Kinematic units 10-11 containing GPS monitoring points 17-19). The lateral boundaries of the landslide consist of strike-slip fault features, which over time have built up large flank ridges.

The relatively steady movement of Slumgullion from year to year Coe et al. (e.g. 2003) and exposed striated low-permeability clay layers suggest that it may be hydrologically isolated from the surrounding host material (Baum and Reid, 2000; Baum et al., 2003). This idea is consistent with some well-log data from similar landslides showing that the thickness extends from the ground surface to the top of the unweathered rock beneath, where there is an abrupt decrease in permeability and reduction in water content (Swanson and Swanston, 1977; Trotter, 1993). However, other studies identified basal shear surfaces well above underlying bedrock in trenches and boreholes (Keefer and Johnson, 1983; Iverson and Major, 1987). Coe et al. (2003) performed periodic surveys of surface monuments distributed across the landslide and hourly monitoring at two locations for displacement, air and soil temperature, snow depth, rainfall, soil-water content, and groundwater pressures. They found that the landslide deformed throughout the year, but that the surface velocity varied seasonally, with the landslide accelerating in spring and decelerating in summer, correlated with the infiltration of snowmelt. Numerous studies have shown that this seasonal acceleration and deceleration is governed by variations in water content and pore-water pressures from infiltration of precipitation and other groundwater supply variations (e.g. Iverson and Major, 1987; Malet et al., 2002). The persistent movement of the Slumgullion Landslide at speeds that respond to variations in pore-water pressure implies that it and similar slides remain close to their failure threshold. Schulz et al. (2009b) confirmed that the Slumgullion Landslide accelerated with increased pore-water pressure over daily time scales within the landslide body, but also observed that pore pressure decreased along the margins, possibly in response to accelerated shear-induced soil dilation. The decreased pore-water pressures increase the effective stress and cause the landslide to decelerate, suggesting a cycle of dilatant strengthening and pore-pressure feedback (Schulz et al., 2007).

In this study, we explore how the hydro-mechanical processes such as seasonal snowmelt that influences the motion of the Slumgullion Landslide Coe et al. (e.g. 2003); Schulz et al. (e.g. 2007, 2009b) are kinematically expressed. We examine how the long-term stability of basal, lateral and internal boundaries is reflected in the surface flow kinematics.

1.4 Instruments and Data

1.4.1 UAVSAR Interferograms

The NASA/JPL UAVSAR airborne repeat-pass SAR interferometry system is flown aboard a NASA Gulfstream III and is capable of acquiring L-Band (24 cm wavelength) SAR images with a resolution of 1.9 m in range and 0.8 m in the azimuth direction (Hensley et al., 2009b). In this study, we utilize the standard UAVSAR multi-looked slant-range products with 3 looks in range and 12 in azimuth, resulting in a spatially averaged pixel spacing of 5.7 m in range and 9.6 m in azimuth. The UAVSAR system was designed with two primary foci: 1) providing repeat-pass radar interferometry at a variety of timescales and optimal imaging geometries in order to provide precise measurements of Earth's surface deformation, and 2) making fully polarimetric SAR observations for measurements of vegetation structure and other aspects of the surface characteristics. In order to provide accurate repeat-track InSAR images, the NASA aircraft uses a Precision Autopilot (Lee et al., 2007) with real-time differential GPS that permits repeats of flight paths within a 10 m diameter tube, and typically achieves a repeat-track baseline of less than 5 m (Hensley et al., 2009b). Additionally, an electronically steered antenna uses real-time attitude-angle measurements to compensate for the changes in the aircraft yaw from flight to flight and during flights. This is necessary to mitigate variations in the Doppler centroid that could well exceed the azimuth beamwidth overlap required in the antenna look direction for repeat-track interferometry. Key radar parameters for the UAVSAR system can be found in Hensley et al. (2009b). In addition to selecting the processing parameters for motion alignment to ensure co-alignment in the along-track and cross-track directions in the generation of single look complex (SLC) images, UAVSAR SLCs require an additional data-driven (Hensley et al., 2009a) baseline correction to provide accurate estimates of the deformation on the scale of millimeters. We used the interferograms after applying this additional empirical baseline correction.

During the image formation process, a digital elevation model (DEM) is needed due to the wide beam (along-track beam width is 8°) that precludes using simple motion compensation schemes employed for some SAR systems. A byproduct of this focusing is that the topographic phase component is effectively removed from the data during processing. However, the radar line-of-sight to each pixel is not output directly, and moreover if the line-of-sight were output it would be in a sensor centric system that would need to be converted to a geographic-based coordinate system. Therefore, we ran an additional program using the same DEM used for motion compensation, usually a shuttle radar topography mission (SRTM) derived DEM (Van Zyl, 2001), and information about the flight trajectory to compute the line-of-sight vector at imaging time needed for inverting for the 3D deformations.

The traditional "integrated correlation and unwrapping" (ICU) method (ICU is an enhanced version of the traditional residue-based unwrapper (Goldstein et al., 1988) that uses phase gradients, amplitude values and coherence masking to guide unwrapping using multiple starting seed pixels (Buckley et al., 2000)) was used to produce the UAVSAR data products. The ICU program automatically seeds a zero-phase reference pixel; therefore, in order to remove the constant reference-phase offset of the UAVSAR interferograms we determine a constant reference velocity (phase divided by the interferogram interval) to subtract from the UAVSAR-derived 3D velocity images using known stationary GPS control points following the methods described in Delbridge et al. (2015).

In 2012, the UAVSAR system made six flights and acquired three pairs of interferometric measurements each spanning approximately 1 week (Figure 1.2); based on the previous work of Milillo et al. (2014), the temporal separation was chosen to maximize the landslide deformation between acquisitions while still maintaining high pixel coherence. For each flight, we acquired SAR images along four independent flight lines bounding the Slumgullion Landslide in order to acquire deformation along four look directions, from which we were able to form 11 interferograms and three temporal sets of velocity observations (Tables 1.1 and S1). Due to an error with the data logging system during the acquisition of flight line 21501 in July 2012 no usable data were recorded, allowing only 11 rather than 12 interferograms to be formed. The flight time of each individual data acquisition is roughly 2.5 minutes for each of the four Slumgullion flight lines. The full list of the UAVSAR interferograms used in this study can be found in Table S1. The flight line geometries were chosen such that lines 03501 and 21501 are sensitive to the landslide's slope-perpendicular motion, and lines 12502 and 30502 are sensitive to the downslope motion. For slow-moving landslides, the majority of the deformation is slope parallel, sliding under the force of gravity, so we expect the largest displacements should be seen in lines 12502 and 30502 (Table 1.2). Figure 1.3 shows the geometry and image footprints of the four flight lines for each of the line-of-sight (LOS) observations acquired at the Slumgullion Landslide.

We take the timestamp at the beginning of each acquisition to calculate the duration of time between each pair of images used to form the resulting interferogram. In order to calculate the LOS velocity from the unwrapped LOS interferograms, we first fit and subtract a plane from the image to remove phase-ramp residuals that arise from residual baseline errors. We then normalize the phase from each interferogram to a common time interval to account for differences in the time duration spanned by each of the four interferograms formed from their respective flight lines.

Figure 1.4 shows the UAVSAR-derived LOS velocity for each of the four look directions acquired in April 2012. Negative values (blue colored pixels) indicate shortening along the LOS direction. As expected, we see larger signals in lines 12502 and 30502, with LOS velocities exceeding 1 cm/day, and we also identify the landslide in lines 21501 and 03501 despite smaller LOS deformation. In Figure 1.4, black pixels denote masked regions with coherence values less than 0.3. Note that these pixels are only masked for plotting purposes and are not masked during the 3D vector inversion.

1.4.2 GPS Measurements

In July 1998, the USGS installed 19 monitoring points and 11 control points around and across the active portion of the Slumgullion Landslide, a subset of which is shown in Figure 1.1. Throughout this study, we will consider the horizontal velocity to be the combined East and North components of the velocity fields, due to the low slopes at the Slumgullion Landslide this velocity is approximately equal to the velocity in the plane of the surface normal. Each point consists of a monument constructed from rebar and an aluminum cap. The locations of the monitoring points were chosen to capture the key structural features of the landslide (Coe et al., 2003). Measurements of the monitoring and control points were completed annually during each summer from 1998 to 2012 (Coe, 2012). In 2012, the USGS performed six rapid static surveys overlapping with the Slumgullion UAVSAR acquisitions (Figure 1.5). The average horizontal velocity magnitude estimates for each measurement spans approximately 10 days and are reported in Table 1.3; April 10th-23rd is shown in orange, May 10th-18th is shown in green, and July 23rd-August 2nd is shown in blue. The largest velocities are observed in the landslide “neck” [defined by Fleming et al. (1999)] where the slide is the steepest and narrowest. The landslide velocity steadily increases as the snow within each region begins to melt; the toe responds first with its fastest motions in April, whereas the higher-altitude regions within the upper body and head have their fastest motions in May. Comparing the 2012 week long velocity measurements with the long-term average estimates spanning 1998-2002 shown in Figure 1.5, we can see that while there has been an overall reduction in the velocity of the slide, the largest reductions are in the body, whereas the motions in the toe and head exhibit smaller changes in rate.

1.5 Methods

1.5.1 Three-Dimensional Vector Deformation Inversion

To obtain the full 3D vector displacement field we combine the LOS measurements from the four flight lines shown in Figure 1.3. The LOS vector is then estimated for each pixel using a DEM for the region and the acquisition flight parameters and geometry. The covariance for the line-of-sight displacement for each pixel is estimated from the interferometric coherence data, and we perform a least squares inversion for the 3D displacement. The desired displacement vector is expressed in terms of the natural physical coordinates North, East, and Up. Mathematically, we express this displacement vector($\vec{d}$) as a linear combination of our basis vectors($\hat{e}_i$):

$$\vec{d} = \sum_{i=1}^{3} d_i \hat{e}_i = \sum_{i=1}^{3} \langle \vec{d}, \hat{e}_i \rangle \hat{e}_i. \tag{1.1}$$

For each LOS measurement (o_j), we observe the true vector projected onto the LOS direction (l_j), $o_j = \langle \vec{d}, \hat{l}_j \rangle$ so using Equation 1.1 above we can write,

$$\langle \vec{d}, \hat{l}_j \rangle = \sum_{i=1}^{3} d_i \langle \hat{e}_i, \hat{l}_j \rangle. \tag{1.2}$$

Thus, the sensitivity of the i^{th} component of the deformation on each LOS observation (o_j) can be expressed as,

$$\frac{\partial o_j}{\partial d_i} = \langle \hat{l}_j, \hat{e}_i \rangle. \tag{1.3}$$

The set of observations (o_j) can now be written in matrix form and is formulated as a classical least squares problem for each pixel

$$\vec{o} = A\vec{d}, \tag{1.4}$$

where $\vec{o}$ ($Nx1$) is the “observation” vector whose elements correspond to the phase measurement associated with each viewing geometry at that pixel. In this inversion, we use the four LOS measurements ($N = 4$) shown in Figure 1.3; in general this inversion scheme is valid for N greater than or equal to three individual viewing geometries. The components of the model matrix A ($Nx3$) are the different LOS vectors ($\hat{l}_j$) projected onto the corresponding basis vectors ($\hat{e}_i$), and given by

$$A = \begin{bmatrix} \langle \hat{l}_1, \hat{e}_1 \rangle & \langle \hat{l}_1, \hat{e}_2 \rangle & \langle \hat{l}_1, \hat{e}_3 \rangle \\ \vdots & \vdots & \vdots \\ \langle \hat{l}_N, \hat{e}_1 \rangle & \langle \hat{l}_N, \hat{e}_2 \rangle & \langle \hat{l}_N, \hat{e}_3 \rangle \end{bmatrix}. \tag{1.5}$$

The solution to this classical least squares problem (Equation 1.4) yields the desired displacement vector d and is given by:

$$\vec{d} = \left(A^t Q^{-1} A \right)^{-1} A^t Q^{-1} \vec{o}, \tag{1.6}$$

where Q is the estimated covariance matrix and is calculated from the interferometric pixel correlation using the Cramer-Rao bounds derived in Rodriguez and Martin (1992). Interferometric correlation is an estimate of the interferometric coherence.

$$Q = \frac{\lambda}{4\pi}\sqrt{\frac{1-\gamma^2}{2N_L\gamma^2}}\mathbf{I}, \tag{1.7}$$

where λ the radar wavelength, and γ is the pixel correlation.

This method also produces a formal covariance matrix for the estimated vector displacement given by:

$$cov_{\vec{d}} = \left[A^t Q^{-1} A\right]^{-1}. \tag{1.8}$$

The vector deformation variance is then the diagonal of the formal covariance matrix given above (Equation 1.8), and the corresponding velocity errors for each component (σ_i) are given as the square root of the deformation variance divided by the time duration spanned by the measurement (T)

$$\sigma_i = \frac{\sqrt{diag[cov_{\vec{d}}]_i}}{T}, \tag{1.9}$$

and the corresponding error for the horizontal velocity magnitude is given by:

$$\sigma_H = \sqrt{\frac{u_{east}^2 * \sigma_{east}^2 + u_{north}^2 * \sigma_{north}^2}{u_{east}^2 + u_{north}^2}}. \tag{1.10}$$

These formal error estimates derived from the inversion covariance are taken as a lower bound for the actual error present in the results of the 3D vector inversion.

1.6 Results

1.6.1 3D Velocity Inversions

Figures 2.3-1.8 show the results of the 3D vector inversions of the four April 2012 LOS images shown in Figure 1.4 in units of *cm/day*. Figure 2.3 shows spatial maps of the magnitude of each inverted velocity component (East, North and Up) and Figure 2.4 shows the corresponding error estimated from the formal covariance matrices produced by the 3D vector inversion (Section 4.1). Figure 1.8 shows the total velocity, with magnitudes within the landslide ranging from 0 to 2 *cm/day*. The black pixels represent regions of large covariance in the inversion, and have estimated errors greater than 1 millimeter per day. The inset in the top left corner of Figure 1.8, shows a close-up of a deformation feature, which we denote as the "mini-slide." This mini-slide corresponds to an isolated region of rapid deformation associated with a region of steep slope within the deforming landslide mass (up-slide of GPS monitoring site MP15, Figure 1.1). Figures 1.9 and 1.10 show the horizontal velocity and estimated horizontal error for all three sets of UAVSAR measurements in April, May and July. The the individual component results corresponding to Figures 2.3 and 2.4 for May 2012 and July 2012 are included in the supplement (Figures S1-S4).

The over-determination of three displacement components from four independent LOS observations in the inversion enables us to reduce the atmospheric noise, which is crucial to obtain a robust vertical deformation. In the horizontal directions, we see that the landslide motion is clearly imaged and well above the background noise (Figure 2.3). The vertical component is smaller in comparison due to the gradual slope of the landslide (average 8°) and is most pronounced in the steep and fast portions of the slide, but hard to visually extract from the atmospheric noise near the toe and source regions. Atmospheric noise may dominate the slow-moving vertical velocity measurement, and thus the formal covariance estimates should be considered a lower bound since they only include phase noise estimated from the interferometric coherence and not systematic phase errors associated with atmospheric conditions.

The mean vertical velocity within the landslide is (defined by the red line in Figure 1.1) $-0.1 \pm 0.09\ cm/day$ whereas the mean velocity of the surrounding region is $0.08 \pm 0.22\ cm/day$. In order to test the hypothesis that the vertical signal we observe within the boundary of the Slumgullion Landslide is not statistically different from the noise in the area surrounding the landslide, we perform a Welch's T-Test to determine whether the two mean velocities measured are significantly different and compute the Kolmogorov-Smirnov statistic to determine if the two sets of measured velocities are sampled from the same distribution. We obtain a T-statistic of -314.34 with a corresponding P-value negligibly from zero ($< 10^{-20}$), and a Kolmogorov-Smirnov statistic of 0.53 with a corresponding P-value negligibly from zero ($< 10^{-20}$); both statistical measures strongly reject our hypothesis that the vertical signal observed is indistinguishable from the noise in the surrounding region. Many areas outside the landslide have dense forest cover and low coherence, which causes greater uncertainties in the velocities in those areas as shown in Figure 2.4.

If the motion of the slide is driven solely by gravity, we expect it to be in the downslope direction (Figure 1.9, black arrows calculated from a 1/3 arcsecond DEM over a radius of 50 meters around each GPS monitoring point). Excluding the head and toe regions where the slide velocity is low, and sites near the lateral boundaries, the velocities from InSAR and GPS agree well and align with the downslope direction (Figure 1.9). While there is no clear indication for a correlation between the slope at each individual pixel and the magnitude of its velocity, there is a nearly linear relationship between the median slope of each kinematic unit and the magnitude of the unit's median horizontal velocity (linear regression with a slope of $0.22 \pm 0.03\ cm/day/degree$ and an R^2 of 0.50, and a corresponding P-value of $1.27 * 10^-4$, Figure 1.11).

We estimate the expected geometrical component of the vertical velocity due solely to downslope sliding by estimating the vertical velocity that is consistent with the slope and measured horizontal velocity at each pixel. We calculate the median vertical velocity we would nominally expect from our measured horizontal motion sliding downslope to be $-0.10 \pm 0.07\ cm/day$, nearly identical to the measured vertical velocity, and the sign is consistent with compression downslope from the “hopper” [defined by Fleming et al. (1999)] through the neck to the toe. The median vertical motion within the slide not attributed to downslope motion is less than a millimeter a day (median velocity difference of 0.00 ± 0.09 cm/day). The measured vertical velocity also accurately captures small-scale features such as the mini-landslide, a region of accelerated slope failure on top of the larger active portion of the slide (Figure 2.3).

The April and May velocity maps (Figure 1.9 top and middle panels) show the spring deformation, which is expected to be faster than during other periods due to infiltration of water from snowmelt. The July velocity map (Fig 1.9 bottom panel) illustrates the summer deformation, which is expected to be smaller given lower levels of precipitation. We confirm this acceleration of the slide during spring, with the mean horizontal velocity of each kinematic unit composing the body of the landslide (kinematic units five through nine) achieving their greatest velocities in April and slowing through July from a mean velocity of 0.91 ± 0.26 cm/day to 0.82 ± 0.23 cm/day.

During the spring and summer it is typical for the Slumgullion Landslide to experience highly localized rainstorms. On May 8th, a rain gauge at the landslide measured 9 millimeters of precipitation within 24 hours (Figure 1.2). There were also high levels of rainfall prior to the April 16th - April 23 and July 24 - August 1 UAVSAR measurements of 4 mm and 8.5 mm, respectively, that did not result in low coherence and correspondingly large estimated formal errors (EQ 1.10, Figure 1.10). It is possible that the UAVSAR coherence is not responding to the cumulative rainfall precipitation prior to or between UAVSAR acquisitions but rather is responding to the change in soil moisture resulting from temporal variations in precipitation levels.

While there was little rainfall during the May UAVSAR measurement ($\sim$ 0.25 mm), the rainfall during the April and July UAVSAR measurements ($\sim$ 2 mm and $\sim$ 8mm, respectively) was comparable to the rainfall prior to the UAVSAR measurements. Since the clays that compose the landslide are highly expansive, it is thought that the near-surface material of the landslide swelled by the May 9th UAVSAR acquisition and dried and contracted by the time of the May 17th UAVSAR acquisition, causing a change in soil moisture and surface roughness that resulted in low coherence between the two UAVSAR acquisitions. It is likely that during the April and July 2012 UAVSAR measurements the clay remain saturated, and did not have an opportunity to dry and contract as it did during the May 2012 UAVSAR measurements.

This interpretation is consistent with the observation that the estimated errors from the pixel coherence do not depend on the absolute cumulative rainfall; the April and July measurements have similar estimated errors despite large differences in absolute cumulative precipitation values ($\sim$ 80 mm), while the April and May measurements have qualitatively different estimated errors for a much smaller change in cumulative precipitation ($\sim$ 15 mm).

These arguments about rainfall precipitation fail to explain the change in “off-slide” coherence, where expansive clays that compose the landslide are not present. We argue that the snow depth is a dominant environmental factor controlling surface reflectivity and UAVSAR coherence. The changes in snow depth during both the April and May UAVSAR measurements are ~ 25 *cm*, with the snow depth dropping to zero between the May 9th and May 17th UAVSAR acquisitions. The SNOTEL station recording the snow depth is located at the same elevation as the uppermost head of the Slumgullion Landslide, and we can assume that the snow depth measured there represents an upper bound on the snow depths at lower elevations such as the toe and body of the landslide. We suggest that in addition to changes in cumulative precipitation and snow depth, a pixel's binary switch from snow covered to snow free, alters the surface reflectivity and is a large contributor to the low coherence and large estimated errors present in the May 2012 UAVSAR measurements.

Due to low coherence, the May 2012 images failed to unwrap correctly across the center of the landslide where the deformation rates were the highest. In order to overcome the phase unwrapping problems, these interferograms were instead unwrapped using an algorithm based on reliability following a noncontinuous path (Delbridge et al., 2015). The low coherence (high covariance) during the May 2012 UAVSAR acquisitions is reflected in Figure 1.9 by the large number of black (masked pixels) within the landslide footprint. A comparison of the estimated covariances can be seen in Figure 1.10. Unfortunately, due to the low coherence and large possible contamination from swelling and differences in phase unwrapping we are unable to utilize the May 2012 inversion results in the subsequent depth inversion presented and performed in section 6.

1.6.2 Comparison with GPS data

Figure 1.9 shows a spatial comparison of the GPS- and UAVSAR-derived horizontal velocities (green and orange vectors, respectively) during the April, May, and July 2012 UAVSAR acquisitions (top, middle, and bottom panels, respectively). Figure 1.12 shows a component-by-component comparison of the GPS- and UAVSAR-derived velocity estimates for the three 2012 time periods. The solid black line represents a one-to-one agreement between the GPS and UAVSAR velocity estimates at location of the GPS monitoring sites. The dashed lines represent a velocity difference of 0.25 cm/day. Since most velocity estimates lie within these bounds, the absolute agreement between the measurements is within several millimeters a day. More precisely, fitting the East and North velocity components we find a linear correlation of 0.82 ± 0.007 with an R^2 of 0.60, an RMS from perfect agreement of 0.23 cm/day and a negligibly small P-value ($< 10^{-21}$). Similarly for the total horizontal magnitudes, we find a correlation of 0.99 ± 0.008 with an R^2 of 0.67, an RMS from perfect agreement of 0.22 cm/day and a negligibly small P-value ($< 10^{-21}$). The regression slope of ~ 1 shows that the inferred velocities statistically agree very well.

In addition to various sources of noise in the measured velocities, we expect some deviation from a perfect agreement due to the fact that the two measurements span slightly different times (Figure 1.2); the GPS measurement pairs were acquired on April 10 and 23, May 10 and 18, and July 23 and August 1, whereas the UAVSAR measurement pairs were acquired on April 16 and 23, May 9 and 17, and July 24 and August 1 (Figure 1.2).

During May 2012, the GPS-derived velocity measured at MP12 far exceeds both the 4 year (1998-2002) average speed reported by Coe et al. (2003) (Figure 1.5), and the UAVSAR-derived velocity (Figures 1.9 and 1.12), suggesting that the movement of MP12 may not be representative of the surrounding overall landslide behavior. The GPS derived velocities of monuments MP11 and MP12 were greatest in May 2012, whereas MP8 moved at its lowest rate in May 2012. In contrast, the UAVSAR derived velocities of kinematic units 5-9 all record their fastest motions in April 2012, with velocities slowly decreasing to July 2012. We also note that while the GPS point measurements show a complex relationship to their historical averages (Figure 1.5), the velocities of the kinematic units estimated by UAVSAR (Figure 1.13) reveal an overall slowing of the landslide consistent with previous observations reported by Coe (2012). These observations highlight the limitations of using GPS point measurements to infer the overall landslide behavior on timescales of days to weeks.

1.6.3 Kinematic Units and Geomorphic Domains

Figure 1.13 compares the week-long average horizontal velocity magnitude of each kinematic unit for each of the 2012 UAVSAR-derived velocity inversions with the 5-year (1985-1990) average horizontal velocity magnitude estimate for each kinematic unit derived from aerial photography (Smith, 1993; Schulz et al., 2012). Between the approximately 30 years separating these measurements, the landslide speed has reduced by approximately $0.25 cm/day$. Both the GPS point measurements shown in Figure 1.5, and the UAVSAR measurements shown in Figure 1.13 suggest that the largest reductions in velocity were found in the body of the landslide.

Along the slide boundaries, the UAVSAR image pixel coherence drops dramatically due to large surface-displacement gradients (Bürgmann et al., 2000), reminiscent of surface ruptures of strike-slip faults (Gomberg et al., 1995) (linear regions of dark black pixels bounding the landslide along domains 6-9, Figure 2.3 and Figure 1.8 bottom right inset). Domains 1-4, which form the landslide head, exhibit similar kinematics with horizontal velocity magnitudes of 0.26 ± 0.03 cm/day (Figure 1.8). While the velocity magnitude in this region is not distinct from the background magnitude due to the short one-week interferogram intervals, the direction of motion is consistent with the downslope direction in which the landslide is expected to move, and the magnitude of the velocity vectors increases from the upper boundary of the landslide towards the fast moving neck.

The "transition region" of the landslide between its head and main body shows a sharp jump in the velocity across the boundary between kinematic units 4 and 5, with a 170% velocity step increase from 0.31 cm/day in kinematic unit 4 to 0.64 ± 0.18 cm/day in kinematic unit 5. While the vertical deformation is expected to be small relative to the noise, the upper boundary of kinematic unit 5 contains thin linear regions of high negative vertical velocity gradients characteristic of vertical motion along the predominant normal faults mapped at this location (Fleming et al., 1999). While present in the vertical velocity images, these sharp transitions are only visibly identifiable in the the east and north velocity components of Figure 2.3. Both the head and transition regions exhibit broad bands of normal faults and tension cracks, characteristic of downslide extension.

Downslope from here, material slides into a geomorphic domain/kinematic unit 6 termed the hopper (Fleming et al., 1999), a 200 m long zone in which the landslide narrows from 230 m to 180 m. The name of this region arises out of the material being constrained and funneled inward by the lateral boundaries of the landslide. Across this region, there is a 40% reduction in the velocity vector direction variance in the downslope direction as the slide material moves increasingly downslope, parallel to the landslide's lateral boundaries. This region is also where the landslide experiences an abrupt increase in slope of $\sim 2\%$, which continues through the narrow neck of the landslide to the downslope extent of kinematic unit 7.

The boundary between the kinematic unit 5 and the hopper is defined geomorphologically by large downslope facing scarps (normal faults) and kinematically by a 0.39 ± 0.28 cm/day velocity jump across the boundary. This region can be seen in Figure 1.8, and is the green region upslope of the fast narrow neck, which roughly corresponds with kinematic unit 7. The downslope end of the hopper, located at the boundary between kinematic units 6 and 7, is marked by an abrupt band of normal faults and tension cracks and expresses itself kinematically as another discrete jump in velocity ($\sim 0.2 cm/day$). This sharp increase in velocity is clearly seen in the east and north components of the velocity shown in the lower and middle panels of Figure 2.3, respectively. Excluding kinematic unit 1, the vertical velocity estimate over the head region is -0.08 ± 0.37 cm/day, whereas the vertical velocity within the neck and hopper is -0.16 ± 0.15 cm/day.

The velocity progressively decreases in the downslope direction through kinematic units $8-11$. The only distinct kinematic boundary observable from our results within these domains is between kinematic units 10 and 11. This kinematic boundary coincides with a geomorphic boundary defined by a right-lateral strike-slip fault, with relative displacement rates across the fault of 0.28 ± 0.19 cm/day. This kinematic boundary arises due to the fact that unit 10 is not currently moving as rapidly as unit 11.

1.7 Discussion

The contribution of landsliding to long-term erosion rates is not well understood, in part due to the variety of timescales associated with the different physical mechanisms governing landslide motion. Landslides may occur as temporally discrete catastrophic failures, or as persistent and episodic failures with decadal, seasonal, and daily velocity variations. In this paper we explore the intermediate timescales of weeks to months. The variety of timescales operating most likely arises due to complex boundaries, distinct kinematic elements, multiple-slip planes, and non-homogeneous interiors of landslide bodies (Coe et al., 2009; Van Asch et al., 2009). In order to further constrain the operating landslide mechanics (e.g. dilation, interstitial pore-pressure, basal shear stress, shear banding) from surface velocity measurements, we need to know the volume and geometry of the deforming landslide material. Traditionally, measurements to define landslide geometry are expensive, labor intensive, and limited to point locations. Further, to understand the seasonal acceleration and deceleration, we need to characterize the visco-plastic behavior of the landslide material.

Currently, the initiation and cessation of sliding is not described by steady-state power-laws, which have been applied to geomorphic transport laws (Booth and Roering, 2011).

1.7.1 Comparison of Spring and Summer Kinematics

The Slumgullion Landslide moves by sliding along discrete bounding faults whose geometry results in segregation of the landslide into distinct kinematic domains. Coe et al. (2009) provide evidence for the persistence of these bounding faults by showing that the location of surface ponds remained spatially constant rather than moving with the landslide material. Schulz et al. (2012) provide evidence for the persistence of the kinematic domains between 1985-2010 using terrestrial InSAR measurements and results from previous studies. We find that the geomorphologically identified domain boundaries are also present within our velocity images and the boundaries coincide with sharp velocity gradients.

The top panel of figure 1.14 shows the velocity of the slide along a 1D profile running from the toe to the head. For reference, the average median horizontal velocities of each kinematic domain from 1985 to 1990 are shown by black crosses, as estimated from the results of a study of aerial photographs (Smith, 1993; Schulz et al., 2012). With the exception of the fast-moving neck of the landslide and domains located immediately downslope (kinematic units 7-9), we observe that the slide was moving approximately at the same average speed in this earlier period as in the spring of 2012.

The velocities in spring (April) and in summer (July) track each other well along the profile but the summer velocities are lower by ~ 0.1 cm/day with the exception of at the head of the slide, suggesting decay of excess pore pressures that resulted from snowmelt infiltration during March-May. The spring velocity decreases in the upslope direction from kinematic unit 7 through kinematic unit 4, beyond which (kinematic units $3-1$) velocities are consistent, while the summer velocities remain consistent through units 4-1. This change reflects the head being faster during the summer than during the spring by ~ 0.1 cm/day, most likely due to progressively later snowmelt at higher elevations.

1.7.2 Depth inversion

We present here a framework for the extraction of slide thickness and basal geometry from remote sensing alone; this is especially advantageous in mountainous regions, which are hard to access. The “landslide-wide” coverage of the UAVSAR-derived velocity field allows us to overcome the limitations of point measurements and estimate the thickness across the entire landslide. The 3D surface deformation enables inversion of the depth and orientation of the landslide basal plane using conservation of mass and a free-surface kinematic boundary condition. Inversions of this type have previously been used in glaciology (Rasmussen, 1988; Farinotti et al., 2009; Morlighem et al., 2011) and applied to the la Chapière landslide in France by Booth et al. (2013a). We follow a similar approach adapted for use with 3D surface velocity measurements. We also find that the inversion requires less tuning of unknown parameters when a visco-plastic rheology is considered.

Surface velocity and thickness evolution equations

For slow slender steady landslides, such as Slumgullion, the static component of stress is much larger than the dynamic component, and thus we expect the total pressure to be approximately hydrostatic such that

$$P = \rho g \cos\theta H, \tag{1.11}$$

where ρ is the density, P is the pressure, g is gravity, θ the angle of the incline from horizontal and H is the characteristic thickness of the landslide (Figure 1.15). We assume no external pressure is applied at the free surface. The force balance governing the dynamics of this gravity-driven creeping flow is between the viscous stresses and pressure gradients within the landslide. The magnitude the body force exerted by gravity on any given parcel of material is small compared to the integrated effect of the pressure generated by the material column above it. The force balance between viscous stresses and pressure gradients reveal that the characteristic surface velocity scales as:

$$U = \frac{\rho g \cos\theta H^3}{\mu L}, \tag{1.12}$$

where μ is the effective viscosity and L is the characteristic length in the direction of flow (x). In order to form an expression for the thickness of the landslide, we model the landslide as fluid flow down an inclined plane. Observations of landslide basal shear distributed through zones as much as several meters thick supports use of the zero slip assumption. The velocity field is defined as $\mathbf{u} \equiv \left\langle u, v, w \right\rangle$, the horizontal and vertical velocities at the ground surface are defined as $\mathbf{u}_{surf} \equiv \left\langle u(x, y, z = h_{surf}(x, y), t), v(x, y, z = h_{surf}(x, y), t) \right\rangle$ and $w_{surf} \equiv w(x, y, z = h_{surf}(x, y), t)$, respectively (Figure 1.15).

Examining the conservation of mass equation in order to determine the size of density perturbations

$$\nabla \cdot (\rho \mathbf{u}) = \rho \nabla \cdot \mathbf{u} + \mathbf{u} \cdot \nabla \rho = 0, \tag{1.13}$$

we find that the flow can be regarded as incompressible ($\nabla \cdot \mathbf{u} = 0$) if the normalized changes in density are small ($\frac{\Delta\rho}{\rho} \ll 1$). The size of these density perturbations are determined from the definition of the bulk modulus (κ):

$$\kappa \equiv \rho \frac{\partial P}{\partial \rho} \approx \rho \frac{\Delta P}{\Delta \rho} \tag{1.14}$$

$$\Rightarrow \frac{\Delta \rho}{\rho} = \frac{\rho g H}{\kappa}. \tag{1.15}$$

Using measured physical parameter values from Schulz et al. (2007, 2009b) and references contained within ($\rho \approx 2500\ kg/m^3$, $\kappa \approx 5-40\ GPa$, $H \approx 15\ m$), we find that the normalized density perturbations indeed are small ($\frac{\Delta\rho}{\rho} \sim \mathcal{O}(10^{-4})$).

The governing equations for incompressible flow are given by mass and momentum balance, respectively:

$$\nabla \cdot \mathbf{u} = 0, \quad \rho \frac{d\mathbf{u}}{dt} = \rho \mathbf{g} - \nabla P + \nabla \cdot \sigma \tag{1.16}$$

with the following kinematic boundary condition at the free surface (h_{surf}) and no-slip at the basal surface (h_{basal}):

$$w_{surf} = \frac{\partial h_{surf}}{\partial t} + \mathbf{u}_{surf} \cdot \nabla_H h_{surf}, \quad w_{basal} = \mathbf{u}_{basal} = 0 \tag{1.17}$$

where ∇ is gradient, $\nabla \cdot ()$ is the divergence, $\nabla_H \equiv \left(\frac{\partial}{\partial x}, \frac{\partial}{\partial y}\right)$ is the horizontal gradient, and σ is the stress tensor.

Integrating the mass balance equation (Equation 1.16) over the flow depth and utilizing the Leibniz Integration Rule we obtain:

$$\begin{aligned}\int_{h_{basal(x,y)}}^{h_{surf}(x,y)} \frac{\partial w}{\partial z} dz &= w_{surf} - w_{basal} \\ &= -\nabla_H \cdot (\mathbf{q}) + \mathbf{u}_{surf} \cdot \nabla_H h_{surf} - \mathbf{u}_{basal} \cdot \nabla_H h_{basal}\end{aligned} \tag{1.18}$$

where $\nabla_H \cdot ()$ is the horizontal divergence, and $\mathbf{q} = \int_{h_{basal}}^{h_{surf}} \mathbf{u} dz$ is the horizontal mass flow rate. Note that this is a very general expression independent of the boundary conditions and dimension of the problem, as well as of the rheology since we have not specified a constitutive relation for σ. The vertical velocity of the fluid at the surface is due to the advection of the basal and surface topography, and the flux of material into or out of the region.

If we write the mass flow rate ($\mathbf{q}$) in terms of the depth-averaged horizontal flow rate flow rate ($\bar{\mathbf{u}} \equiv \frac{1}{h} \int_{h_{basal}}^{h_{surf}} \mathbf{u} dz$) and apply the boundary conditions (Equation 1.17) we obtain the canonical thickness evolution equation (Liu and Mei, 1990; Balmforth and Craster, 1999; **?**):

$$\frac{\partial h_{surf}}{\partial t} = -\nabla_H \cdot (h\bar{\mathbf{u}}). \tag{1.19}$$

This is the form of the equation used by Booth et al. (2013a) to invert for the thickness of the la Chapière landslide in France. The change in elevation measurements $\left(\frac{\partial z}{\partial t}\right)$ obtained from differencing DEMs is equivalent to the left-hand side of Equation 1.19 $\left(\frac{\partial h_{surf}}{\partial t}\right)$. However, the vertical deformation derived from the UAVSAR data is the actual velocity of the surface material (w_{surf}), rather than the change in the height of the surface. This distinction between the equations and measurements is related to whether we approach the problem using a Eulerian or Lagrangian specification of the flow field.

The various modeled and measured quantities can be seen in Figure 1.15. Slow geophysical flows have often been modeled using a visco-plastic rheology and the assumption of incompressible flow (Liu and Mei, 1990; Coussot et al., 1996; Coussot and Proust, 1996;

Balmforth and Craster, 1999; Balmforth et al., 2002; Mei et al., 2001; Mei and Yuhi, 2001; Ancey, 2007; Matson and Hogg, 2007; Hogg and Matson, 2009).

Only applying the boundary conditions on Equation 8 at the basal surface, or rewriting the left-hand side of Equation 1.19 using the surface kinematic boundary condition, we obtain a similar expression written in terms of the surface velocity:

$$w_{surf} = -\nabla_H \cdot (h\bar{\mathbf{u}}) + \mathbf{u}_{surf} \cdot \nabla_H h_{surf}. \tag{1.20}$$

This is the form of the equation we will use, since we can project our data into the $(\hat{x}, \hat{z})$ coordinate system shown in Figure 1.15 and equate our measured slide-perpendicular motion with the left-hand side of Equation 1.20.

The "Rheological parameter" f

The horizontal flow rate $(\bar{\mathbf{u}})$ can be written such that it is proportional to the surface velocity, $\bar{\mathbf{u}} = f\mathbf{u}_{surf}$. The proportionality constant (f), which we will refer to as the "rheological parameter," is related to the assumed rheology and varies from 0 to 1.

In order to explore this further, we will consider a flow down a rigid impermeable plane inclined at an angle θ, with a visco-plastic rheology described by the Herschel-Bulkely model (Figure 1.15). The Herschel-Bulkely model captures the transition from flow to no-flow, as well as shear-thinning and -thickening behavior by combining the effects of Bingham and power-law flow. For shear stresses below the yield stress $(\tau < \tau_y)$, there is no flow $(\dot{\gamma} = 0)$, for stress exceeding the yield stress $(\tau > \tau_y)$ the relation between the shear-stress and strain-rate in the Herschel-Bulkely model is given as $\tau = \tau_y + \mu\dot{\gamma}^n$ where μ is the consistency index (viscosity), n is the flow index, τ is the shear stress, and γ is the shear strain. Newtonian fluids are a special case of the Herschel-Bulkely model where the flow index n is 1 and the yield stress τ_y is zero $(n \equiv 1, \tau_y \equiv 0)$. Power-law fluids also display a zero yield stress $(\tau_y \equiv 0)$ but are not restricted to a flow index of 1, while Bingham fluids have a flow index equal to 1 and a non-zero yield stress $(n \equiv 1, \tau_y \neq 0)$.

Booth et al. (2013a) assumed a power law rheology and wrote the flow rate as $q = fh\mathbf{u}_{surf}$ where $f = 2/3$ corresponds to Newtonian viscous flow, $2/3 < f < 1$ represents plug flow, and $f = 1$ represents a rigid sliding block (Booth et al., 2013b). We will derive similar expressions here for visco-plastic flow described by the Herschel-Bulkely model.

For simplicity, we will only discuss the resulting velocity profiles for two-dimensional Bingham flows following Liu and Mei (1990). Free surface visco-plastic flows result in two layers separated by a yield surface $Y(x,t)$; the upper region has a nearly zero shear rate since the stress is below the yield stress (τ_y) and will be called the plug-flow region, the layer below this yield surface is the viscously deforming region, which for Bingham materials yields a Newtonian-like parabolic flow profile (Ancey, 2007).

The velocity profile within the shear zone is parabolic and is given as:

$$u(x,z) = \frac{\rho g \cos\theta}{\mu}\left(\tan\theta - \frac{\partial h}{\partial x}\right)\left(Yz - \frac{z^2}{2}\right) \quad z < Y, \tag{1.21}$$

and the surface plug velocity is:

$$u(x,z) = \frac{\rho g Y^2 \cos\theta}{2\mu}\left(\tan\theta - \frac{\partial h}{\partial x}\right) \qquad z > Y. \tag{1.22}$$

Integrating these profiles:

$$\bar{u} = q/h = \frac{1}{h}\int_0^h u(x,z)dz = \frac{\rho g Y^2 \cos\theta}{6\mu}\left(\tan\theta - \frac{\partial h}{\partial x}\right)\left[3 - \frac{Y}{h}\right] \tag{1.23}$$

Thus we can relate the mean flow velocity to the surface velocity as:

$$f = \bar{u}/u_{surf} = \frac{3 - Y/h}{3} \tag{1.24}$$

Thus, when the entire depth has yielded and the plug region vanishes ($Y(x,t) \to h(x,t)$), we recover Newtonian flow and have $f = 2/3$. In the limit that the plug region dominates the depth profile ($Y(x,t) \to 0$), we have $f = 1$ as we'd expect with a rigid sliding block. A key difference between this model and a power-law model is that it has the ability to fully stop its motion, since there is no flow if the stress does not exceed the yield stress (τ_y); the power-law model only exhibits zero strain rate, and consequently zero surface velocity, for zero shear stress. For the more general Herschel-Bulkely model f is given as:

$$f_n = \frac{(2n+1) - nY/h}{2n+1} \tag{1.25}$$

In the case of a Bingham fluid assuming the viscosity is constant does not imply that f is constant throughout the slide. Rather, since f characterizes the thickness of the plug region in the flow, it implies that the plug region is a constant fraction of the total thickness. Table 1.5 shows the calculated values of f, from an expression we derive in the next section, estimated from a number of velocity-depth profile measurements of slow-moving, clay-rich landslides similar to Slumgullion and located across the globe, where U is the ground surface velocity, H is the total landslide thickness, Y is the height of the yield surface, and T is the thickness of the plug-flow region.

Viewing the landslide as a visco-plastic material has the advantage that we can bound the value of f to be between 2/3 and 1. Further, we see that $f_1 \approx 0.85 \pm 0.08$, and $f_3 \approx 0.80 \pm 0.09$ are estimated in this study from inclinometer data for clay-rich landslides globally (Gould, 1960; Ter-Stepanian, 1965; Chleborad, 1980; Iverson, 1985; Van Asch and Van Genuchten, 1990; Malet and Maquaire, 2003; Mainsant et al., 2012). While this is a small sample of landslides, it highlights that our choice of f is not dependent on the flow index n, but rather reflects a variation in the yields stress τ_y.

Imaging of shear zones typically shows alignment of elongated particles in the direction of shear, implying that distributed shear occurs even in shear zones just several millimeters thick (e.g. Lupini et al., 1981). True slip along a boundary might not occur in many situations, rather, distributed shear within very thin shear zones may give the appearance of discrete basal slip while discrete slip may really only occur between particles in the shear zone. The inclinometer data reported in Table 1.5 reveal subsurface deformation profiles similar to that in Figure 1.15, supporting our use of a visco-plastic rheology with a no-slip basal boundary condition.

Discretization and Inversion:

Using the rheological parameter f, we can rewrite the integrated mass balance equation (Equation 1.20) as:

$$w = \nabla_H \cdot (hf\mathbf{u}_{surf}) + \mathbf{u}_{surf} \cdot \nabla_H h_{surf} \tag{1.26}$$

where w and $\mathbf{u}_{surf}$ are the vertical and horizontal UAVSAR-measured velocities respectively. To invert for the depth of the landslide. this equation is discretized using an "unwinding scheme" appropriate for advection equations (LeVeque, 2007). But, this ill-posed inverse problem requires stabilization, thus we implement a Laplacian smoothing on the depth and solve the damped least squares form of the problem (**?**); this procedure is often generally referred to as Tikhonov regularization. This matrix equation is then solved using a scipy implementation of a non-negative least squares solver (Jones et al., 2001–). The level of smoothing was determined using the L-curve criterion by comparing the quality of fit with the size of the regularized solution. The L-curve is a graphical tool for displaying the trade off between the size of a regularized solution and the quality of its fit, as the regularization parameter varies, in our case the level of smoothing. In reality, this amounts to identifying the corner of the typical L-shape observed when making a log-log plot of the residual versus model size.

Assuming that the depth of the basal surface has not changed significantly from spring to summer, the depth profiles for several levels of smoothing using both the April and July one-week velocity measurements are shown in the lower panel of Figure 1.14. In this inversion, we have fixed the depths outside of the landslide footprint to be zero and assumed f is a constant equal to 0.8. We estimate that the depth of the landslide is 7.5 meters on average. If the rheological parameter is allowed to vary to its bounds of 2/3 and 1 as discussed previously, the average depth varies from 9.1 to 6.0 m. The average depth of the landslide is not sensitive to the smoothing parameter; however, there is a large variability of basal topography with less smoothing (Figure 1.14), which makes interpretations difficult. The optimal smoothing parameter of 0.33 shows that the slide deepens as the material decelerates towards the source and toe region. The most remarkable variation is observed entering the source region, and crossing the geomorphic domain boundary between zones 4 and 5. Interpretation of the deepening in the source and toe regions is especially difficult since these regions also contain the smallest signal-to-noise ratios, which is particularly evident in the vertical deformation (Figure 2.3). The inclusion of additional velocity measurements will lower the noise levels in these crucial regions and is required to have confidence in this anomalous deepening. Booth et al. (2013a) used deformation spanning 4 years, whereas we have used velocity measurements spanning $\sim$ 7 days. In order to utilize surface deformations spanning time periods of months to years for which traditional SAR images become de-correlated, we hope to apply the 3D vector inversion to UAVSAR pixel-tracking data in the same manner as we treated the UAVSAR in this study.

We note that the landslide thicknesses obtained from the inversion agree with previous observations and conclusions made regarding the landslide's toe evolution. Many (e.g. Parise and Guzzi, 1992; Varnes and Savage, 1996; Fleming et al., 1999) have observed that the toe overrides the present and former ground surface. The depth inversion (Fig. 1.14) at the landslide toe shows the landslide base as an upslope projection of the ground surface located immediately downslope from the slide, in agreement with observations. Further, Fleming et al. [1999] concluded that the toe of the landslide emerged from the subsurface and began sliding along the ground surface soon after the landslide initiated 300 yrs ago; their location of the emergent toe corresponds with 700 m along-profile distance (Fig. 11) and the basal geometry from the inversion suggests this emergence quite well. However, it is important to remember that in this inversion we did not allow for basal slip, or large variations in basal topography. This is an issue plaguing previously published methods for inferring landslide depth from surface measurements (Booth et al., 2013a; Aryal et al., 2015). Future work will focus on further usage of UAVSAR-derived InSAR interferograms and pixel-tracking velocity maps in conjunction with ground-based data, and more sophisticated modeling to allow for basal slip.

1.8 Conclusion

Mass wasting in mountainous regions, including clay-rich slow-moving landslides, can be the leading factor in controlling sediment production, long-term erosion rate, and topographic form (Kelsey, 1978; Korup et al., 2010; Booth and Roering, 2011; Mackey and Roering, 2011). Understanding how climatic forcing and a landslide's geometry interact to control landslide motion is necessary to quantify the contribution of landsliding to the long-term erosion rate and morphology of a landscape in past climatic and tectonic conditions (Roering et al., 2009) and to predict landslide behavior during changing climates in future decades (Coe, 2012). Increasing global temperatures will lead to more frequent and intense precipitation (Meehl et al., 2007) and consequently an increased risk of shallow landslide failure (Crozier, 1986). Understanding how landslides respond to these environmental changes is essential to hazard mitigation and has societal, environmental and financial impacts across the globe (Crozier, 2010; Winter et al., 2010) and will help identify the physical mechanisms controlling landslide acceleration and consequently allow for an improved understanding of how a landscapes's existing landslides and the spatial distribution of landslides within a landscape will respond to changing climatic conditions.

In order to understand how landslides respond to environmental forcing, we quantify how the hydro-mechanical forces controlling the Slumgullion Landslide express themselves kinematically in response to the infiltration of seasonal snowmelt. The well-studied Slumgullion Landslide, which is 3.9 km long and moves persistently at rates up to ∼2 cm/day is an ideal natural laboratory due to its large spatial extent and rapid deformation rates. In order to measure the response to perturbations of spatiotemporal fluid infiltration and the interaction of distinct kinematic units, we present a method for the characterization of 3D surface deformation with landslide-wide spatial coverage using the unique capabilities of the NASA/JPL UAVSAR airborne repeat-pass interferometry system. Deformation measurements provided by the UAVSAR system have advantages over space-based InSAR measurements in that the user can adapt acquisition plans to the desired target with optimal imaging geometries, and temporal sampling. Unlike space-borne InSAR, the UAVSAR system is not restricted to fixed viewing geometries and repeat times constrained by satellite orbit. By combining four LOS measurements along look directions chosen based on the landslide geometry, we invert for the full 3D landslide-wide surface deformation. The data acquisition and processing scheme presented here can be used to measure 3D surface deformation of any kind with applications to glaciology, hydrology, seismology, and volcanology (e.g. Minchew et al., 2015).

A comparison with survey-mode measurements of 17 GPS sites by the USGS validate this method and show that it provides reliable and accurate 3D surface deformation measurements. The UAVSAR-derived spatially dense velocity field reveals the persistence and stability of previously mapped basal, lateral and internal boundaries, and their characteristic sharp boundaries. Comparisons with previous GPS campaigns and deformation estimated from aerial photography indicates that the landslide has slowed since 1985. We acquired data during the spring and summer and identified that the landslide moves slower during the summer everywhere except at its head, presumably in response to spatiotemporal variations in snowmelt infiltration.

Displacement results for Slumgullion display clearly defined kinematic units comprising the landslide in agreement with earlier studies (Smith, 1993; Fleming et al., 1999; Schulz et al., 2012). However, we find that the landslide has slowed compared to speeds during 1985-1990 (Smith, 1993) and 1998-2002 (Coe et al., 2003). Slowing was not consistent across the landslide but was greatest within the landslide body. Our results also revealed that the landslide accelerated progressively later with increasing elevation, most likely due to progressively later snowmelt infiltration and consequent pore-pressure increases.

In order to interrogate the mechanics controlling landslide motion from surface velocity measurements, we need to know the volume and geometry of the deforming landslide material. Traditionally, these measurements are expensive and labor intensive, and are usually limited to point measurements. We present an inversion framework for the extraction of slide thickness and basal geometry from spatially dense vector velocity fields; this is especially advantageous in mountainous regions which are hard to access. Using the UAVSAR-derived 3D velocity measurements, we find that the average depth of the Slumgullion Landslide is 7.5 meters, several meters less than previous depth estimates. We propose that the UAVSAR system and imaging methodology can provide a valuable response tool for rapid characterization of landslide hazards following shaking from large-magnitude earthquakes for which the risk of landslides may increase for several years following the rupture (e.g. 1999 Mw-7.6 Chi-chi, 2008 Mw-7.9, 2015 Mw-7.8 Gorkha) (Yu et al., 2014; Witze, 2015).

We show that by considering a visco-plastic rheology, we can derive tighter theoretical bounds on the rheological parameter f relating mean horizontal flow rate to surface velocity by excluding non-physical regions of parameter space included in power-law models. We bound the rheological parameter to be between 2/3 and 1, rather than the 0 to 1 bound obtained when considering a power-law rheology. Using inclinometer data for slow-moving, clay-rich landslides similar to Slumgullion and located across the globe, we find a consistent value of the rheological parameter of 0.85 ± 0.08. Similar to previously published landslide depth inversion procedures, neither basal slip nor sharp variations in the basal topography are considered; however, we argue here that measurements of distributed slip occurring over centimeters to meters above the discrete basal surfaces and observations of aligned elongated particles in these shear zones (Lupini et al., 1981) support the use of the visco-plastic model and zero-slip boundary condition.

1.9 Acknowledgments

Part of this research was sponsored by the NASA Earth Surface and Interior Geodetic Imaging program and performed at the Jet Propulsion Laboratory, California Institute of Technology. We thank Jeff Coe (USGS) for performing GPS surveys at the landslide and for helpful discussions. We also thank the UAVSAR flight and data processing teams for their help with acquiring and processing the data. All UAVSAR interferograms and metadata used in this study can be downloaded from the Alaska Satellite Facility (ASF, https://www.asf.alaska.edu). This work was generously supported by NASA/JPL subward 1492856, and NSF GRFP Fellowship 923843294. The use of trade, product, industry, or firm names is for descriptive purposes only and does not imply endorsement by the US Government.

1.10 Figures

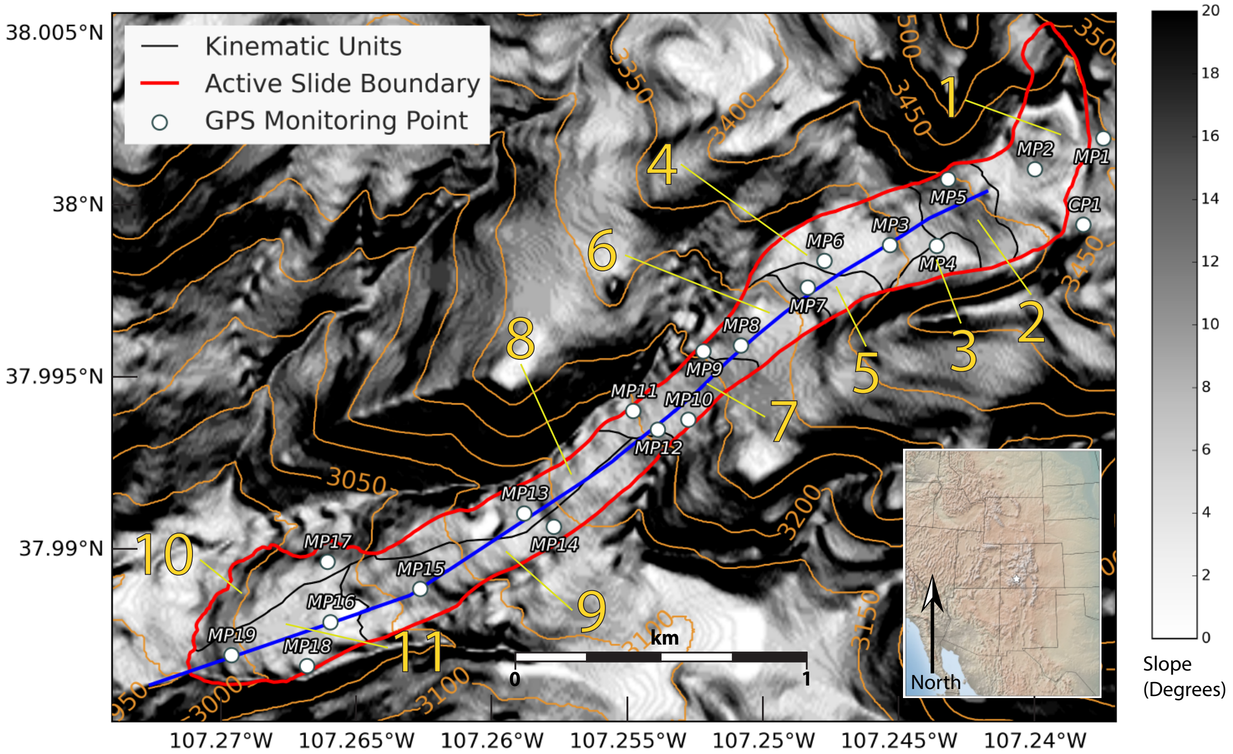

Figure 1.1: Slope and elevation of the Slumgullion Landslide and surrounding terrain. The *1/3* arcsecond DEM is from the USGS National Elevation Dataset (NED) and was formed in October 2010. The color scale varies from white to black as the slope varies from 0 to 20 degrees. The red line shows the boundary of the active portion of the landslide. The black lines show the distinct geomorphic domains within the slide as identified by Schulz et al. (2012). The white circles represent USGS GPS monitoring sites. The blue line represent the 1D transect shown in Figure 1.14.

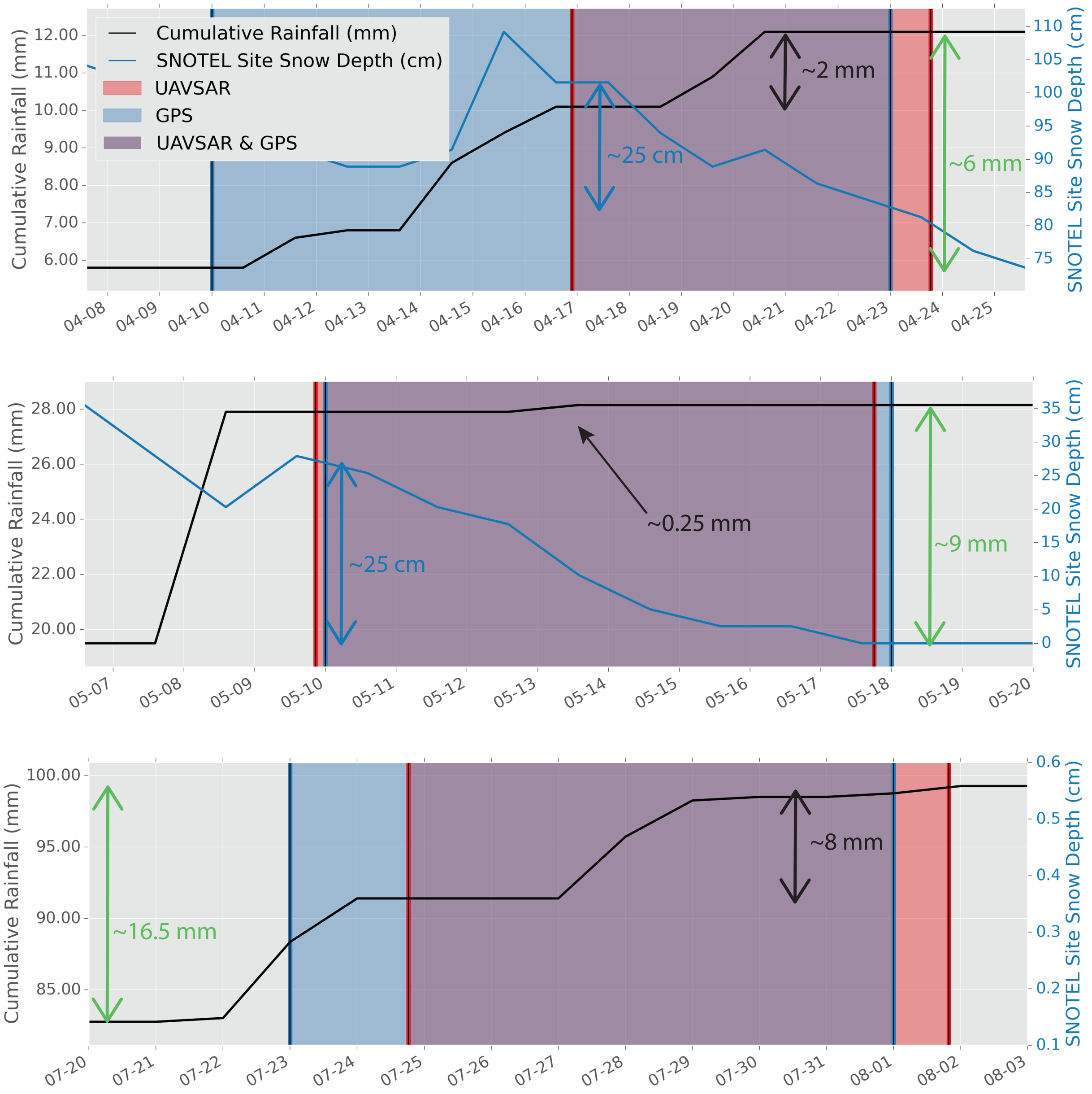

Figure 1.2: Time periods spanned by each GPS and UAVSAR velocity measurement, cumulative rainfall, and snow depth during April, May, and July 2012. The vertical red and blue bars represent the times of GPS and UAVSAR data acquisitions, respectively. The background colors represent the observation periods spanned by the GPS and UAVSAR velocity estimates; the blue regions represent times included in the GPS velocity measurements only, the red regions denote times included in the UAVSAR velocity measurements only, and the purple regions denote times spanned by both the GPS and UAVSAR velocity measurements. The rainfall precipitation is measured near the longitudinal center of the landslide (near MP10, Figure 1.1), and the snow depth is acquired from the U.S. Department of Agriculture Natural Resources Conservation Service at SNOTEL site 762 and is located 3.2 km to the southeast at the elevation of the uppermost part of the landslide ($\sim 3500 meters$, Figures 1.1 and 1.3). Blue and black annotations report the total change in cumulative rainfall and snow depth between the UAVSAR acquisitions. Green annotations denote the change in cumulative rainfall over the full time period shown in each panel.

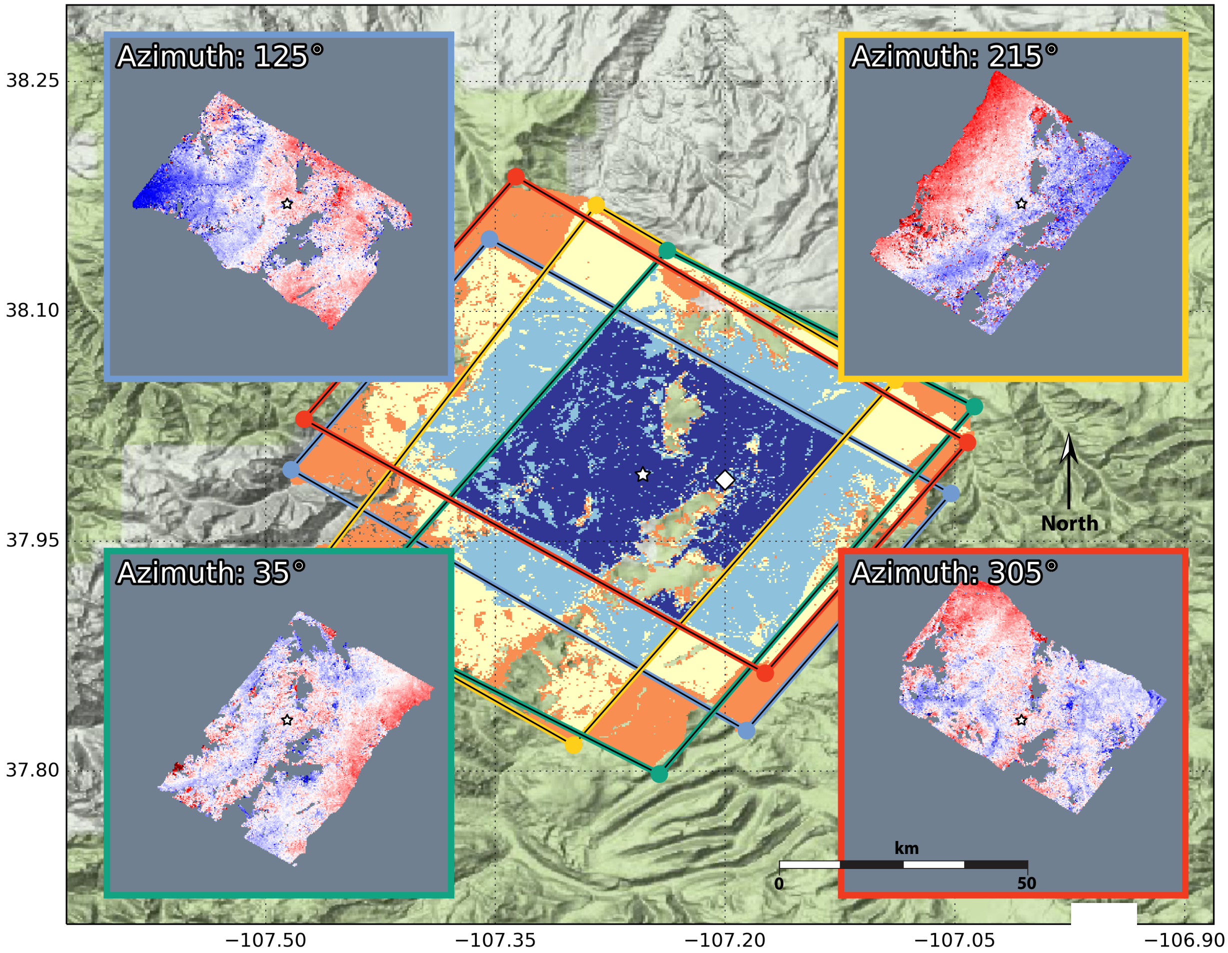

Figure 1.3: Slumgullion Landslide UAVSAR imaging geometry, and corresponding unprocessed LOS interferograms on top of a topographic basemap, modified from Delbridge et al. (2015). The white star and diamond show the location of the Slumgullion Landslide and snow telemetry (SNOTEL) site 762, respectively. The colored rectangles show the approximate non-zero footprint of each interferogram corresponding to Slumgullion lines 12502, 21501, 30502, and 03501 (first 3 digits indicate flight azimuth). The inset maps show uncorrected (e.g. prior to removal of phase ramps) and unwrapped LOS interferograms formed from UAVSAR acquisitions on April 16th and April 23 2012. All of the interferograms plotted show the unwrapped phase in radians with the color scale varying from blue to red as the phase varies from -2pi to 2pi where we have converted the phase to LOS velocity in units of centimeters per day. For reference, the count of the actual number of LOS observations for each pixel provided by the four April 2012 interferograms is shown beneath the rectangles, where orange, yellow, light blue and dark blue denote 1 ,2, 3 and 4 LOS observations per pixel. Pixels with coherence less than 0.3 are transparent.

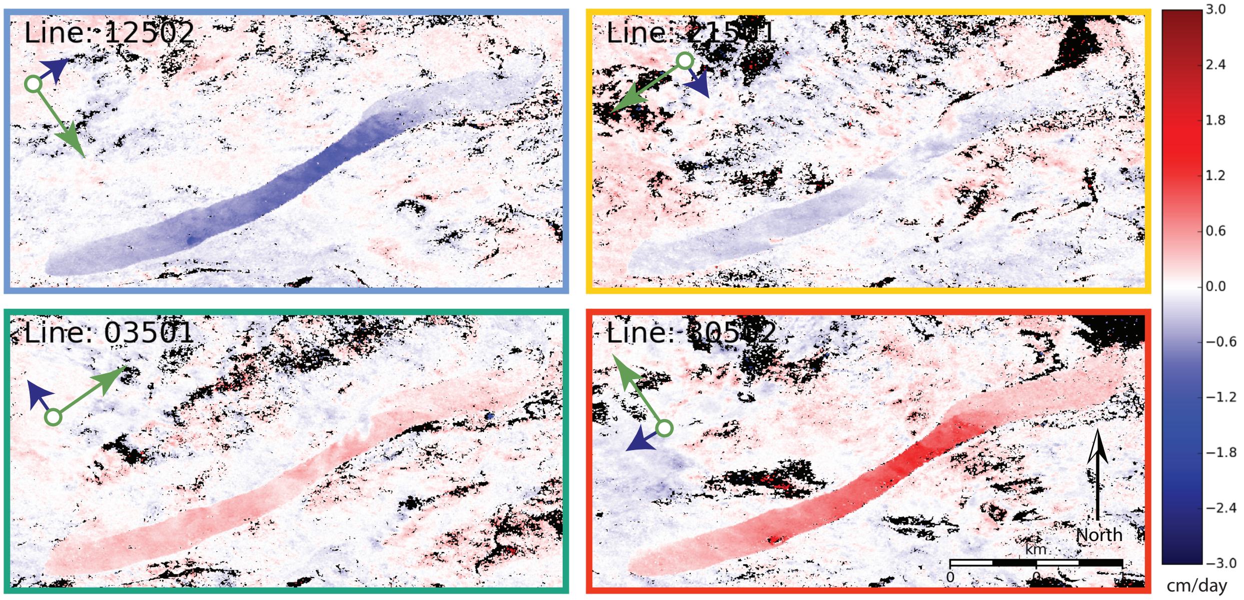

Figure 1.4: Unwrapped interferograms for each of the four Slumgullion fight lines formed from two sets of UAVSAR image acquisitions on April 16th and 23, 2012, respectively. The green arrow show the fight heading, and the blue arrow shows the radar look direction. The unwrapped phase change has been converted to velocity in units of centimeters per day which is indicated by the scale bar. Blue pixels indicate a decrease in distance in the LOS direction. The landslide deformation within its boundaries is clearly identifiable even in lines 03501 and 21501 in which the LOS vectors are least sensitive to the landslide deformation. Black pixels represent masked pixels with a coherence of less than 0.3.

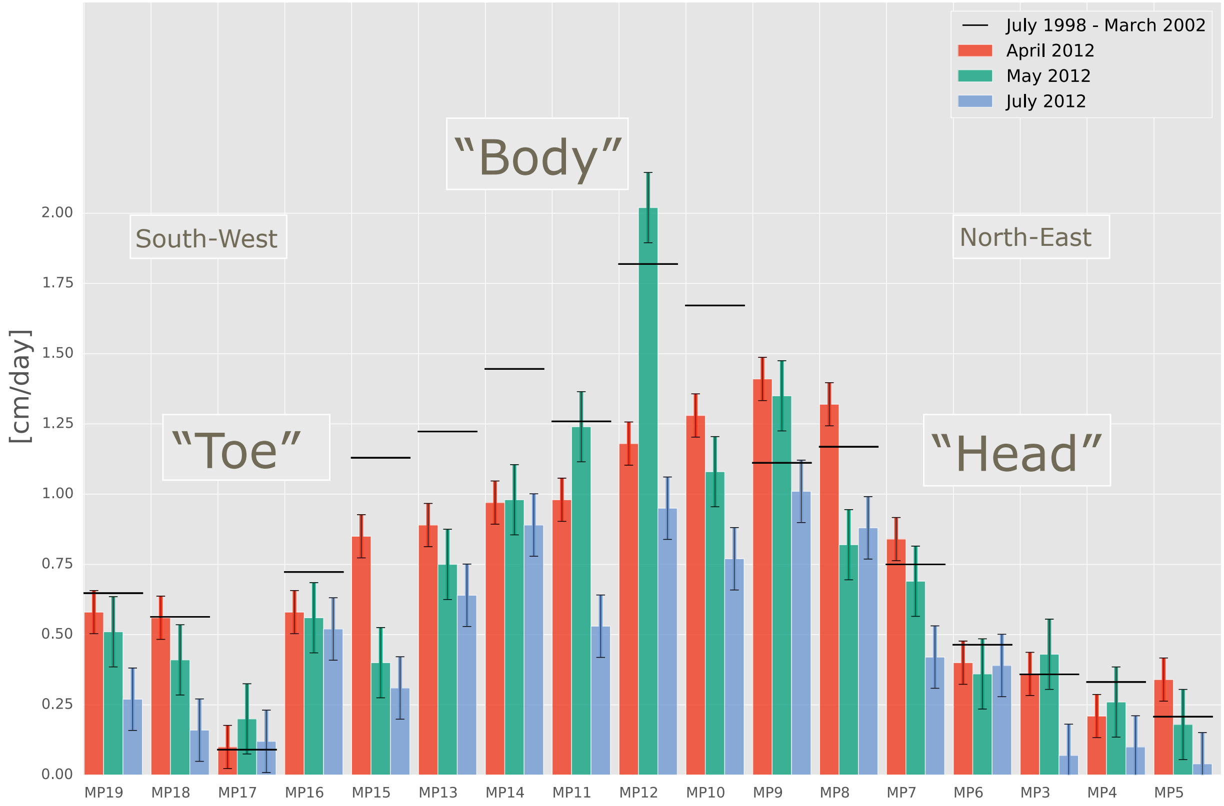

Figure 1.5: GPS-derived average horizontal velocity magnitude (scalar magnitude of the east and north vector components) estimates for three time periods in 2012 in which each measurement spans approximately 10 days; April 10-23 is shown in orange, May 10-18 is shown in green, and July 23-August 2 is shown in blue. The largest velocities are observed in the landslide body where the slide is the steepest and narrowest. The black bars represent the average horizontal velocity for each station from July 1998 to March 2002 as measured by Coe et al. (2003).

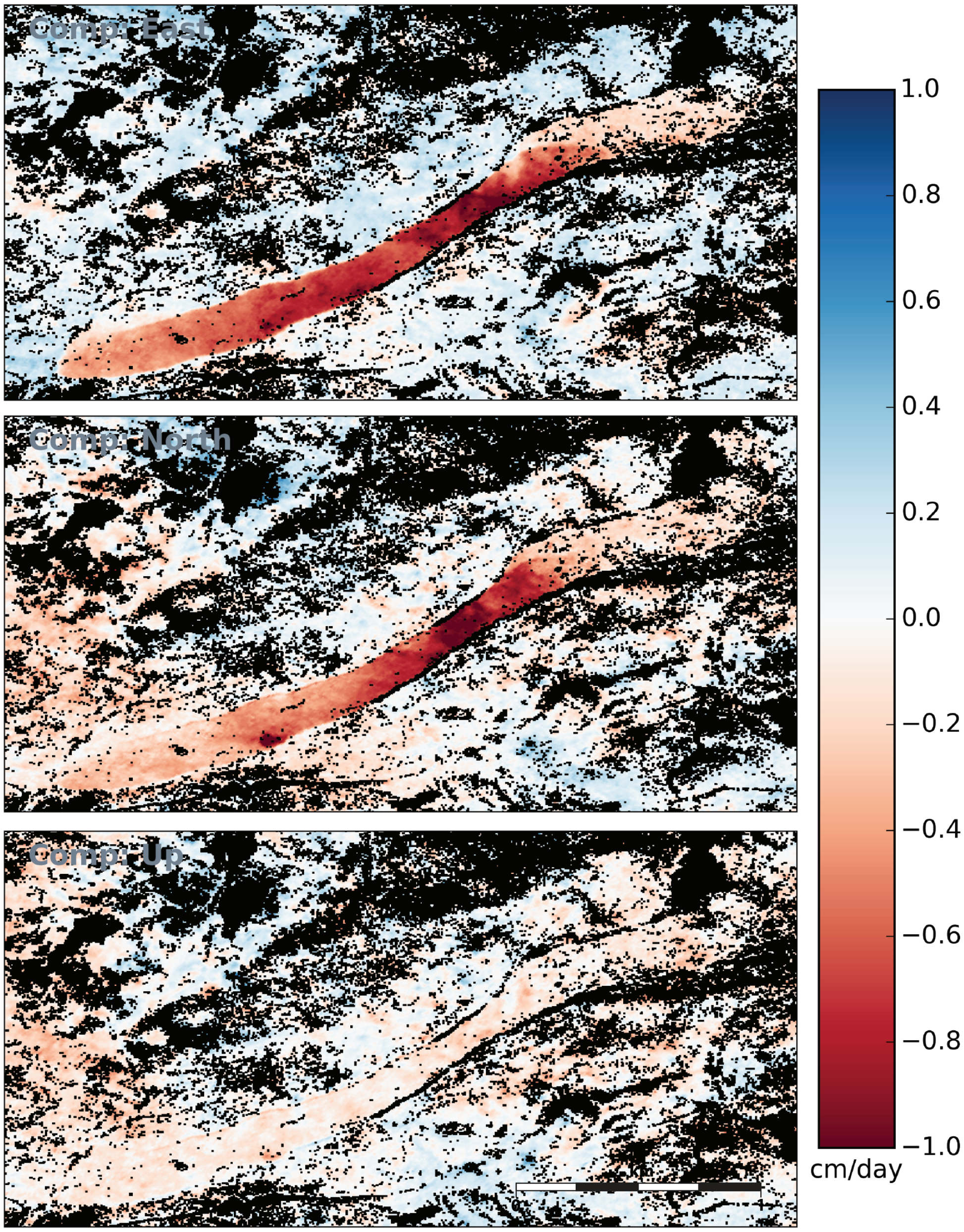

Figure 1.6: Results of the 3D vector inversions of the four April 2012 LOS images shown in Figure 1.4 in units of *cm/day*. The color ranges from red to blue corresponding to velocities ranging from −1 to 1 *cm/day*. The black pixels represent regions of large covariance in the inversion, and have estimated horizontal errors greater than 1 millimeter per day. The three panels show the magnitude and sign of the individual velocity components, East, North, and Up, respectively.

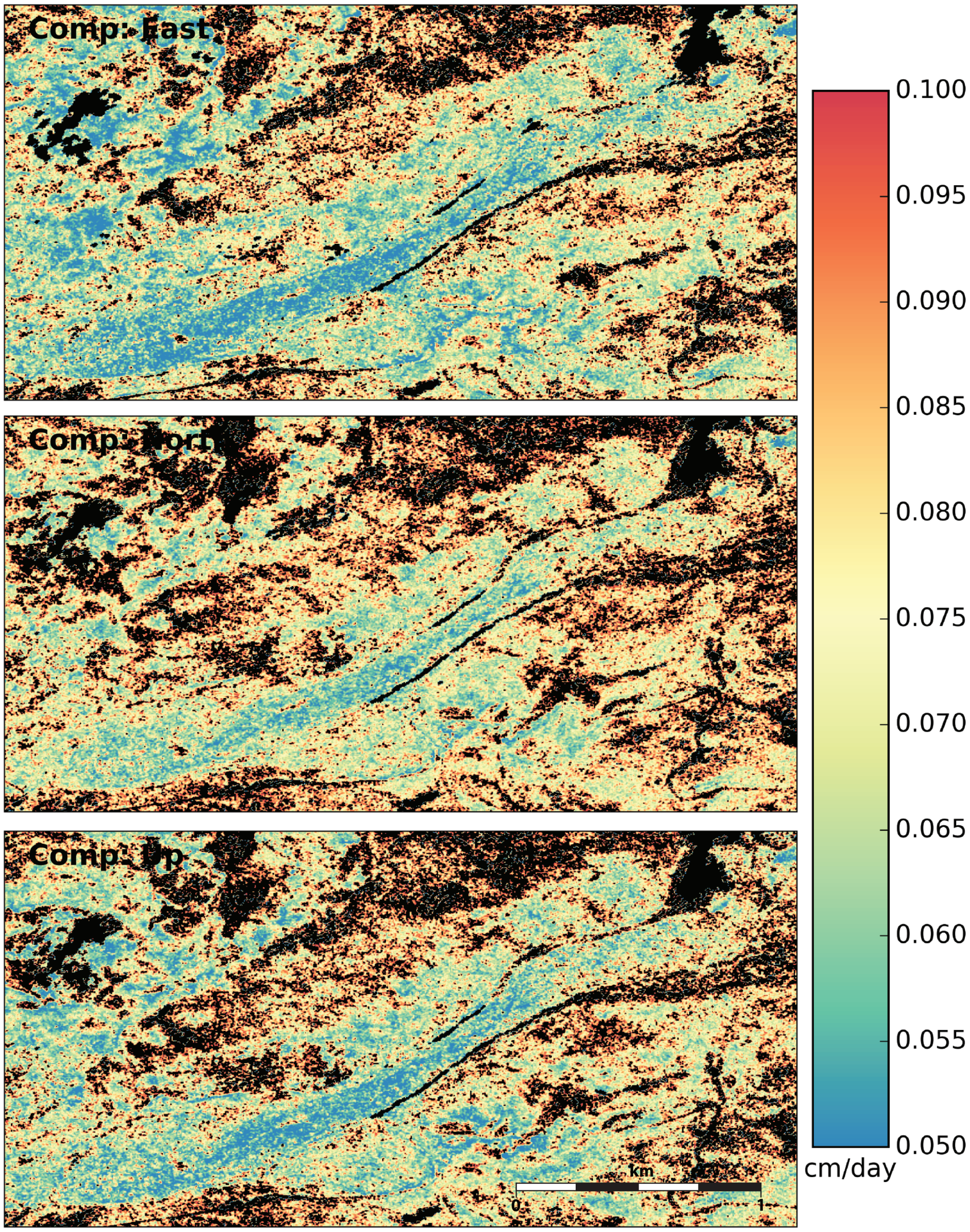

Figure 1.7: Velocity error estimates associated with the April 2012 3D vector inversions results shown in Figure 2.3. The color ranges from red to blue corresponding to errors ranging from 0 to 0.1 *cm/day*. The black regions in each panel denote masked out regions in which the error estimated for that component exceeds 1 millimeter per day. The three panels show the components, East, North, and Up, respectively.

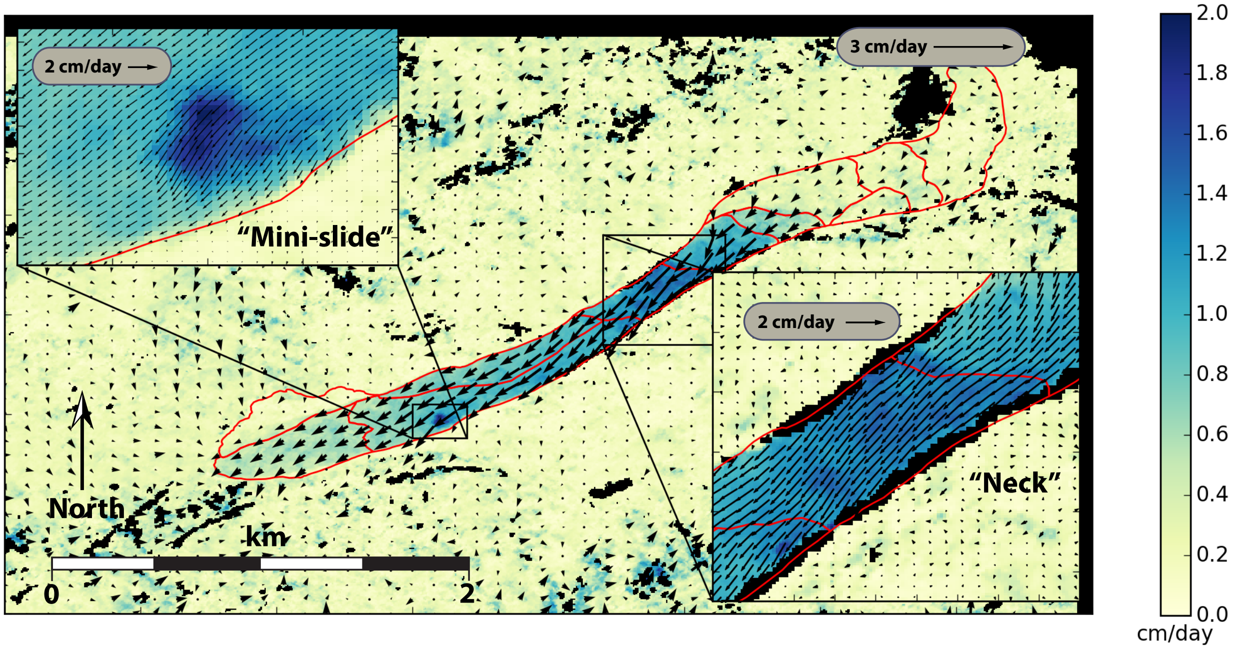

Figure 1.8: Horizontal and total velocities corresponding to the results of the April 3D vector inversions shown in Figure 2.3. The black arrows represent a downsampled representation of the same inverted horizontal velocity field. The magnitude of the total velocities are shown with color ranges from yellow to blue corresponding to velocities ranging from 0 to 2 *cm/day*. The black pixels represent regions of large covariance in the inversion, and have estimated errors greater than 5 *mm/day*. The inset in the top left corner shows a 7 times zoomed detail of a local failure we denote as the "mini-slide". The inset in the bottom right corner shows a 3 times zoomed detail of the steep and narrow landslide neck.

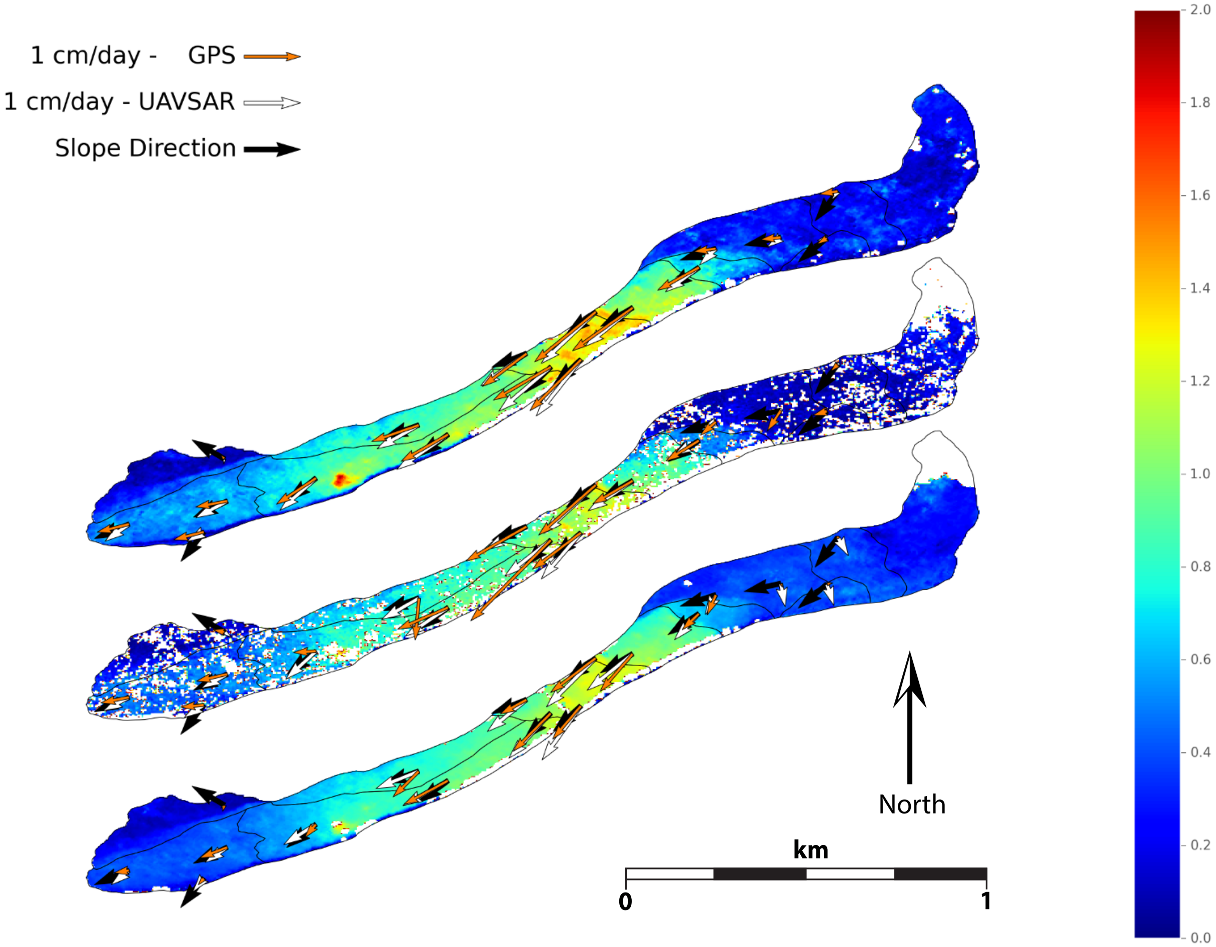

Figure 1.9: Comparison of GPS- and UAVSAR-derived horizontal velocity vectors. At the location of each of the GPS monitoring points, each component of the UAVSAR-derived horizontal velocity is extracted from the inversion images shown in in Figure 2.3 and represented by the white arrows. The collocated GPS-derived velocities for that time period are shown by the orange arrows. For reference, black vectors show the downslope direction (the negative normalized gradient at each GPS site). The three color panels show the magnitude of the horizontal velocity for the UAVSAR observations in April, May, and July, 2012, from top to bottom. Pixels with estimated errors greater than 5 *mm/day* are masked and not shown.

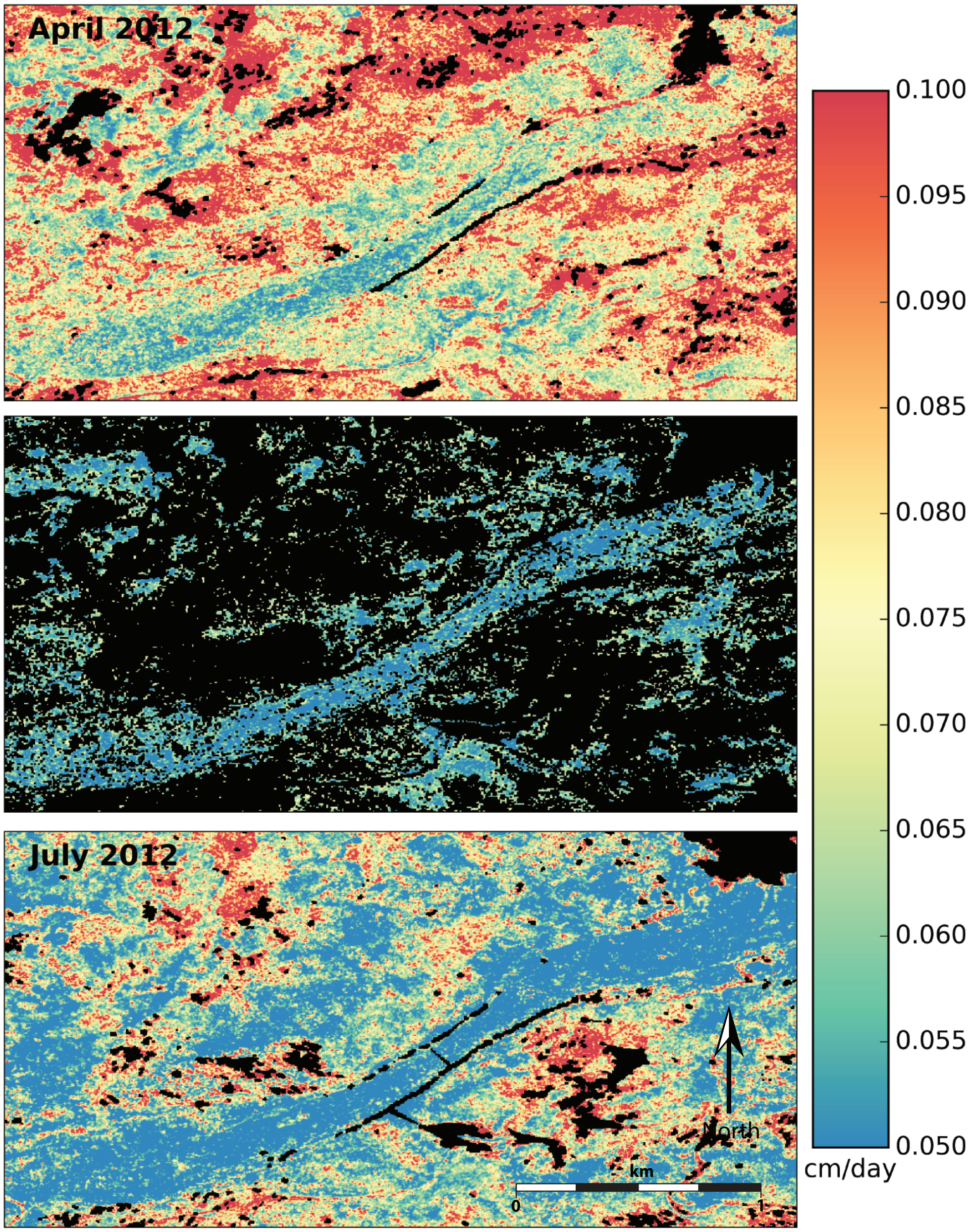

Figure 1.10: The magnitude of the estimated horizontal error for the April, May and July 3D deformation fields. The color ranges from blue to red corresponding to errors ranging from 0.05 to 0.1 *cm/day*. The black regions denote pixels in which the error exceeds 5 *mm/day*.

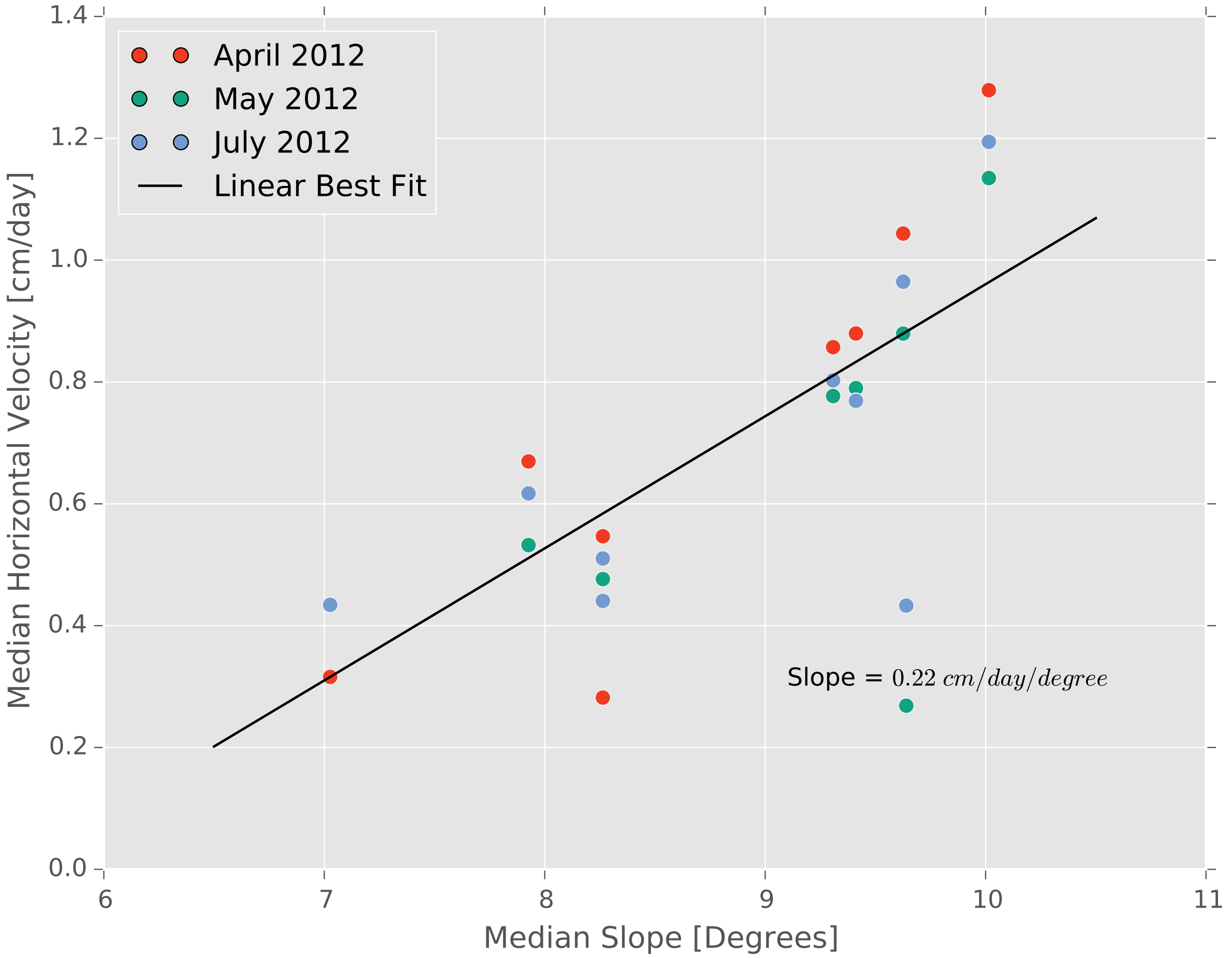

Figure 1.11: Relation between median slope and median UAVSAR-derived horizontal velocity for each kinematic unit. The median slope for each domain is calculated from the DEM in Figure 1.1. The blue, green, and red circles correspond to the median kinematic domain velocities from the April, May, and July 2012 UAVSAR measurements respectively. The best fit least squares regression is shown in black. We only consider here domains with median velocities exceeding 2 mm/day.

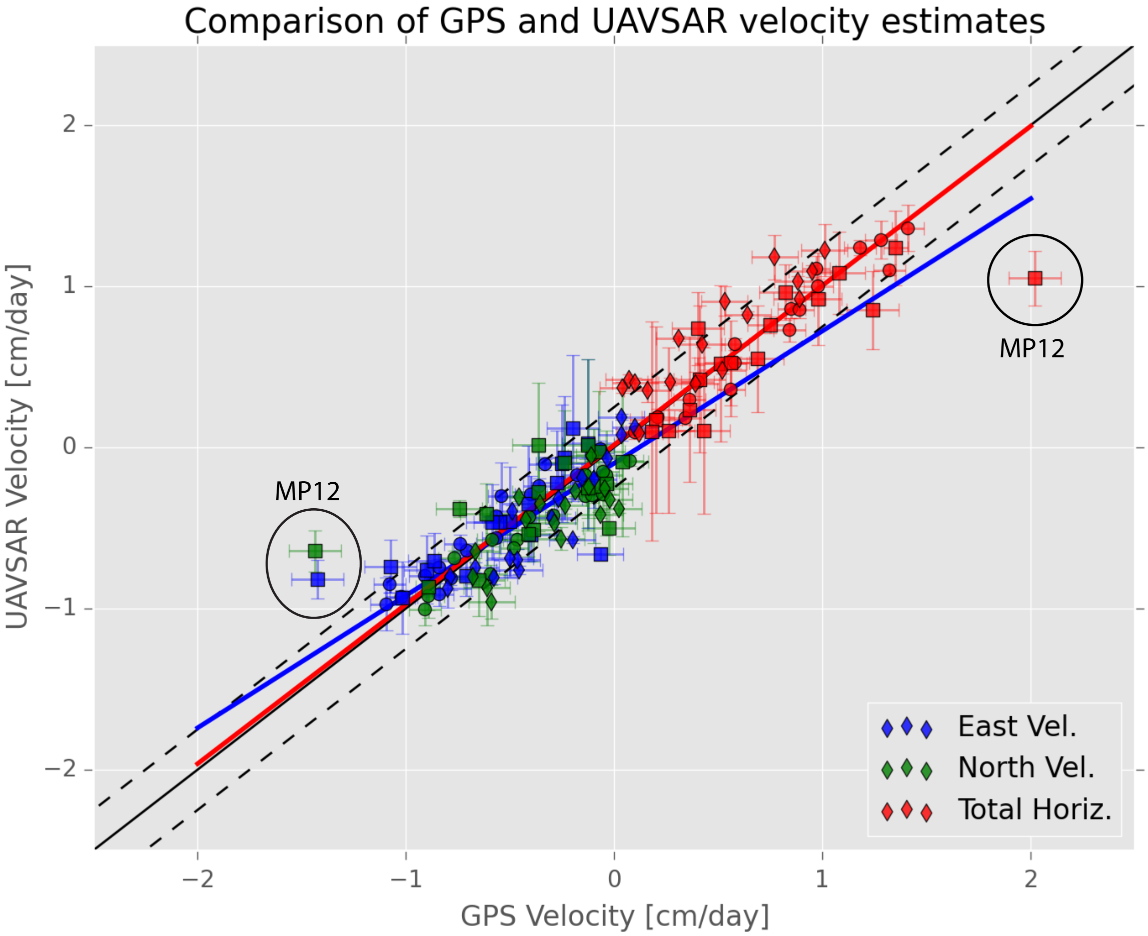

Figure 1.12: Comparison of the magnitude of each component of the velocities derived from GPS point measurements versus the UAVSAR-extracted velocities at the same locations and similar time periods. The east components are shown in blue, the north components in green, and the total horizontal velocities are shown in red. The circles, squares, and diamonds represent the values for the April, May, and July 2012 measurements, respectively. The solid black line represents a perfect agreement between the two measurements, the dashed black lines represents ± *2.5 mm/day*. The solid blue line shows the regression for the east and north components together, and the solid red line shows the regression for the horizontal velocity magnitudes. The error estimates for the UAVSAR-derived velocities shown in this figure represent the standard deviation of pixels within 30 meters of the GPS site.

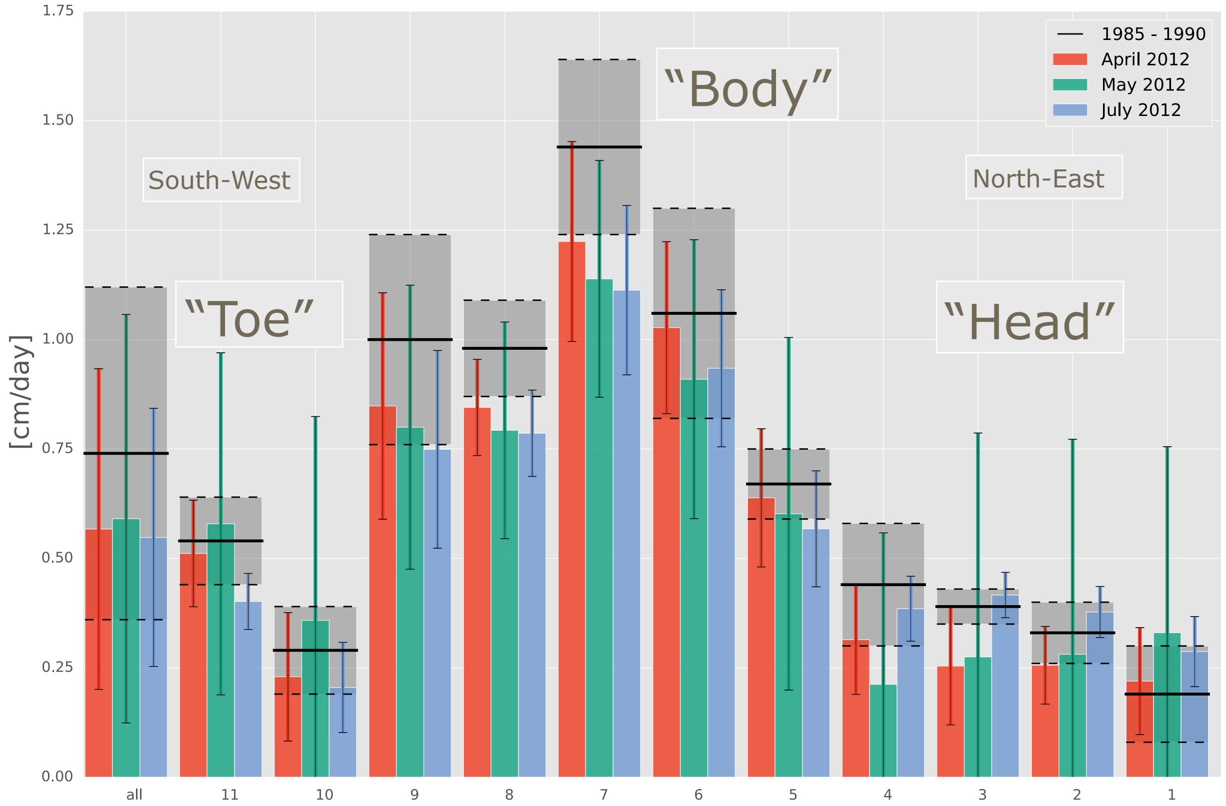

Figure 1.13: UAVSAR derived average horizontal velocity magnitude and standard deviation estimates for three time periods in 2012 for each kinematic domain defined in Figure 1.1; April 10-23 is shown in red, May 10-18 is shown in green, and July 23-August 2 is shown in blue. The solid and dashed black lines represent the average horizontal velocity and standard deviation of each domain during the time period of 1985 to 1990 as estimated by Schulz et al. (2012).

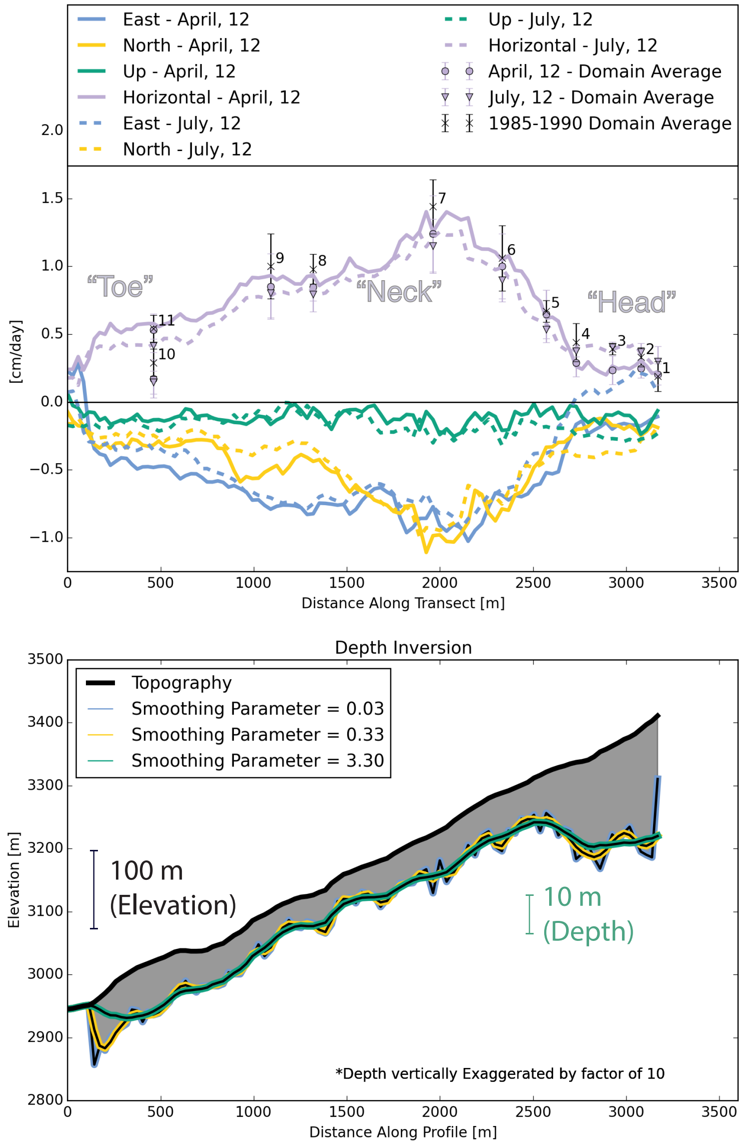

Figure 1.14: Along-slide velocity profiles showing each component of the variation from the toe to the head of the landslide. The solid and dashed lines represent the April and July 2012 measurements, respectively. The East, North, Up and Horizontal components are shown in blue, yellow, green and purple respectively. The mean and standard deviation of the total horizontal velocities of the geomorphological domains are shown by the circle and triangle markers. The black crosses represent the average horizontal velocity of each domain during the time period of 1985 to 1990 as estimated by Smith (1993); Schulz et al. (2012). The numbers correspond to the numbering of the geomorphic domains in Figure 1. BOTTOM: The predicted landslide thickness for a range of smoothing parameters is shown by the grey filled curves and colored lines, the thick black line represents the along-track topography. The results of depth inversion are vertically exaggeration by a factor of five relative to the elevation profile, black 100 meter and green 10 meter scale bars are shown for the profile elevation and inverted basal depth, respectively.

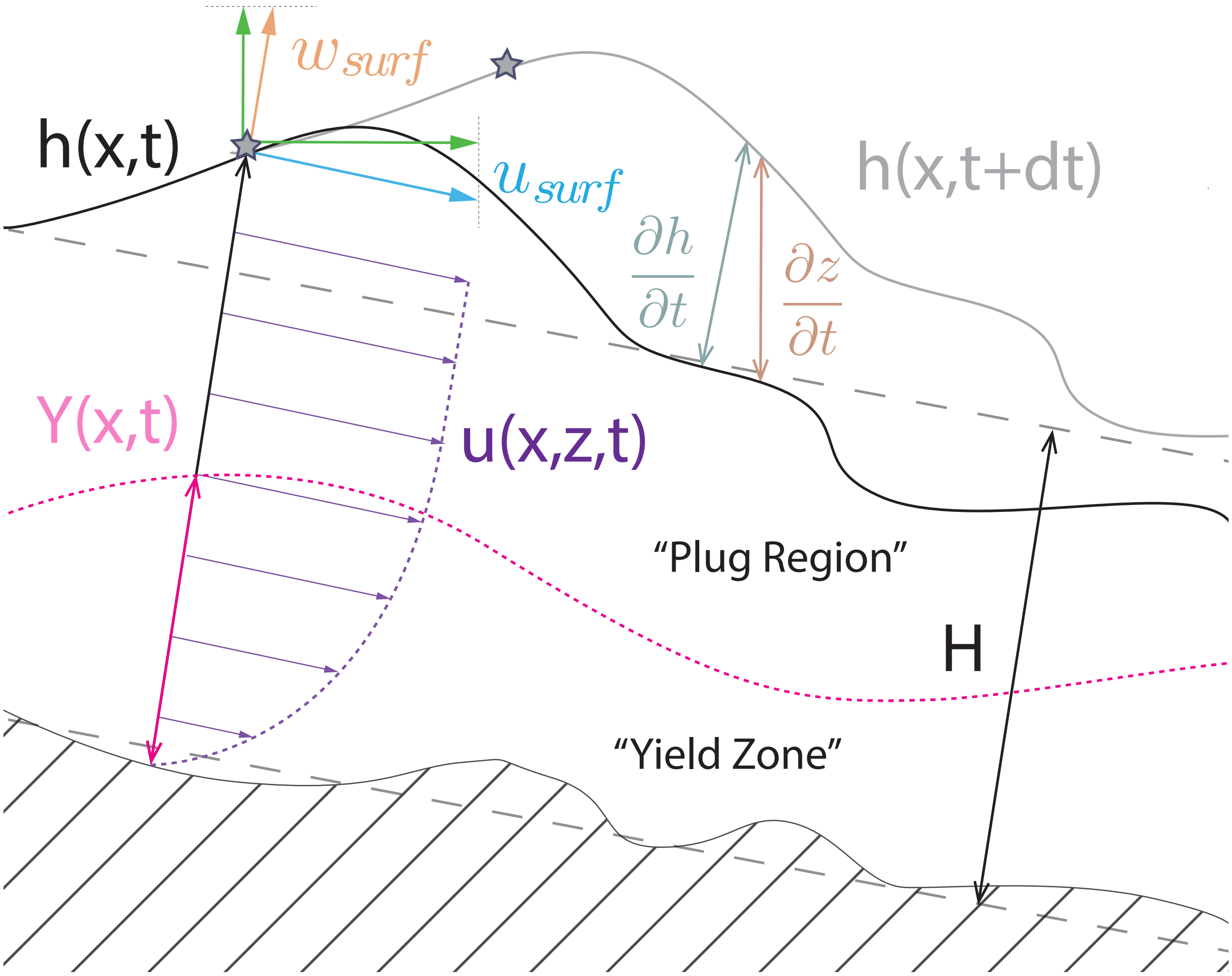

Figure 1.15: An idealized landslide of a visco-plastic material flowing down an incline with topography. The surface of the slide at the time of the UAVSAR measurement is shown by the black line. The surface at some later time is shown by the grey line. The two stars represents a specific InSAR scatter on the slide at the time of the measurement and some later time where the calculated velocities are shown by the green arrows. The grey arrow shows the apparent thickness change ($\frac{\partial h}{\partial t}$). The brown arrow shows the measured elevation change from differential DEMs. The dashed grey lines show the idealized planar surface geometries, where H is the characteristic thickness. The black arrow extending from the basal topography shown by the hashed region to the free surface shows the total slide thickness at the measurement point (the bottom extent and arrowhead are coincident and hidden by the pink). The purple arrows and dotted curve show an idealized depth velocity profile. The yield surface ($Y(x,t)$) is shown by the dashed pink line and is the depth where the stress equals the yield stress. Above the yield surface, the strain rate approaches zero and the flow moves as a uniform plug; below this region the material is viscously deforming and the velocity drops to zero at the basal surface.

1.11 Tables

Table 1.1: Temporal dataset parameters using the acquisition times of line 03501. The fourth column denotes the number of interferograms used in the inversion to obtain the 3D deformation field (Note that there was an error with the acquisition of line 21501 in July 2012; however, since this flight line is sensitive to the slope perpendicular deformation we still were able to obtain a robust inversion result using only the minimum of 3 look directions.).

Name:	**Pass 1:**	**Pass 2:**	**Temporal Baseline:**	**# Used:**
April, 2012	Apr 16, 2012	Apr 23, 2012	6.9	4
May, 2012	May 9, 2012	May 17, 2012	7.9	4
July, 2012	Jul 24, 2012	Aug 1, 2012	8.1	3

Table 1.2: Slumgullion flightline parameters and description of LOS deformation sensitivity. The first column gives the flight line ID number, and the second column gives the corresponding azimuth flown by the plane during acquisition. Columns three and four give the look directions and the corresponding motion to which each LOS measurement is sensitive. We also report the look angle range across the full UAVSAR images(Figure 1.3).

ID:	**Azimuth:**	**Look Direction:**	**Sensitivity:**	**Look Angle:**
03501	35	NW Across Landslide	Slope Perp.	52° – 55°
12502	125	From Toe Upslope	Slope Parallel	50° – 56°
21501	215	SE Across Landslide	Slope Perpend.	53° – 55°
30502	305	From Head Downslope	Slope Parallel	50° – 57°
	Near Range:		**Far Range:**	
Full Image:	$\sim 30°$		$\sim 70°$	

Table 1.3: UAVSAR- and GPS-derived velocity measurements (cm/day) at each of the Slumgullion GPS monitoring points shown in Figure 1.1.

	GPS				UAVSAR			
	April	May	July	Average	April	May	July	Average
MP19	0.58	0.51	0.27	0.45	0.53	0.51	0.41	0.48
MP18	0.56	0.41	0.16	0.38	0.31	0.43	0.35	0.36
MP17	0.10	0.20	0.12	0.14	0.10	0.17	0.09	0.12
MP16	0.58	0.56	0.52	0.55	0.65	0.53	0.48	0.55
MP15	0.85	0.40	0.31	0.52	0.86	0.73	0.68	0.76
MP13	0.89	0.75	0.64	0.76	0.86	0.77	0.82	0.81
MP14	0.97	0.98	0.89	0.95	1.11	0.93	0.92	0.99
MP11	0.98	1.24	0.53	0.92	0.98	0.86	0.91	0.92
MP12	1.18	2.02	0.95	1.38	1.24	1.06	1.09	1.13
MP10	1.28	1.08	0.77	1.04	1.28	1.07	1.18	1.18
MP9	1.41	1.35	1.01	1.26	1.36	1.26	1.23	1.28
MP8	1.32	0.82	0.88	1.01	1.10	0.97	1.03	1.03
MP7	0.84	0.69	0.42	0.65	0.73	0.58	0.64	0.65
MP6	0.40	0.36	0.39	0.38	0.40	0.30	0.39	0.36
MP3	0.36	0.43	0.07	0.29	0.29	0.13	0.42	0.28
MP4	0.21	0.26	0.10	0.19	0.19	0.10	0.40	0.23
MP5	0.34	0.18	0.04	0.19	0.18	0.09	0.37	0.21
MP2	0.14	0.66	0.08	0.29	0.16	0.19	0.27	0.21

Table 1.4: UAVSAR-derived velocity measurements (cm/day) for each kinematic unit shown in Figure 1.1.

	April	May	July	Average
all	0.57	0.59	0.55	0.57
11	0.51	0.58	0.40	0.50
10	0.23	0.36	0.21	0.26
9	0.85	0.80	0.75	0.80
8	0.84	0.79	0.79	0.81
7	1.22	1.14	1.11	1.16
6	1.03	0.91	0.93	0.96
5	0.64	0.60	0.57	0.60
4	0.31	0.21	0.39	0.30
3	0.25	0.28	0.42	0.32
2	0.26	0.28	0.38	0.30
1	0.22	0.33	0.29	0.28

Table 1.5: The first column gives the name of the region for which the depth-velocity profile of a slow-moving, clay-rich landslide was measured. The second column (U) is the ground surface velocity in nanometers per second, the third column (H) is the total landslide thickness in meters, the fourth column (Y) is the height of the yield surface above the basal surface in meters, and the fifth column (T) is the thickness of the plug-flow region in meters, the sixth and seventh column (f_1, f_3) are the calculated values of the rheological parameter for the flow index equal to 1 and 3, respectively, and the last column is the reference for the depth-velocity profile used to calculate the previous columns.

Location	U[10^{-9} m/s]	H[m]	Y[m]	T[m]	$f_1(n=1)$	$f_3(n=3)$	ref.
The Causcasus	3.1	3.5	2.1	1.4	0.8	0.74	Ter-Stepanian (1965)
Costal California	4.95	10.0	1.5	8.5	0.95	0.94	Gould (1960)
Sheridan Wyoming	0.345	4.8	1.0	3.8	0.93	0.91	Chleborad (1980)
Humbolt California	0.3	7.5	3.0	4.5	0.87	0.83	Iverson (1985)
French Alps	77.	4.2	1.8	2.6	0.86	0.82	Van Asch and Van Genuchten (1990)
Southern Switzerland	1.3x10^3	11.0	9.5	1.5	0.71	0.65	Mainsant et al. (2012)
Southeastern France	1.4	8.9	5.3	3.6	0.80	0.74	Malet and Maquaire (2003)

Chapter 2

Supporting Information for “3D surface deformation derived from airborne interferometric UAVSAR: Application to the Slumgullion Landslide”

Contents of this file

1. **Table S1: Detailed Metadata of all interferograms used.**
2. **Figure S1: May Velocity Components.**
3. **Figure S2: May Velocity Component Error Estimates.**
4. **Figure S1: July Velocity Components.**
5. **Figure S4: July Velocity Component Error Estimates.**

2.1 Introduction

Included in this supplement are the metadata for all UAVSAR interferograms used in this study. We also report here the individual velocity component results and corresponding errors for May 2012 and July 2012 3D velocity inversions.

Table 2.1: Metadata for interferograms used in analysis. The first column denotes the temporal dataset that is included. The second column denotes the RPI product which can be downloaded from the Alaska Satellite Facility (ASF, https://www.asf.alaska.edu). The third and fourth columns are the acquisition start times for pass 1 and pass 2 respectively, and the fifth column is the flight line ID as in Table 2.

Ref. Name:	**RPI Product:**	**Pass 1:**	**Pass 2:**	**Flight line ID:**
4/12	`Slumgl_03501_12016-001_12019-001_0007d_s01_L090`	Apr 16, 2012	Apr 23, 2012	03501
4/12	`Slumgl_12502_12016-003_12019-003_0007d_s01_L090`	Apr 16, 2012	Apr 23, 2012	12502
4/12	`Slumgl_21501_12016-000_12019-000_0007d_s01_L090`	Apr 16, 2012	Apr 23, 2012	21501
4/12	`Slumgl_30502_12016-002_12019-002_0007d_s01_L090`	Apr 16, 2012	Apr 23, 2012	30502
5/12	`Slumgl_12502_12026-003_12028-006_0008d_s01_L090`	May 9, 2012	May 17, 2012	12502
5/12	`Slumgl_03501_12026-001_12028-004_0008d_s01_L090`	May 9, 2012	May 17, 2012	03501
5/12	`Slumgl_21501_12026-000_12028-005_0008d_s01_L090`	May 9, 2012	May 17, 2012	21501
5/12	`Slumgl_30502_12026-002_12028-007_0008d_s01_L090`	May 9, 2012	May 17, 2012	30502
7/12	`Slumgl_03501_12064-000_12067-001_0008d_s01_L090`	Jul 24, 2012	Aug 1, 2012	03501
7/12	`Slumgl_12502_12064-002_12067-003_0008d_s01_L090`	Jul 24, 2012	Aug 1, 2012	12502
7/12	`Slumgl_30502_12064-003_12067-004_0008d_s01_L090`	Jul 24, 2012	Aug 1, 2012	30502

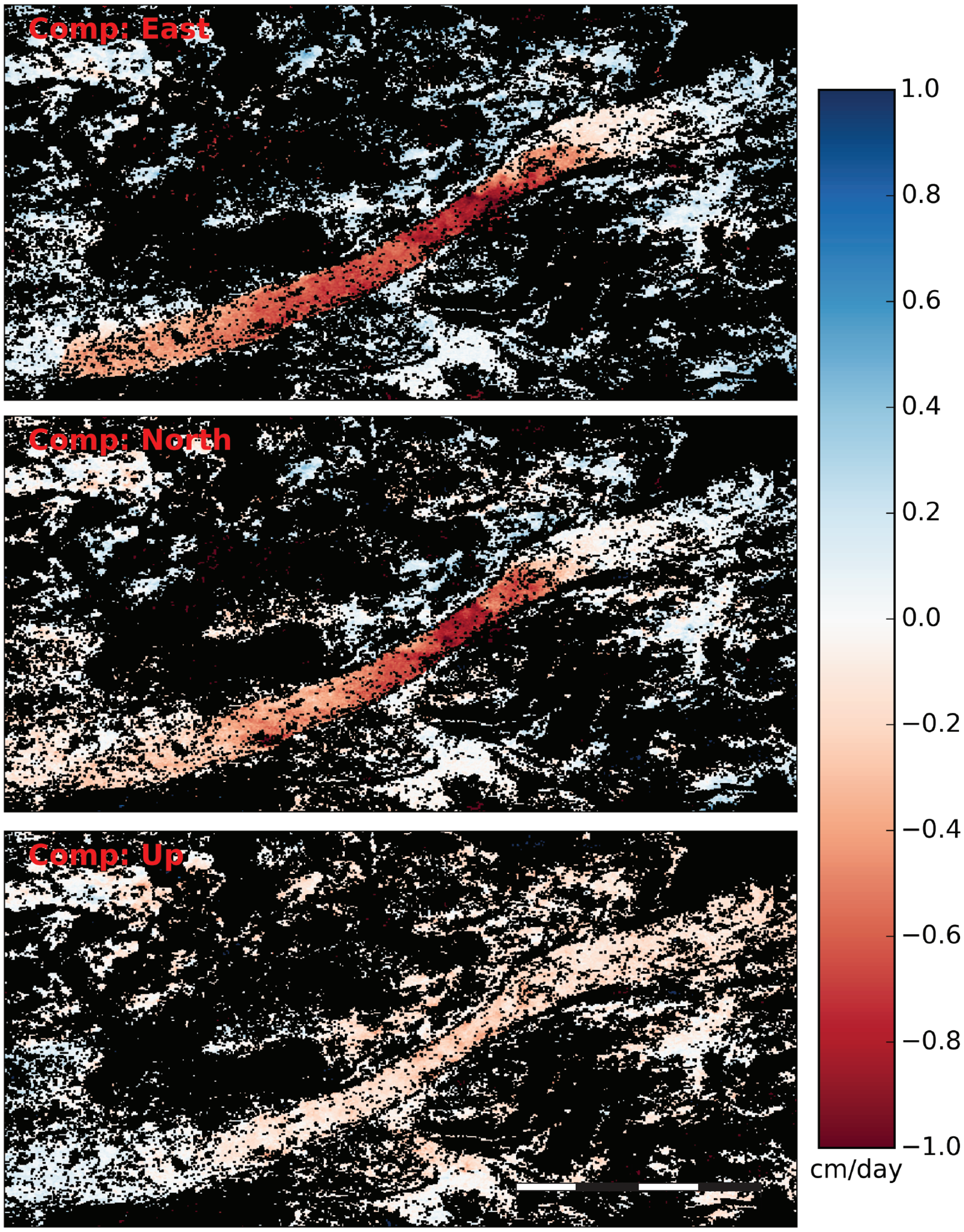

Figure 2.1: Results of the 3D vector inversions of the four May 2012 LOS images. The color ranges from red to blue corresponding to velocities ranging from -1 to 1 *cm/day*. The black pixels represent regions of large covariance in the inversion, and have estimated horizontal errors greater than 1 millimeter per day. The three panels show the magnitude and sign of the individual velocity components East, North and Up, respectively.

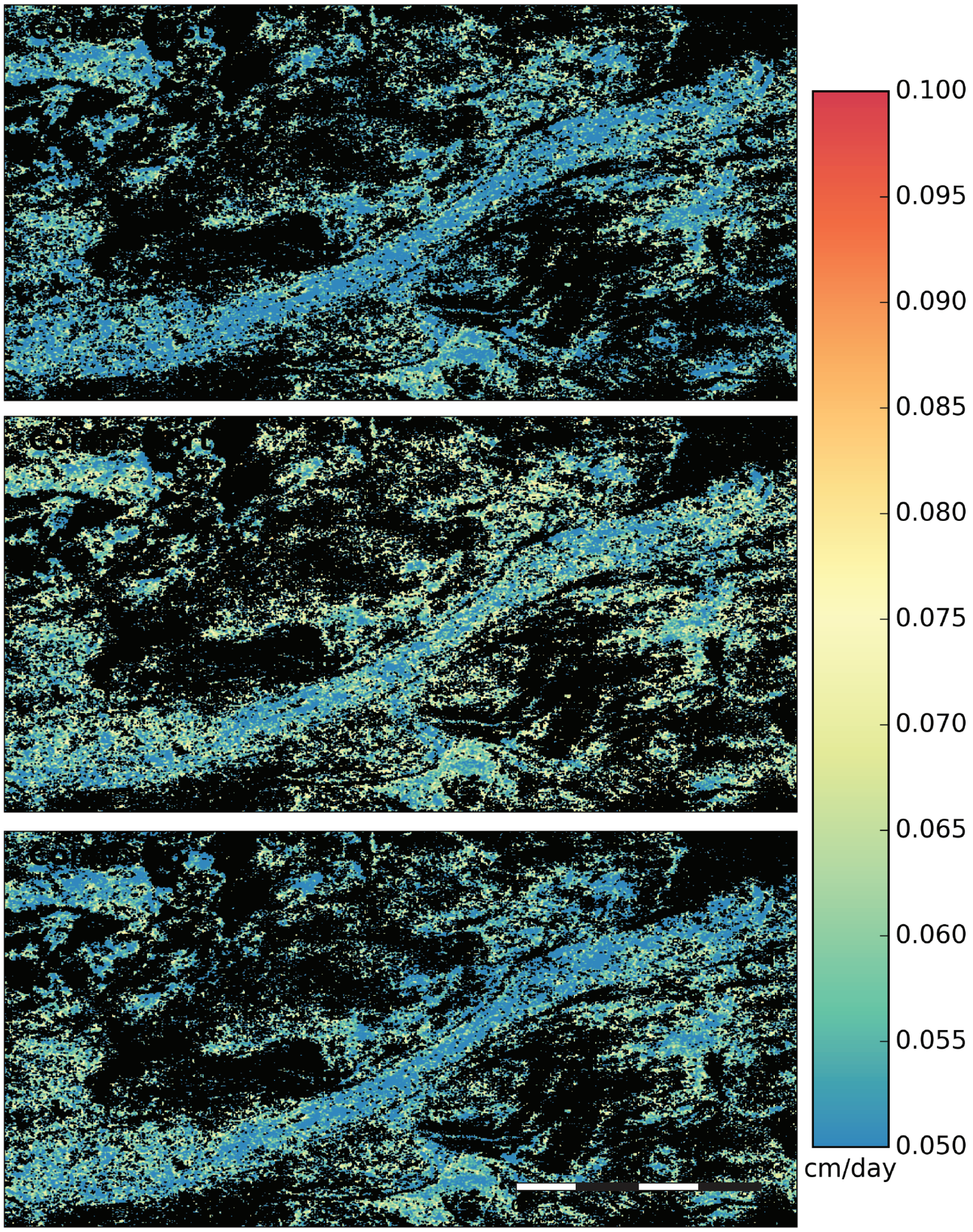

Figure 2.2: Velocity error estimates associated with the May 2012 3D vector inversions. The color ranges from red to blue corresponding to errors ranging from 0.1 to 0.05 *cm/day*. The black regions in each panel denote masked-out regions in which the error estimated for that component exceeds 1 millimeter per day. The three panels show the components East, North and Up respectively.

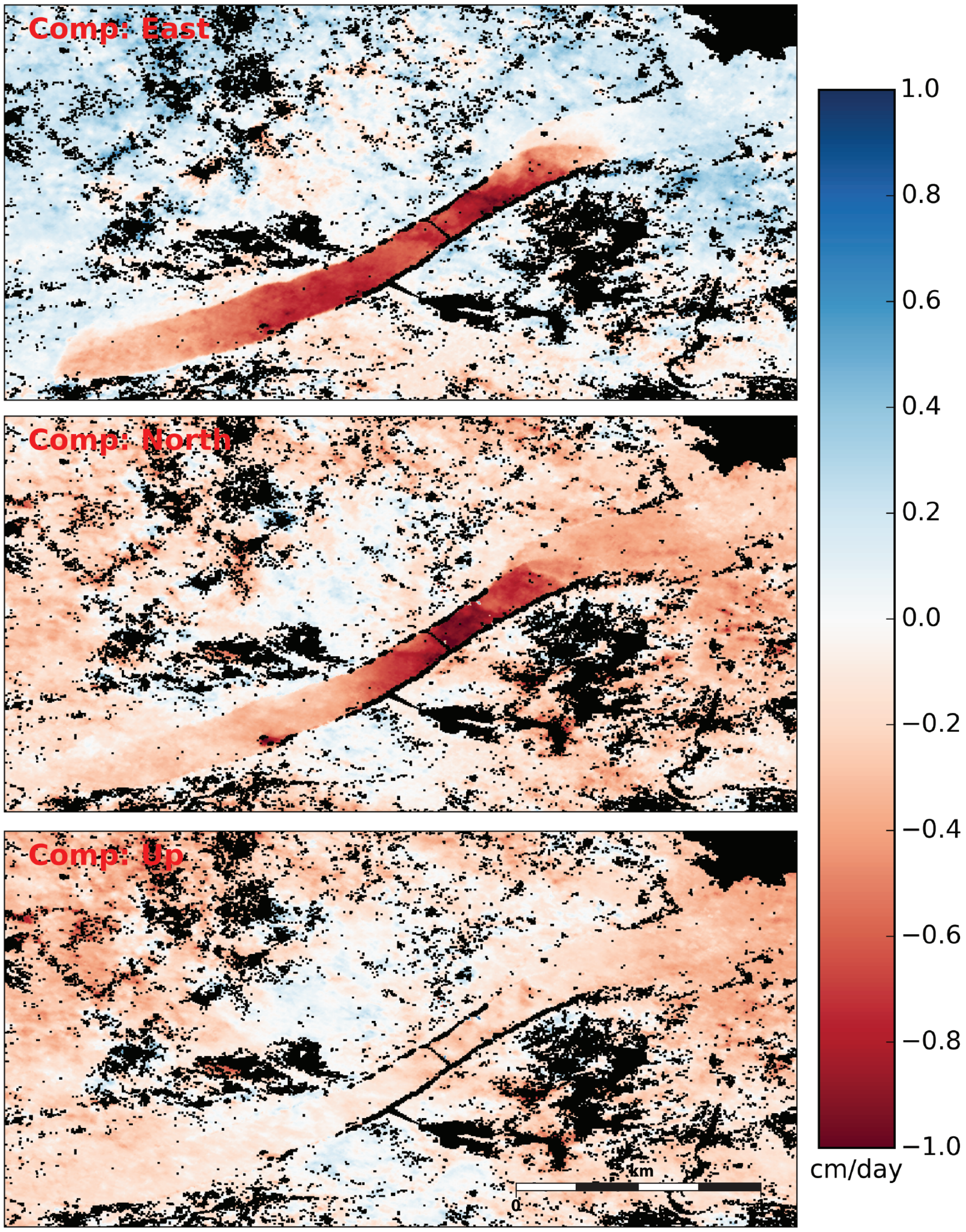

Figure 2.3: Results of the 3D vector inversions of the three July 2012 LOS images. The color ranges from red to blue corresponding to velocities ranging from −1 to 1 *cm/day*. The black pixels represent regions of large covariance in the inversion, and have estimated horizontal errors greater than 1 millimeter per day. The three panels show the magnitude and sign of the individual velocity components East, North and Up, respectively.

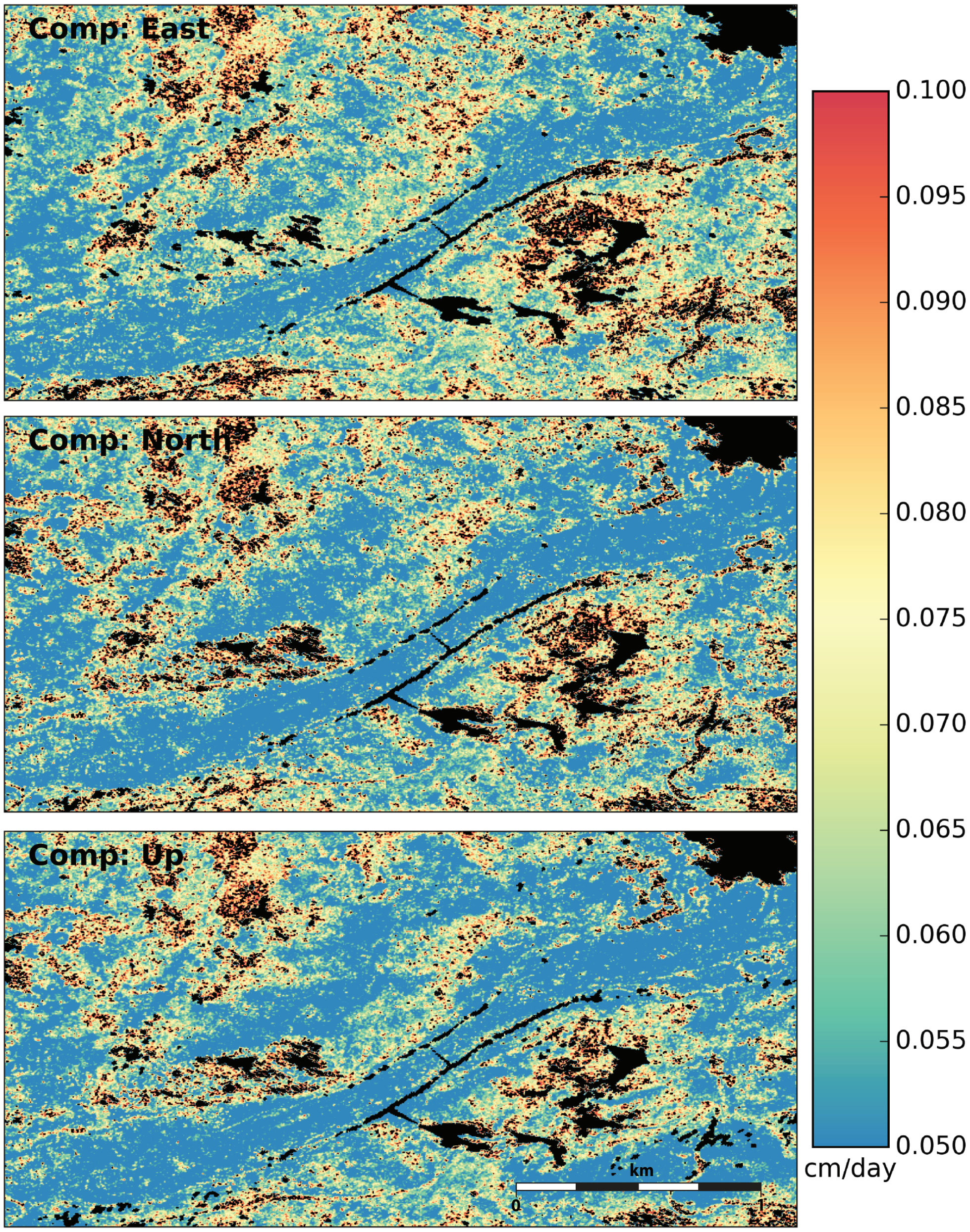

Figure 2.4: Velocity error estimates associated with the July 2012 3D vector inversions. The color ranges from red to blue corresponding to errors ranging from 0.1 to 0.05 *cm/day*. The black regions in each panel denote masked-out regions in which the error estimated for that component exceeds 1 millimeter per day. The three panels show the components East, North and Up, respectively.

Chapter 3

Temporal variation of intermediate-depth earthquakes around the time of the M9.0 Tohoku-oki earthquake

3.1 Abstract

The temporal evolution of intermediate depth seismicity before and after the 2011 M 9.0 Tohoku-oki earthquake reveals interactions between plate interface slip and deformation in the subducting slab. We investigate seismicity rate changes in the upper and lower planes of the double seismic zone beneath northeast Japan using both a β-statistic approach and a temporal epidemic type aftershock sequence(ETAS) model. We do not observe an anomalous precursory increase in intermediate-depth earthquake activity preceding the mainshock, however, following the mainshock we observe a rate increase for the intermediate-depth earthquakes in the upper plane. The average ratio of upper plane to lower plane activity and the mean deep aseismic slip rate both increased by factor of two. An increase of down-dip compression in the slab resulting from coseismic and postseismic deformation enhanced seismicity in the upper plane, which is dominated by events accommodating down-dip shortening from plate unbending.

3.2 Introduction

The locked zone between subducting and overriding plates hosts the largest earthquakes, including all the recorded events of moment magnitude (M) 9.0 or larger. However a large percentage of subduction zone earthquakes are intraslab events that occur within the subducting plate rather than along the plate boundary. These earthquakes are often damaging events that pose a seismic hazard to large populations along convergent boundaries across the globe. In general, we have a limited understanding of the physical mechanisms controlling the generation and occurrence of these events due to a lack of direct observation of composition, in-situ stress state and insufficient understanding of their spatiotemporal distribution.

Previous studies have proposed models for the mechanisms controlling the large-scale stress regimes generated during the subduction process and the relation between intermediate-depth earthquakes and events on the plate boundary subduction thrust (Dmowska et al., 1988; Thatcher and B., 1984; Lay et al., 1989). In these models stresses are generated by the episodic locking of the upper part of the plate that only slides during large megathrust events. As the slab subducts into the surrounding mantle, a static stress field is generated by bending and unbending, slab-pull, and viscous resistance. The time varying stresses are superimposed on the static stress fields resulting in a temporally pulsating stress field. A mechanical model of the coupled subduction zone is presented by Dmowska et al. (1988), which argues for increased rates of intermediate-depth events indicating down-dip extension prior to large interplate thrust events on timescales of months to years. This increase in the occurrence of extensional intraplate earthquakes in the subducting slab reflects the long-term stress cycle of the megathrust. On much shorter time scales (minutes to months) similar models suggest that transient slip down-dip from the megathrust rupture zone results in diminished tensional stresses within the subducting slab (e.g. Thatcher and B., 1984; Dmowska et al., 1988), and furthermore, this slip could act as a precursor to the main rupture (Obara and Kato, 2016). Thus, we expect an overall increase in the down-dip tensional stress during the interseismic period, which is released over short timescales prior to, during and following the mainshock. Lay et al. (1989) examined global seismicity for temporal variations of intraplate seismic activity in the vicinity of large interplate thrust events. They show that the intermediate-depth seismicity rates exhibit strong spatiotemporal variations following large interplate thrust events and a transition from down-dip tension to down-dip compression caused by several great subduction thrust earthquakes.

Beneath the northeastern Japan arc (Tohoku region), intraslab earthquakes occur at depths of 50-200 km within the subducting slab. These events form two inclined parallel planes of seismicity separated by 35 km which delineate the plate curvature as it subducts into the surrounding mantle. At depths >70 km beneath NE Japan the earthquake focal mechanisms of the upper plane predominantly reflect down-dip compression, while the lower plane events reflect down-dip extension (Igarashi, 2002). Using 2002-2007 focal mechanism data from the Kiban observation network, Kita et al. (2010a,b) relocated the hypocenters at depths of 20 - 300 km beneath NE Japan and defined the location of a stress neutral plane between the double-layered seismic zone. A schematic interpretation is shown in Figure 1c of the relocations and the stress inversion results from Kita et al. (2010a,b).

A recent seismicity analysis by Bouchon et al. (2016) suggests that the stress field associated with slab-pull should not be considered a static background stress, but instead can vary temporally and directly or indirectly modulate both intermediate-depth and shallow earthquake activity. They analyze the intermediate-depth earthquake activity prior to the 11 March 2011 M 9.0 Tohoku-Oki earthquake and suggest that a two-month-long period of accelerated seismicity within the subducting slab occurred synchronously with shallow foreshock activity near the Tohoku-oki earthquake hypocenter. Kato et al. (2012) used foreshocks and small repeating earthquakes to show that an increase in shallow seismicity was driven by slow slip near the mainshock rupture area. Ocean bottom pressure gauge data also support this idea (Ito et al., 2013). Bouchon et al. (2016) propose that the slab was transiently "stretching" and "plunging" below the rupture area of the Tohoku-oki earthquake and that this mechanism may more generally act as a nucleation phase for large megathrust earthquakes. The key difference between this new model and the previous studies is the source of the time-varying stress field. Bouchon et al. (2016) suggest that the temporal variation comes from transient deformation (over short timescales) within the slab, which increases the tensional stresses within the plate down-dip of the megathrust and promotes slip on the shallow plate interface. This is in contrast to the alternative view (e.g. Dmowska et al., 1988) that slip may initiate along the down-dip portion of the locked interface, which would result in increased down-dip compression within the subducting plate.

In this study we examine the spatiotemporal variation of the intermediate-depth earthquake activity in the Tohoku region prior to and following the M9.0 rupture. We expect the increase in down-dip compressional stress associated with the M9.0 mainshock (10 - 100 kPa (Hu et al., 2016)) to increase seismic activity in the down-dip compressional upper plane and suppress activity in the down-dip extensional lower plane. We examine seismicity rates in the layers to test whether the observations indicate an increase or decrease in the down-dip tensional stresses, before and after the Tohoku-oki earthquake.

3.3 Data and Methods

3.3.1 JMA Hypocenters and Slab Geometry

To examine the temporal changes of seismicity within the subducting Pacific Plate we analyze earthquake hypocenters from the Japan Meteorological Agency (JMA) catalog. The JMA catalog utilizes the Kiban Observation Network that was completed in 2002 and now includes more than 1200 stations and records 100,000 events per year in Japan. The magnitude of completeness (M_c) in the Pacific slab beneath northeastern Japan is $M1.2$ (Kita, 2009) and increases to $M3.0$ near the trench (Nanjo et al., 2010). We determine M_c before and after the $M9.0$ mainshock for the deep intermediate depth earthquakes (60 -300 km) located within the transect shown in Figure 1 using goodness-of-fit (GFT) (Wiemer and Wyss, 2000) and maximum curvature (MAXC) (Wiemer and Katsumata, 1999). Prior to the mainshock we find a magnitude of completeness of $M1.4 \pm 0.3$ from GFT and M1.15 from MAXC (Figure S1a-S1c). Following the mainshock we find that the magnitude of completeness increased to $M1.9 \pm 0.3$ for GFT and $M2.17$ from MAXC(Figure S1d-S1f). Figure S2 shows the magnitude of completeness versus time. With the exception of a brief excursion in March 2007 and directly following the M9.0 mainshock, the temporal Mc estimates fall within the pre- and post- mainshock estimates (Figure S3). During the period directly following the mainshock we also observe a sudden increase in the minimum measured magnitude (Figure S4); both the increased magnitude of completeness and minimum measured magnitude return to the post-mainshock average values within 6 months.

In the Tohoku region, interplate thrust events are limited to depths <60 km (Igarashi et al., 2003; Kita et al., 2010a). The events used in this analysis are shown in map view and cross section in Figure 1 for a 200-km-wide transect centered on the epicenter of the 2011 M 9.0 Tohoku-oki mainshock and approximately parallel with the slab dip (azimuth 275°). In order to determine the spatial distribution of earthquakes within the slab we utilize a high-resolution slab geometry model of the plate interface. The shallow portion of the plate interface (<60 km depth) is determined from the location of low-angle thrust-fault events and repeating earthquakes (Igarashi et al., 2003; Uchida et al., 2003, 2009)and the deeper interface is resolved in large part from converted SP seismic waves (Zhao et al., 1997) and hypocenters (Kita et al., 2010b). We omit earthquakes located within the overriding continental wedge and limit our analysis to the subducting slab using the plate-interface geometry (Figure 1). We calculate the minimum perpendicular distance of each hypocenter to the slab interface and select events within the slab using this distance, which we refer to as the plate-interface depth (Zhao et al., 1997; Kita et al., 2010b,a). The geometric selection process results in 7,883 intermediate-depth (60-220 km) events and 22,392 shallow (0-60km) events with magnitude greater than M1.2 from March 2006 to October 2015. We further separate the intermediate-depth region into two distinct planes of seismicity based on the location of the neutral plane (plate-interface depth of 22 km as shown by dashed line in Figure 1b) defined by Kita et al. (2010b,b). We select 5,257 events in the compressional upper plane with a plate-interface depth <22 km and 2,626 events in the extensional lower plane with a plate-interface depth >22 km.

3.3.2 Seismicity Rates

The seismicity is analyzed using three methods to determine temporal rate variations. First we examine the earthquake activity spanning the time of the M 9.0 mainshock by estimating the earthquake occurrence rate as a function of time using a 30-day bin width with a 12-hour step for a lower-magnitude cutoff of $M \geq 1.5$ to $M \geq 3.0$ with a 0.5 magnitude step for all cataloged events in the target volume (Figure 2a). All moving averages calculated in this study use an adaptive moving window to avoid averaging across a discrete change point (t_c), to avoid mixing preshock and postshock behavior (Pollitz et al., 2012; Johnson et al., 2015). Earthquake occurrence rates are estimated at discrete times (t_i) with a moving window half-width of T_{hw} (here 15 days). For all times before the change point ($t_i < t_c$) the moving average bins are defined as $[t_i - T_{hw}\ , min(t_c, t_i + T_{hw})]$ and for times after the change point ($t_i > t_c$) the bins are defined as $[max(t_i - T_{hw}, t_c),\ t_i + T_{hw}]$. Additionally, we compare the cumulative number of events during the time of interest to the linear background rate estimated using both 1 and 5 years prior to the time of the M9.0 mainshock (Supplement Figure S1).

Second, we investigate seismicity changes using the β-statistic approach (e.g. Hough, 2005; Matthews and Reasenberg, 1988; Reasenberg and Simpson, 1992). Beta is defined as $\beta = \frac{N_a - N_e}{\sqrt{\nu}}$, where N_a is the number of earthquakes in a given time window, N_e is the expected number of earthquakes in a given time window (average event rate times length of window), and ν is the variance of earthquakes estimated from the distribution of events in reference time period. Similar to our first analysis we use an adaptive moving window with a 60-day half-width and a reference period from 12 March 2006 to 1 January 2011. The Beta values will be positive when the seismic rate is higher than the background seismicity rate and negative when it is lower. Additionally, we specifically test for the rate change proposed by Bouchon et al. (2016) on 13 January 2011 using the seismicity from 13 January 2011 to 9 March 2011 compared to the year prior to 13 January 2011 for a wide variety of geometry and catalog analysis parameters.

Third, the seismicity is analyzed using a temporal epidemic type aftershock sequence (ETAS) model (Ogata, 1992) shown in Equation 1.

$$\lambda(t) = \mu(t) + \sum_{t_i < t} \frac{K}{(t - t_i + c)^p} 10^{\alpha(M_i - M_c)} \tag{3.1}$$

We compute seismicity rates following Marsan et al. (2013) using an iterative smoothing method to select the model parameters describing the target volume. The observed earthquake rate ($\lambda(t)$) is composed of background events ($\mu(t)$) and dependent events, such as foreshocks and aftershocks. In this study we are interested in observing variations of the background rate through time. The second term of Equation 1 represents the contribution of aftershocks where K is the aftershock productivity, α is the aftershock efficiency, c and p are the Omori decay parameters, and t_i is the time of the i-th event with a magnitude M_i. The best-fit inversion parameters are calculated using the entire catalog and the model parameters are then used to estimate the background seismicity rate curves for the upper and lower planes of seismicity.

During the 2011 Tohoku-oki mainshock there was damage to the Kiban seismic network and in the following months there were many large-magnitude aftershocks. The network conditions and elevated seismicity prohibit the detection of many small events $M < 2$) Kita (2009), therefore we use $M > 2$ events for the ETAS and -statistic analysis. For our analysis we assume that changes to the network affect the detection of low-magnitude events in the lower and upper plane equally. Therefore, in order to compare behavior before and after the $M9.0$ rupture we focus on the ratio of the upper to lower plane seismicity background rates, which we refer to as the intermediate-depth activity ratio. Using the ratio of the seismic activity rates in the upper and lower planes to remove artificial changes in rate resulting from time dependent detection thresholds was first introduced by Igarashi (2002). Additionally, some large magnitude events ($M5 - 6.5$) are known to be missing from the hypocenter catalog for a minimum of 25 hours following the 2011 Tohoku-oki mainshock due to the large number of recorded events and increased background noise levels (Kiser and Ishii, 2013; Fan and Shearer, 2016). While the absence of a few large early aftershocks in the slab would have little effect on rates estimated directly from the catalog, it could bias the ETAS derived background rates. If a large event is missing, the ETAS model rate could be artificially increased by the contamination of aftershocks that were erroneously identified as background events.

3.3.3 Deep aseismic slip rate estimation from repeating earthquakes

In order to explore the interaction between stresses generated by locking of the plate interface and the seismogenesis of intermediate-depth intraplate earthquakes within the slab we examine temporal variations of deep aseismic fault slip constrained from small repeating earthquakes on the plate interface. Repeating earthquakes are thought to occur on small fault zone asperities with failure being driven by aseismic fault slip on the surrounding fault interface Nadeau and Johnson (1998); Uchida and Matsuzawa (2013). In the Tohoku region, repeating earthquakes can provide direct estimates of aseismic fault slip at depth with a spatio-temporal resolution of 20-30 km and 3-12 months, respectively (Uchida and Matsuzawa, 2013). Using a repeating earthquake catalog created by the same procedure as Uchida and Matsuzawa (2013), we estimate the cumulative offsets of the small repeating earthquakes down-dip of the M9.0 Tohoku-oki earthquake. We examine the repeating earthquakes that occur during the five years prior to the M7.3 foreshock. The same transect geometry previously used to select the JMA hypocenters is used to select the 224 repeating events belonging to 94 sequences shown Figure 1. The aseismic fault slip (d) driving each repeating earthquake is estimated using an empirical scaling with seismic moment (M_0) (Nadeau and Johnson, 1998; Hanks and Kanamori, 1979) shown in Equation 2.

$$\log(d) = -2.36 + 0.17\log(M_0) \tag{3.2}$$

To study the time-varying aseismic slip down-dip of the M9.0 Tohoku-oki earthquake we follow the methods described in Uchida et al. (2016) to calculate average slip rates from clusters of repeater sequences. Rather than using the recurrence interval to obtain a slip rate estimate for each event, we calculate the average cumulative slip rate within a given time period by dividing the total cumulative slip within a given time period by the number of repeater sequences and the duration of the time window. We use the adaptive moving window mentioned previously, with a 90-day half-width and 30 day time steps. Due to detection issues previously mentioned, we do not interpret the deep aseismic slip rates during the 180 days directly following the $M9.0$ mainshock.

3.4 Results

3.4.1 Averaged seismicity rates

The 30-day moving-average intermediate-depth earthquake rates from March 2006 through October 2015 for four choices of catalog minimum magnitude thresholds are shown in Figure 2a. We test a range of window sizes from 5 to 100 days and obtain similar results. The rate and cumulative event count curves for minimum magnitudes ranging from $M1.5$ to 3.0 show little to no observable deviation from their average long-term rates prior to the 9 March 2011 $M7.3$ foreshock (Figures 2b and S1), which we refer to throughout as the "pre-foreshock period". A few short-lived excursions from the long-term average in March 2010, April 2011, November 2012, and November 2013 are coincident with a $M5.5$ event at 78 km depth on 13 March 2010, a $M7.2$ event at 66 km depth on 7 April 2011, a $M5.6$ event at 48 km depth on 25 November 2012, and a $M7.1$ at 56 km depth on 26 November 2013. During the two months after the mainshock there is a dramatic drop in the number of small events recorded ($M < 2.0$) that does not recover to constant background levels until May-July 2011 (Figure 2a and S2). For all cutoff magnitudes we find a large sudden increase in the earthquake occurrence rate following the $M9.0$ mainshock, which decays over the following half year to an elevated mean long-term occurrence rate which persists throughout the observation period. The mean rate calculated for events with $M > 2.0$ increased from 0.54 ± 0.2 events per day during the pre-foreshock period to 0.8 ± 0.3 since 12 September 2011, the "post-six-month period". The mean rates and variances of the pre-foreshock and post-six-month periods for all magnitude cutoffs are reported in table S1.

Figure 2b shows the deep intermediate depth occurrence rates with the lower and upper planes respectively. The lower and upper plane shows only minor deviations from the pre-foreshock average rate prior to the $M9.0$ mainshock. Following the mainshock both planes of seismicity show a sudden increase in occurrence rate. During the post-six month period the lower plane returns to it pre-foreshock levels, but with significant variations that that are associated with large deep intraplate earthquakes($M > 6$) located within the lower plane of seismicity. The rate increase observed at the beginning of 2013 is associated with a $M7.3$ event located at 49 km depth on December 7, 2012; the rate increase observed at the beginning of 2014 is associated with a $M7.1$event located at 53 km on November 26, 2013. In contrast the upper plane remains at an elevated occurrence rate through out the remaining observational period. Figure S3 shows the spatial distribution of the elevated rates observed during the excursion that occurred from March 2007 to July 2008, the time period directly leading up to the $M9$ mainshock, and the elevated rates during the post-6 month period. The ratio of upper plane to lower plane occurrence rates, shows significant variation throughout the observational period(Figure 2b).

3.4.2 β - Statistic

Figure 2c shows the calculated β-statistic for the duration of the observational period. We find stable β-statistic values close to zero for both the upper and lower plane events during the pre-foreshock period, suggesting there was little variation from the background rate prior to the $M9.0$ Tohoku-oki earthquake. Following the $M9.0$ mainshock the upper and lower plane seismicity indicate a significant rate change with β-values above 2 for ∼1-year.

Table S2 reports the β-statistic during the period of the proposed rate increase suggested by Bouchon et al. (2016) (13 January 2011 to 9 March 2011). We do not observe a statistically significant deviation in the occurrence rate of intermediate-depth events from the average long-term rate for all magnitude ranges tested. In contrast, we do observe a statistically significant increase in the occurrence rate of shallow events ($<$ 60 km depth) with the largest deviation found using $M \geq 3.0$, (β= 7.60), which is associated with the slow-slip and foreshock episode described by Kato et al. (2012), and Ito et al. (2013). Table S3 shows that the β-statistic results are not sensitive to our choice of analysis parameters (transect width, minimum magnitude, depth range, and reference period length).

3.4.3 ETAS model seismicity rates

The intermediate-depth ETAS derived earthquake background rate for both the upper and lower planes of seismicity within the subducting slab are shown in Figure 3a. Following the M9.0 mainshock we observe a large jump in the background rate of events in the upper plane for 6 months, which then decays to a new background level that is increased to 150% of the pre-earthquake long-term rate. In the lower plane of seismicity the rates remain nearly constant and do not significantly deviate from the long-term trend.

Figure 3b shows the intermediate-depth activity ratio. The ratio of background rates for the upper and lower planes is examined to test for a systematic change in earthquake activity from intraslab stress changes induced by the M9.0 mainshock, subsequent large magnitude aftershocks and postseismic deformation processes. Prior to the mainshock the activity ratio of the upper and lower planes is measured to be 1.4 ± 0.3, implying that the occurrence rate in the upper plane was 40% greater in the upper plane than in the lower plane (Figure 3b, blue dashed line). At the time of the 2011 Tohoku-oki mainshock we see a sharp increase in the seismicity rate with the event-rate ratio elevated for several months following the mainshock before decreasing to an approximately constant ratio. The activity ratio following the mainshock, excluding the 6 months directly following the mainshock, is 2.5 ± 0.1, implying that the occurrence rate in the upper plane now exceeds the occurrence rate in the lower plane by 150%. The average activity ratio during post-six month period was found to be 1.8 times greater than the average during the pre-foreshock period.

3.4.4 Deep aseismic slip rates

The average aseismic slip rate calculated from repeating earthquake sequences down-dip of the Tohoku-oki rupture is shown by the orange curve in Figure 3b. During the 5 years prior to the M7.3 foreshock we observe that the deep aseismic megathrust slip rates were relatively low with an average rate of approximately half the plate convergence rate (4.9 cm/year). Directly following the Sept. 2011 M9.0 mainshock, the deep aseismic slip rate increased to a maximum elevated rate of approximately 7 times the plate convergence rate ($\sim$60 cm/year). During the four years following the mainshock the aseismic slip rate steadily decayed to a final value of 15.8 cm/year (Sept. 2015) and an average post-six month rate of 18.3 cm/year. The average deep aseismic slip rate during the post-six month period was found to be 3.7 times greater than the average rate during the pre-foreshock period. Both before and after the mainshock, quasi-periodic changes in the deep aseismic slip rate roughly correspond to similar variations in the activity ratio. As the rate changes in the repeaters appear to precede those in the activity ratio, this may suggest that variations in the deep aseismic slip can result in observable modulation of deep intraslab seismicity. However, more comprehensive observations and careful modeling are required to test this inference.

3.5 Discussion

3.5.1 Seismicity prior to the M7.3 Foreshock

We have examined the temporal behavior of shallow and intermediate-depth earthquakes near the rupture area of the 2011 M9.0 Tohoku-oki earthquake. We do not observe an anomalous precursory increase in intermediate-depth earthquake activity when selecting reasonable choices of geometry, timespan, and minimum magnitude. Prior to the M7.3 foreshock we observe evidence for an increase in the rate of shallow events, which is thought to be associated with slow slip near the hypocenter of the mainshock (Kato et al., 2012). Neither the earthquake occurrence rate estimates shown in Figure 2a, the individual upper/lower plane occurrence rates shown in Figure 2b, the β-statistic time series shown in Figure 2c, nor the intermediate-depth background rate estimates from the ETAS analysis shown in Figure 3 show the precursory activity reported in Bouchon et al. (2016).

The results of the statistical tests designed to specifically determine the significance of the precursory activity proposed by Bouchon et al. [2016] reported in Table S2 show that there is no evidence for a corresponding change in the rate of intermediate-depth earthquakes. Table S3 shows that this is a robust observation and is not dependent on our choices of geometry or analysis parameters. Figure S2 shows the earthquakes selected from the JMA hypocenter catalog using identical geometries and analysis parameters reported in Bouchon et al. (2016). We are able to reproduce their reported rate increase in intermediate-depth events (depth $>$ 80 km, M$>$ 1.0) and shallow events (depths $<$ 40 km, M $>$ 4.0). However, the increase in intermediate-depth events is only observed for a magnitude cutoff of M1.0 (red curve in Figure S3a). The increase in rate above the background rate is not observed for minimum magnitude cutoffs ranging from M1.5 to M3.0 (Figure S3a). Table S4 reports the -statistic using the geometry and analysis parameters of Bouchon et al. (2016), and qualitatively confirms the observations in Figure S3a ($M \geq 2, \beta \approx 0$). Figure S3b shows that there is no deviation from the long-term average background rate for all magnitude ranges considered when the time period used to estimate the background rate is extended to include the 5-years prior to the M7.3 foreshock.

The precursory "plunge" mechanism proposed by Bouchon et al. (2016) seems to imply an increase in tensile stress prior to the M9.0 mainshock resulting from deep slab processes. We argue that an overall increase in intermediate earthquake rates is not expected to be associated with an increase in down-dip tensional stress due to the heterogeneity of the background stress field in the subducting slab with the upper plane in down-dip compression and the lower plane in down-dip extension. Namely, we expect that a down-dip tensional stress perturbation would result in an increase in earthquake occurrence rate in the lower plane and suppression of earthquake activity in the upper plane. Our results do not indicate such behavior prior to the M 9.0 mainshock. Rather, the ETAS derived rates are consistent with increased down-dip compression during the time of the proposed rate change of Bouchon et al. (2016). We argue that the precursory activity reported by Bouchon et al. (2016) reflect the stress fields associated with long-term mechanical subduction processes late in the earthquake cycle (Dmowska et al., 1988; Uchida and Matsuzawa, 2013) and previously identified precursory shallow slow slip (Kato et al., 2012) rather than short-term precursory extensional accelerations termed “plunges”.

3.5.2 Seismicity following the M9.0 Mainshock

Due to the large rupture area and displacement of the M 9.0 mainshock there is a 10 - 100 kPa increase in down-dip compressional stress following the M 9.0 mainshock in the section of the slab hosting the intermediate-depth earthquakes (Hu et al., 2016). We observe a sharp increase in the ETAS derived upper plane background rates directly following the M 9.0 mainshock. In contrast, the ETAS derived lower plane background rates show little to no deviation from the long-term average. This slight decrease is in contrast with the β-statistic time series results shown in Figure 2c, which suggest that there was a short duration increase in the lower plane occurrence rate following the M9.0 mainshock that can also be seen in Figure 2b. This apparent difference between the ETAS and β-statistic derived rate change is likely due to aftershocks from several large events at the base of the upper plane extending into the lower plane, such as the 7 April 2011 M7.2 earthquake which occurred at a depth of 66km. In this case, ETAS background rates will not increase even if aftershock activity increases seismicity rates within the region.

We interpret the increase in the long-term activity ratio after the Tohoku-oki M 9.0 mainshock as a down-dip compressional static stress increase due to the M9.0 mainshock and subsequent aftershocks and persistent postseismic processes such as aftershocks, afterslip, viscous relaxation, or fluid flow. The persistent and steady elevated rate of deep aseismic slip estimated from repeating earthquakes suggests that longterm afterslip contributes to the elevated activity ratio [Figure 3b, orange curve].

Igarashi (2002) used the activity ratio to study the spatio-temporal changes in the intermediate-depth earthquake activity of NE Japan. They found similar increases in the activity ratio following large plate boundary thrust events. The rupture of the 28 December 1994 M7.6 Sanriku-haruka-oki earthquake exhibited a similar temporal response as the M9.0 Tohoku-oki earthquake. Directly following the mainshock, both earthquakes produced several year-long increases in activity ratio. The intermediate-depth earthquake occurrence rates reported in their study also show modulation by afterslip on the plate interface surrounding the mainshock rupture area.

3.6 Conclusion

We have examined the temporal behavior of intermediate-depth earthquakes near the rupture area of the 2011 M 9.0 Tohoku-oki earthquake. We find that for reasonable choices of geometry, timespan, and minimum magnitude we do not observe an anomalous precursory increase in intermediate-depth earthquake activity. We see no evidence for the precursory rate change proposed by Bouchon et al. (2016) before the 9 March 2011 M7.3 foreshock, but following the M9.0 mainshock we see an increase in the rate of intermediate-depth earthquakes. The rate increase we observe is isolated to the upper plane of the double layered seismic zone. The increase in the intermediate-depth intraslab earthquake activity ratio following the M9.0 mainshock is likely driven by persistent deep aseismic afterslip and other postseismic deformation processes. Further, the activity ratio shows variations throughout the observational period which roughly corresponds to variations in the deep aseismic slip rate revealed by repeating earthquake sequences. In the future, the intermediate-depth intraslab activity ratio should be compared with time-dependent deep aseismic slip estimates from repeating earthquakes such as those from Uchida et al. (2016) over a longer time period and larger spatial extent than considered in this study.

3.7 Acknowledgements and Data

This material is based upon work supported by the National Science Foundation Graduate Research Fellowship under grant DGE1106400 for B. G. Delbridge and C.W. Johnson. The earthquake catalog used in this study is produced by the Japan Meteorological Agency, in cooperation with the Ministry of Education, Culture, Sports, Science and Technology (http://www.data.jma.go.jp/svd/eqev/data/bulletin/hypo.html). The catalog is based on seismic data provided by the National Research Institute for Earth Science and Disaster Resilience, the Japan Meteorological Agency, Hokkaido University, Hirosaki University, Tohoku University, the University of Tokyo, Nagoya University, Kyoto University, Kochi University, Kyushu University, Kagoshima University, the National Institute of Advanced Industrial Science and Technology, the Geographical Survey Institute, Tokyo Metropolis, Shizuoka Prefecture, Hot Springs Research Institute of Kanagawa Prefecture, Yokohama City, and Japan Agency for Marine-Earth Science and Technology. We also used waveform data provided by Hokkaido University, Hirosaki University, Tohoku University, the University of Tokyo (http://wwweic.eri.u-tokyo.ac.jp/harvest/) for the selection of repeating earthquakes.

3.8 Figures

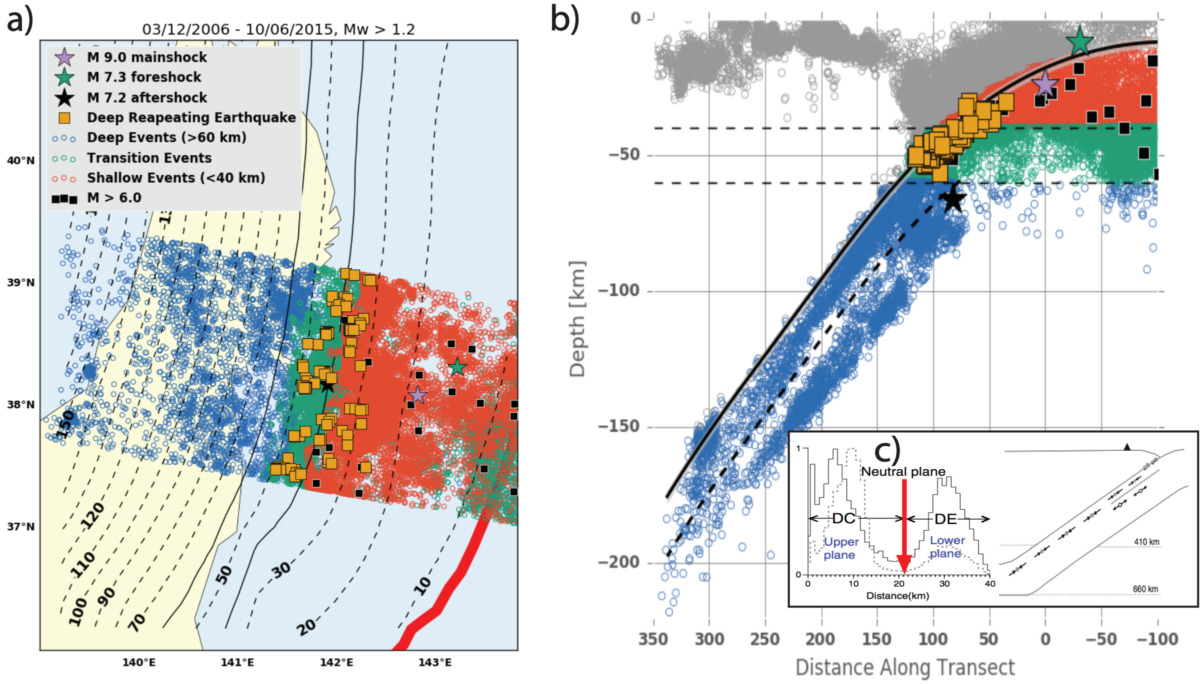

Figure 3.1: JMA hypocenters selected for analysis (a) in map view and (b) in cross-section. Shallow events are defined to have depths less than 40 km (red), and deep events are defined to have depths greater than 60 km (blue). Green and grey circles are events located in the transition depth range (40 âĂŞ 70 km) and overriding plate, respectively, which were not included in the analysis. The purple, green and black stars denote the locations of the 11 March 2011 M 9.0 mainshock, 9 March 2011 M 7.3 foreshock, and 7 April 2011 M 7.2 aftershock. The black squares denote M > 6.0 earthquakes. The orange squares represent the repeating earthquakes used to estimate the deep aseismic slip rate in Figure 3b. The plate interface depth contours are shown by dashed and continuous black lines in (a) [Zhao et al. 1997; Kita et al. 2010]. The solid and dashed black lines in (b) are a smoothed representation of the plate interface within the transect and the location of the neutral plane at 22 km plate-interface depth. (c) Schematic interpretation of stress inversion results for NE Japan from Kita et al. [2010] with the normalized event frequency, including and excluding the aftershocks of the 2003 Miyagi-oki intraplate earthquake. The red arrow denotes the location of the inverted neutral plane. Gray and open dots in the right panel show down dip compression and down dip tension, respectively.

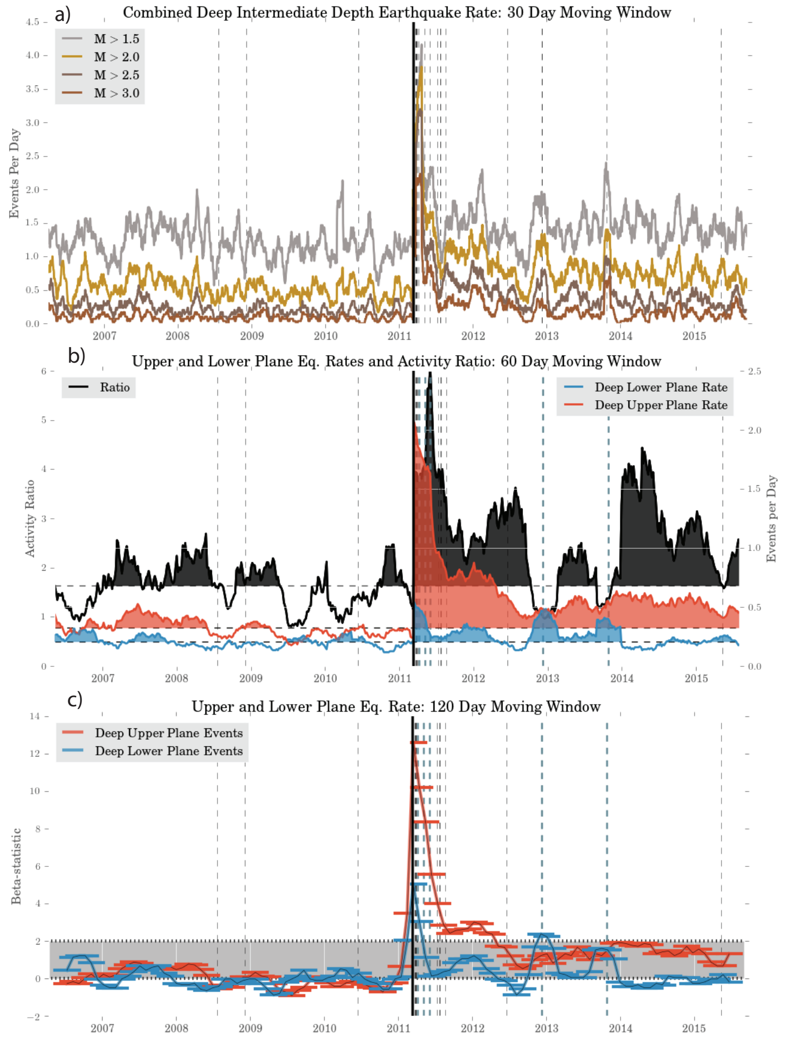

Figure 3.2: Intermediate-depth (60-220 km) intraplate earthquake rate before and after the M9.0 Tohoku-oki Mainshock from March 2006 to October 2015 (a) Intermediate-depth intraplate occurrence rate for a range of minimum magnitudes. The earthquake occurrence rate is calculated using a 30-day moving window and 2-day time steps. (b) Earthquake occurrence rate versus time separated into events in the upper (red) and lower (blue) seismicity planes. The black curve shows the ratio of the rates of upper over lower plane events. The filled regions under the curve denote periods exceeding the pre-foreshock average rate shown by the horizontal dashed black line (c) β-statistic through time using the geometry shown in Figure 1 and a minimum cutoff of M2.0. The red and blue curves represent the results for the upper plane events, and lower plane events respectively. The β-statistic is calculated using a 120-day moving window and 30-day time steps. The vertical black dashed lines show the origin times of large magnitude earthquakes ($M > 6.0$) within the transect. The vertical blue dashed lines show the origin times of large magnitude earthquakes (M>6.0) within the lower plane. The solid black line shows the time of the $M9.0$ March 11 Tohoku-oki mainshock. The horizontal grey region denotes the range of rate change from $\beta = 0$ (no deviation from background rate), to $\beta = 2$ (a statistically significant deviation).

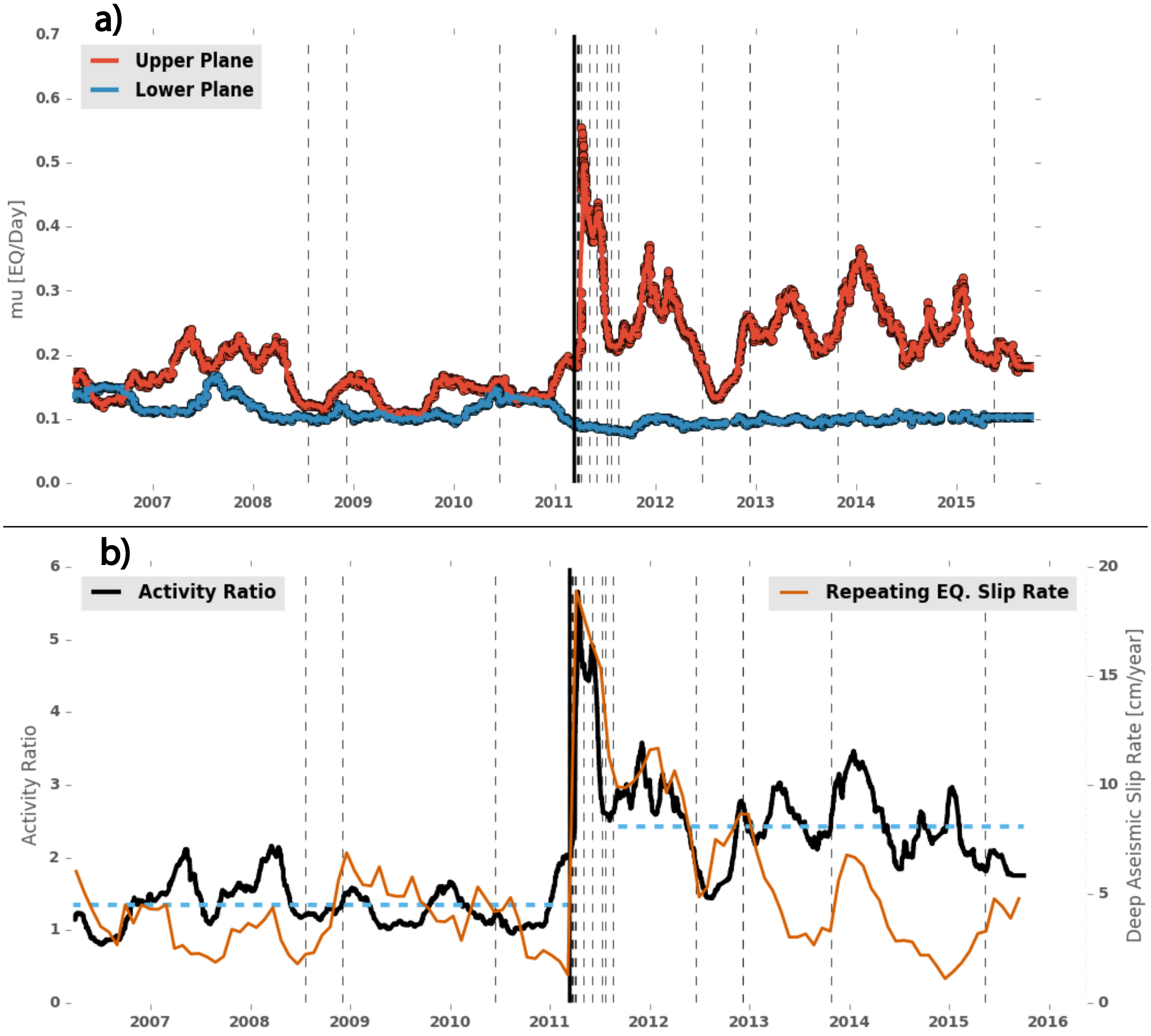

Figure 3.3: Intermediate-depth earthquake rates estimated from the ETAS model using M > 2 events and deep aseismic slip rates. Curves in both panels represent 30-day moving averages with 12-hour steps. (a) The red and blue curves represent background rates for the upper plane, and the lower plane, respectively. (b) The ratio of the background rates of the upper and lower planes, termed the activity ratio, is shown by the black line. The deep aseismic slip rate estimated from repeating earthquakes in Figure 1 is shown by the orange line. The dashed horizontal blue lines represent the average value before and after the M 9.0 Tohoku-oki mainshock, excluding the 6-months following the mainshock. The vertical black dashed lines show the origin times of large magnitude earthquakes (M>6.0) within the transect. The solid black line shows the time of the M9.0 March 11 Tohoku-oki mainshock.

Chapter 4

Supporting information for “Temporal variation of intermediate-depth earthquakes around the time of the M9.0 Tohoku-oki earthquake”

4.1 Comparison with Bouchon et al., 2016

We examine in detail the methods and results of Bouchon et al. (2016). We examine both the temporal and spatial observations of the proposed changes in the occurrence rate of intermediate depth earthquakes prior to and near to the M7.3 foreshock and M9.0 mainshock.

Figure S4 shows the cumulative number of intermediate depth events versus time prior to the mainshock using the geometry used in this study shown in Figure 1. Figure S6 shows the events selected by the spatial regions used in Bouchon et al. (2016), the shallow events are defined as events with depths less 40 km and contained within a 55 km radius around the M7.3 foreshock, and the deep events are defined to be deeper than 80 km within a 90 degree wedge of a circle with a radius of 220 km centered about the M7.3 foreshock in the direction of the down dip azimuth. Figure S3-S7 follows Figure 1a in Bouchon et al., 2016 and shows the cumulative number of events for the year prior to the M7.3 foreshock. Using a minimum magnitude of M1.0 we also see the proposed rate increase during the two months prior to the mainshock (Figure S3a). However, when we calculate the β-statistic measuring the change in earthquake occurrence rate during the two months prior to the M7.3 foreshock (13 January 2011 – 9 March 2011) to the natural rate variations during the previous one-year period (13 January 2010 – 13 January 2011) we find that the rate increase cannot be clearly distinguished from the natural rate variations. We calculated a β statistic of 1.66 for the selection parameters of Bouchon et al., [2016]. For higher values of minimum magnitude, M1.5 to M3.0, the observed rates during the two months prior to the mainshock are nearly identical to the background rate with β-values of approximately 0 [Table S2]. The rate changes are even less anomalous if we increase the reference time period to include the 5 years prior (13 January 2006 - 13 January 2011, Figure S3b). 13 January 2006 - 13 January 2011, Figure S7b). The variability in the beta values in Table S4 are likely related to the magnitude of completeness for magnitude cutoffs with M $<$ 2. The magnitude of completeness for the deep intraplate earthquakes determined in this study is M1.4 $\pm$ 0.3, thus we don't expect the beta statistic to be reliable. For cutoff magnitudes M1.5 $<$ Mco $<$ M3 the results are nearly identical and suggest no change in rate. For the case of Mco = M3 we suspect that the reduction in rate(negative β value) is due to the short time window used.

In order to thoroughly test for a change in earthquake occurrence rate, we systematically vary the key parameters used in our analysis. We vary the minimum depth of intermediate-depth events between 60 and 80 km, the transect width from 100 km to 200 km, the minimum magnitude from M1.0 to M3.0, and the length of the preceding reference time period from 1 year to 5 years prior to the proposed rate change. We do not find evidence supporting an overall increase in rate for all parameter values considered [Table S3].

4.2 Magnitude of Completeness

4.2.1 Maximum Curvature (MAXC):

We first calculate Mc by estimating the curvature of the frequency magnitude distribution (FMD) and estimate Mc from the point of maximum slope. Since the derivative of the frequency magnitude distribution(FMD) decreases strictly monotonically with increasing cutoff magnitude, the maximum derivative is an estimate of the smallest cutoff magnitude not exhibiting the "roll-over" caused by the network missing events. However, following the M9.0 mainshock this method does not provide a robust estimate since the FMD does not strictly decrease and exhibits multiple plateaus at M1.9 and ~M3.

4.2.2 Goodness-of-fit (GFT):

The GFT estimates the magnitude of completeness by determining the lowest cutoff magnitude for which the observed FMD can be matched by a synthetic FMD sampled from the synthetic distribution estimated from the data. We fit the observed dataset to the Gutenberg-Richter Law(G-R) from which we can calculate a PDF from which use to create synthetic magnitude catalogs from which to calculate a synthetic FMD. We report here the details and procedure used to estimate the Mc using GFT. We first fit the data to the Gutenberg-Richter Law which is defined as:

$$\log_{10} N = a - bm, \tag{4.1}$$

where N is calculated data by:

$$N(m) = \sum_{m_i=m}^{\infty} B_i, \tag{4.2}$$

where B_i is number of earthquakes in the magnitude interval defined by m_i and $m \geq M_c$. This can be re-written as:

$$N(m) = \sum_{m_i=0}^{\infty} B_i - \sum_{m_i=0}^{m} B_i. \tag{4.3}$$

The RHS can be interpreted as the total number of events($N(m=0) = N_{Tot} = 10^a$) minus the discrete cumulative distribution(CDF) for the frequency magnitude distribution FMD:

$$N(m) = N(m=0) - CDF. \tag{4.4}$$

We can then calculate the probability density function by taking the derivative with respect to m. In practice we determine N as a function of m from the magnitude catalog and fit the G-R using the SCIPY implementation of the Nelder-Mead simplex algorithm to determine a and b. We then calculate a numerical PDF from the fit G-R parameters and then sample from the PDF until we have a synthetic catalog with the same number of events with magnitude greater than M_{co}. We then bin magnitude to determine the FMD of the data (B_i) and synthetic catalog (S_i). We calculate the residual as:

$$Res = \sum |B_i - S_i| / \sum |B_i|. \tag{4.5}$$

In practice we generate > 20 distributions with the same number of events with $M > M_{co}$ for each. We then determine M_c by choosing the minimum M_{co} with $\langle R \rangle \leq 10$. We estimate error bounds on M_c using min(R) and max(R). Note this sampling procedure is NOT equivalent to using the error from the G-R CDF fit.

4.3 Figures

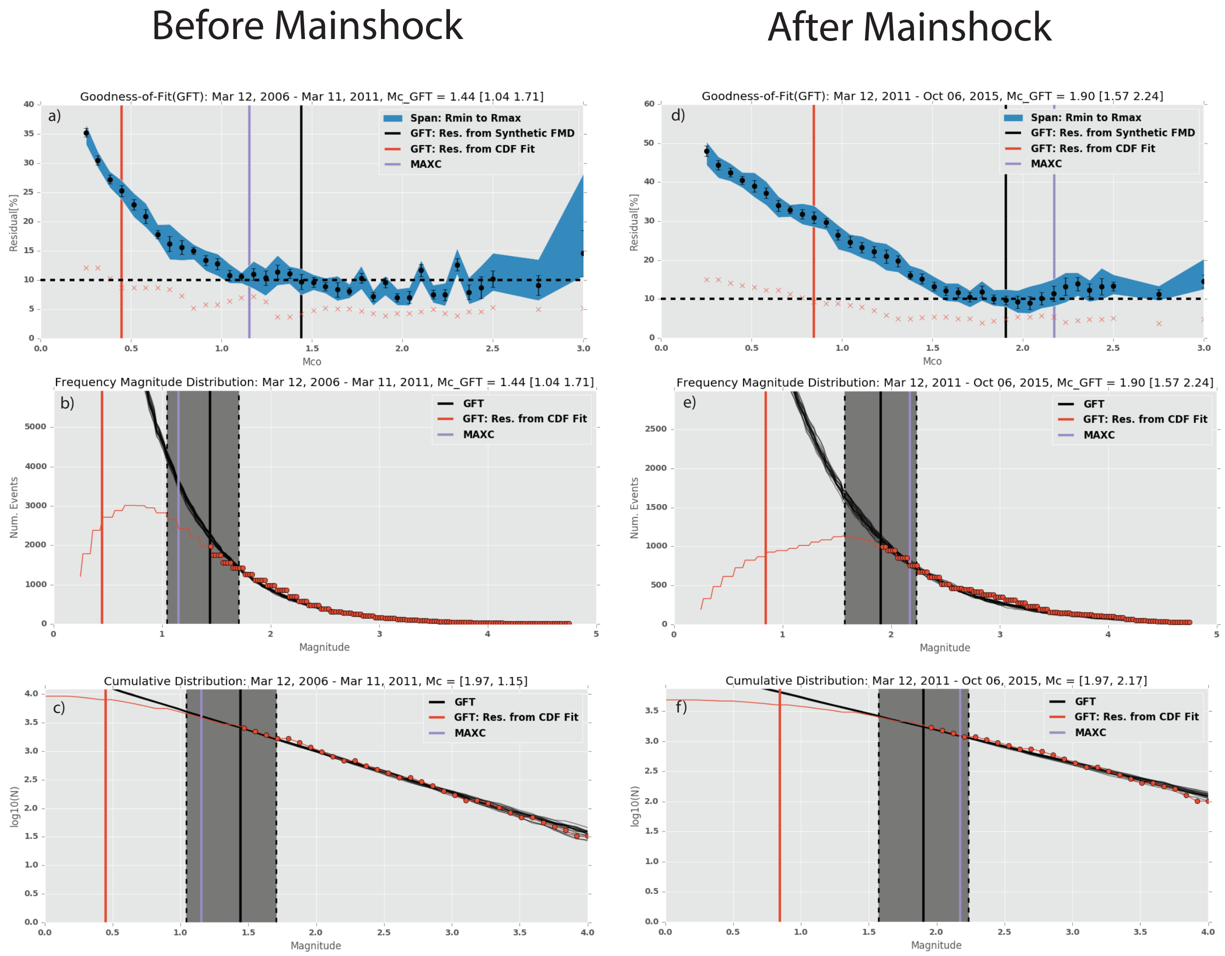

Figure 4.1: Magnitude of completeness before and after the M9.0 mainshock. (a)(d) Goodness-of-Fit as a function of cutoff magnitude. The black circles denote the mean and standard deviation of R. The filled blue curve shows the spread of min(R) and max(R) as a function of Mco which is used to estimate the errors in Mc. The purple and black vertical lines denote the value of Mc determined using MAXC and GFT respectively. The dashed horizontal black line denotes the residual threshold used to select Mc. (b)(e) The frequency magnitude distribution estimated from the data and synthetics. The FMD determined from the data is denoted by the red curve and circles, and each black curve represents a sampled synthetic FMD. The dashed vertical black lines and dark grey region show the range of possible Mc values. (c)(f) log(N) estimated from the data and synthetics. N determined from the data is denoted by the red curve and circles, and each black curve represents N calculated from the synthetic magnitude catalogs. The dashed vertical black lines and dark grey region show the range of possible Mc values.

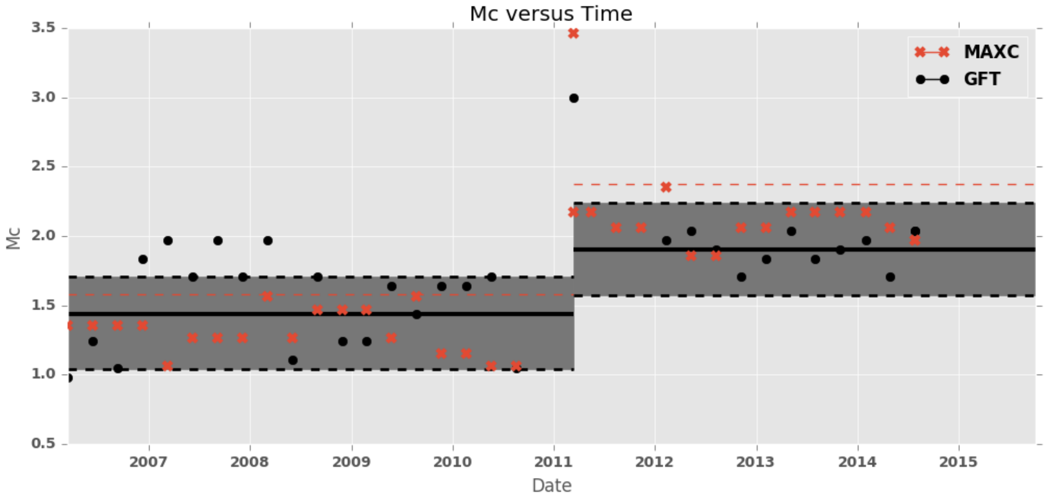

Figure 4.2: Magnitude of completeness versus time. The horizontal black bars denote the average Mc determined from GFT (Figure S1), and the dashed horizontal black lines and dark grey region show the range of possible Mc. The dashed horizontal lines denote the average Mc determined from MAXC (Figure S1). The red x's and black circles denote Mc determined from MAXC and GFT respectively.

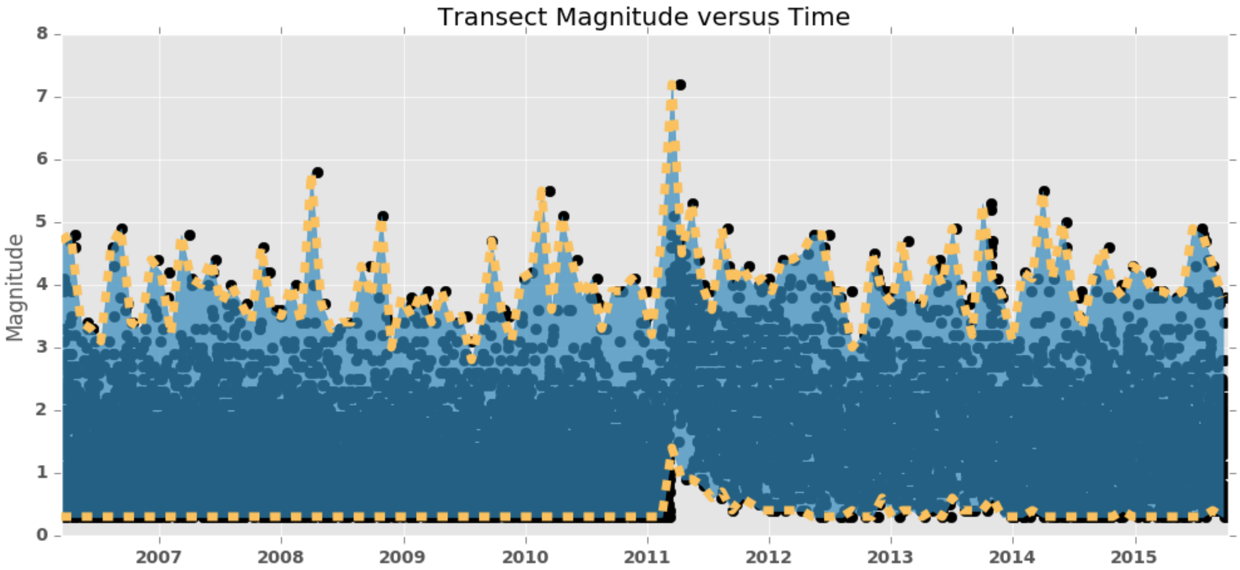

Figure 4.3: Magnitude dependence of deep intermediate depth earthquakes. The black circles represent the magnitude of each deep intermediate depth earthquake (60 âĂŞ 300 km) located within the transect shown in Figure 1. The yellow lines represent the minimum and maximum magnitude within a 30 day moving window, and the blue region shows the magnitude range spanned during each time period.

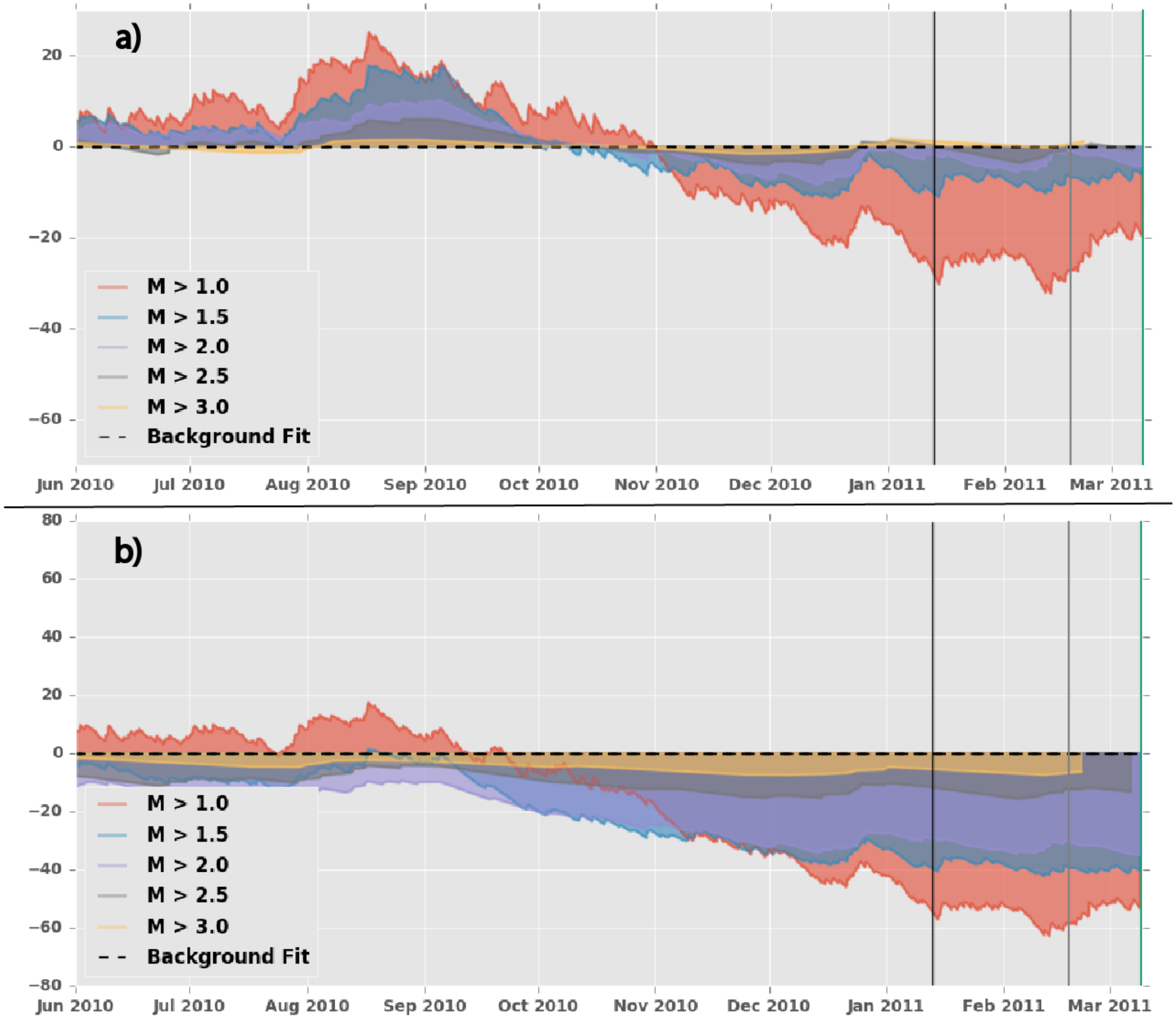

Figure 4.4: Cumulative number of intermediate depth events minus background rate versus time prior to the mainshock using the geometry shown in Figure 1. The black dotted lines show the long-term average rates are determined using the cumulative values of events one year prior to the proposed rate increase on January 13, 2011. The time of the proposed rate increase two months prior to the M 9.0 mainshock by Bouchon et al., [2016] is shown by the vertical black line. The green and purple lines show the time of the M7.3 Tohoku-oki foreshock and the M9.0 Tohoku-oki mainshock respectively. The grey vertical line shows the beginning of the slow-slip (18 February 2011) precedingproceeding the M7.3 foreshock reported by Kato et al. [2012].. The top panel uses the seismicity one year prior to calculate the background rate, and the bottom panel uses the seismicity during the 5 years prior to the M 9.0 mainshock, both panels share the same x-axis.

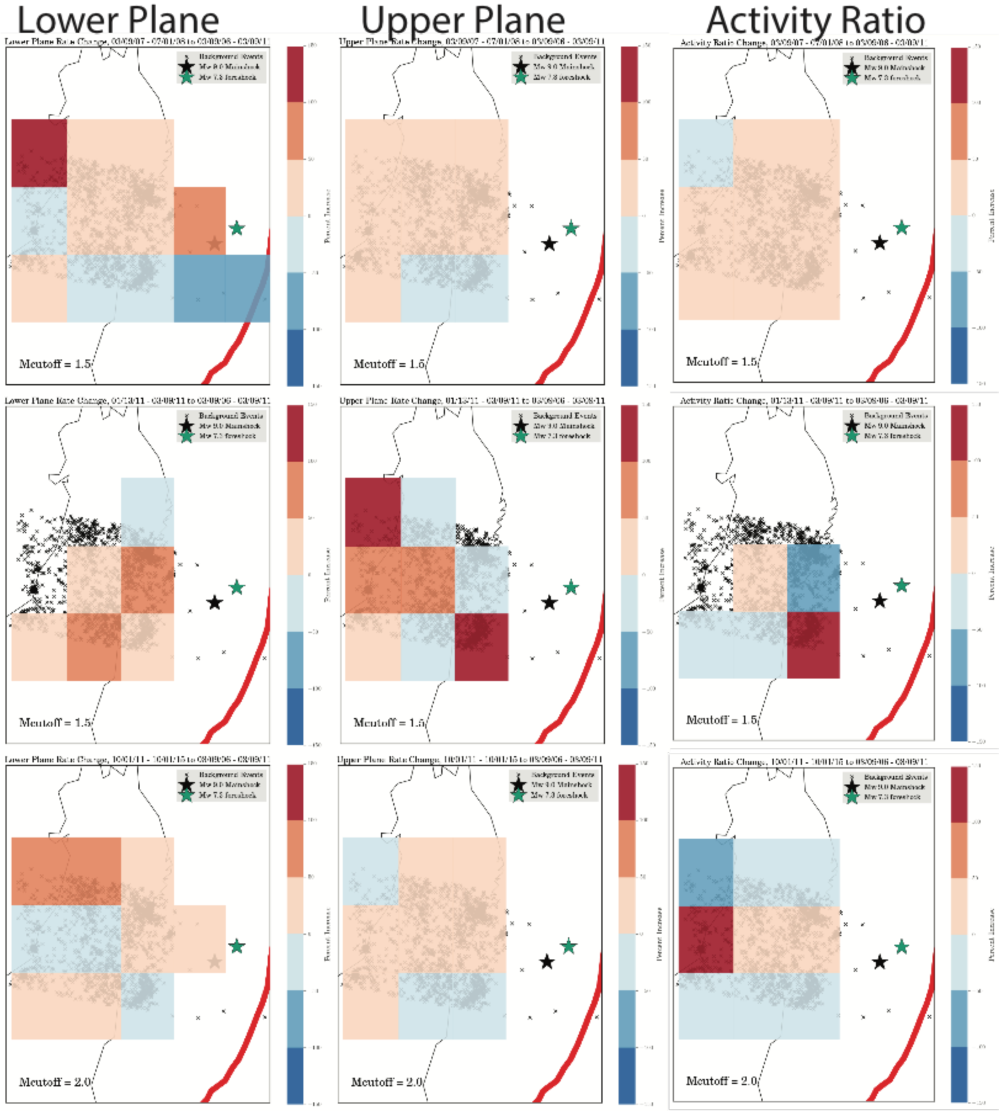

Figure 4.5: Spatial maps of deep Intermediate depth earthquake rate changes (60-300 km) during periods of elevated earthquake rates, activity ratio, and -statistic (Figures 2-3). The reference background rate in each 1 x 1 degree bin was calculated using the pre-foreshock reference period(Jan. 1, 2006 to March 09, 2011), using the earthquakes denoted by black x's, and the cutoff magnitude reported in the lower left-hand corner. The upper row examines the excursion observed to occur from Mar. 2007 to July. 2008, the middle row examines the period of time directly leading up to the M7.3 foreshock, and the bottom row examines the rate variations in the post-six month period. The colors denote the percent change compared to the pre-foreshock period with blue denoting decreasing rates and red denoting increasing rates.

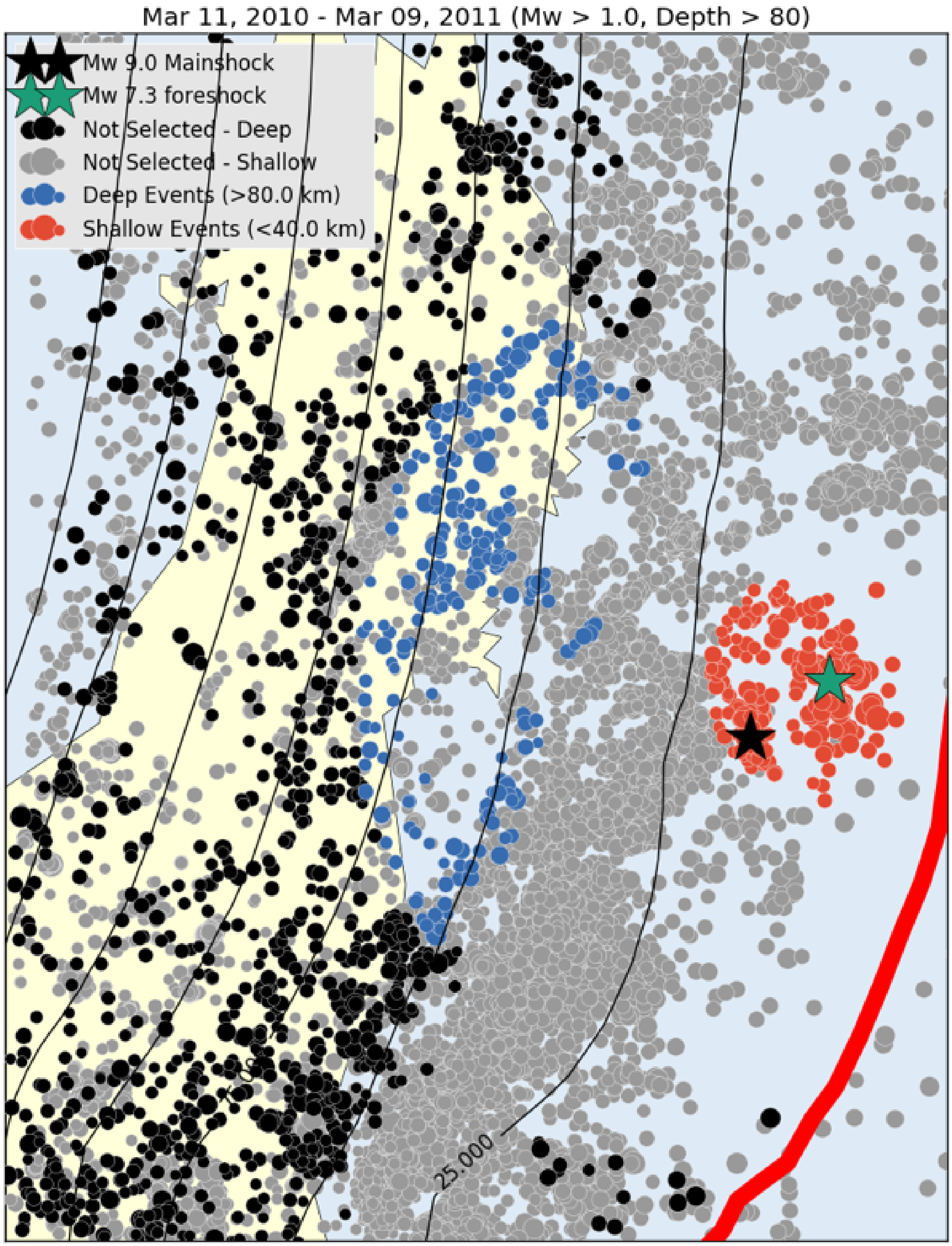

Figure 4.6: Hypocenters selected for analysis following Bouchon et al. [2016]. Shallow events are defined to have depths less than 40 km, and deep events are defined to have depths greater than 80 km. The large black and green stars denote the epicenters of the 2011 M 9.0 mainshock and M 7.3 foreshock. The radius of the circles increases with earthquake moment magnitude, and color denotes selection region; red and blue circles denote shallow and deep events, and the grey and black circles denote shallow and deep events not selected for analysis respectively.

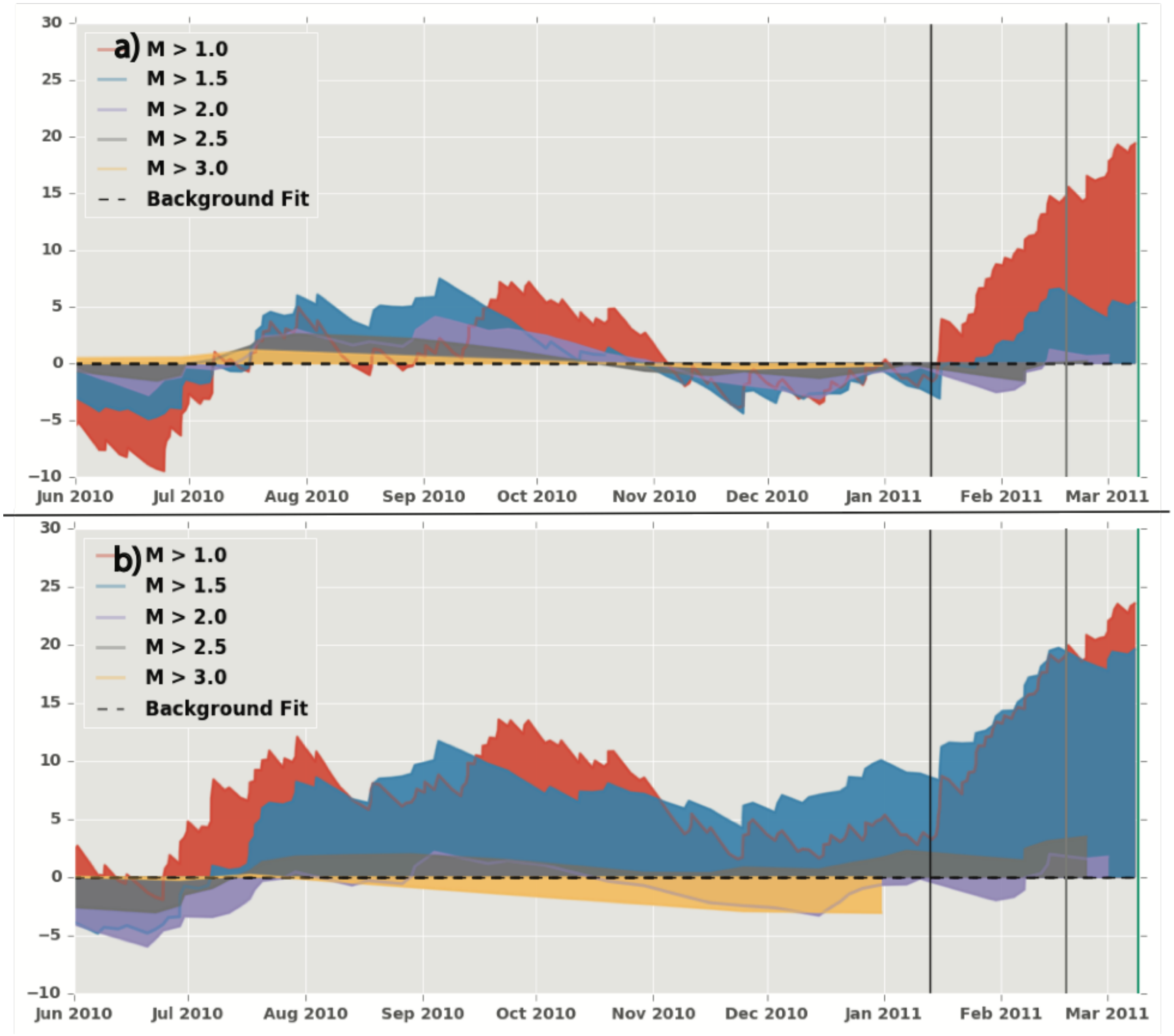

Figure 4.7: Cumulative number of intermediate depth events minus background rate versus time prior to the mainshock using the analysis geometry of Bouchon et al [2016]. The long term average rates are determined using the cumulative values of events one year prior to the proposed rate increase on January 13, 2011. The time of the proposed rate increase two months prior to the M 9.0 mainshock is shown by the vertical black line. The top panel only uses the seismicity one year prior to calculate the background rate, and the bottom panel uses the seismicity during the 5 years prior to the M 9.0 mainshock.

4.4 Tables

Table 4.1: Mean earthquake rate and standard deviation estimated using a 30-day adaptive moving window for a range of magnitude cutoffs. See main text for details of rate estimation and definition of pre and post seismic periods.

	Pre-foreshock Rate[Eq/Day]:	**Post-six month Rate[Eq/Day]:**
M ≥ 1.5	1.21 ± 0.24	1.45 ± 0.26
M ≥ 2.0	0.54 ± 0.16	0.83 ± 0.25
M ≥ 2.5	0.22 ± 0.1	0.22 ± 0.21
M ≥ 3.0	0.09 ± 0.05	0.21 ± 0.16

Table 4.2: Beta statistic measuring the change in earthquake occurrence rate during the two months prior to the M 7.3 foreshock (13 January 2011 - 9 March 2011) to the natural rate variations during the one year prior to (13 January 2010 - 13 January 2011) using the analysis geometry shown in Figure 1.

	Intermediate-depth Events:	**Shallow Events:**
M ≥ 1.0	0.17	2.34
M ≥ 1.5	0.17	4.52
M ≥ 2.0	-0.87	6.51
M ≥ 2.5	-0.49	6.86
M ≥ 3.0	0.14	7.6

Chapter 5

Geodetic constraints of Slow Slip near Parkfield, CA

5.1 abstract

It is thought that large bursts of deep tremor ($>$ 20 km depth) near Parkfield, CA are associated with quasi-periodic shear dislocations on the deep extent of the San Andreas Fault. Slow slip has been discovered in subduction zones worldwide and manifests aseismically as geodetic transients in GPS and seismically as a long duration, low amplitude seismic signal known as tectonic tremor. However, deformation associated with tremor in a transform fault environment has not previously been observed despite the ubiquitous presence of tremors and low frequency earthquakes (LFEs) and targeted attempts to observe this deformation. The strain rates associated with these events are below the detection level of GPS networks. Thus, in order to observe this deformation we have utilized two long-baseline laser strainmeters located in Cholame, CA and the PBO borehole strainmeter network to place a lower upper bound on their moment release. We find that the NVTs and LFEs likely reflect distinct faulting behaviors.

5.2 Introduction

The San Andreas fault(SAF) is one of the few strike-slip faults hosting tremors and low-frequency earthquakes(LFEs). Tremors and LFEs are generally thought to be seismic manifestations of fault-slip, with relatively rapid slip rates occurring on small asperities embedded in an otherwise aseismic slipping region (Beroza and Ide, 2011). LFEs are thought to be small repeating earthquakes representing shear slip on the plate interface. However, they are relatively depleted in high frequencies with low corner frequencies, implying longer durations than regular earthquakes. Similarly, NVTs are rich in low-frequencies and lack an impulsive arrival compared with regular earthquakes. LFE events are often observed to occur in rapid succession, and on the SAF are thought to comprise the majority of tremor signals (Shelly, 2017).

In contrast to the seismic component, aseismic deformation reflects fault slip that is slow enough that both inertial forces and seismic radiation are negligible. The durations of observed aseismic slip events range from days to years, with displacements of up to tens of centimeters (e.g. Peng and Gomberg, 2010). These events are not unique to a specific depth range and occur on faults in a variety of tectonic settings (Figure 5.1). This aseismic slip can sometimes also trigger more rapid slip somewhere else on the fault, such as small embedded asperities. This is thought to be the mechanism for the SAF LFEs and small repeating earthquakes on shallower sections of the creeping San Andreas Fault (e.g. Nadeau and McEvilly, 2004). While the deep extent of the SAF is believed to be creeping, continuous monitoring of seismic activity on the Parkfield section of the SAF suggests a spatio-temporally complex deformation style.

Episodic tremor and slip(ETS) is a recently identified phenomenon in which weak seismic signals(tremors and LFEs) accompany slowly migrating slip on a fault interface. ETS was first identified geodetically from GPS and tiltmeters, and found to occur along the subduction thrust below the locked zone that breaks in regular earthquakes. In Japan and Cascadia, these events occur quasi-periodically with typical periods spanning 3 to 19 months. It is important to note that the discovery of this phenomena was only made possible in the last few decades by increasingly sensitive seismic and geodetic networks. In addition, a variety of slow deformation phenomena have been identified in the past decade in a variety of subduction zones and several continental faults (Obara, 2002; Rogers and Dragert, 2003; Beroza and Ide, 2011). Prior to this study, ETS has been found to primarily occur in subduction zones of young and warm slabs (Figure 5.1).

Understanding stress accumulation in fault zones that fail in large earthquakes is a fundamental challenge in seismology. The region in which ETS occurs, is thought to represent the transition from seismic to aeseismic behavior. Prior to the discovery of slow-slip, faults were thought to relieve stress either through continuous aseismic sliding, as is the case for continental creeping faults (Figure 5.1), or in near instantaneous failure. Since the ETS events occur in the transition zones between freely slipping and locked sections(e.g. Rogers and Dragert, 2003; Obara et al., 2004), the associated seismic signals allow us to directly investigate the time-dependent stress accumulation and release in the deep crust. The transition zone in which the inferred slow-slip zone is located between the southeast and northwest ends of the quasi-regular Parkfield and Fort Tejon locked zones is analogous to the transition zone hosting ETS in subduction zones. Stress transfer to the overlying locked patches may also lead to an increased probability of triggering a large event if this up-dip region is critically stressed (Mazzotti and Adams, 2004; Beeler et al., 2016). Further, it is also known that these events are sensative to small stress purturbations, and can be triggered by passing dynamic waves and modulated by earth tides (Rubinstein et al., 2008; Thomas et al., 2009). In this study we use geodetic measurements to place a quantitative upper bound on the size of the slow slip accompanying large bursts of quasi-periodic tremors and LFEs on the Parkfield section of the SAF. We use a host of analysis methods to try toisolate the small signal due to the slow slip and characterize noise properties. We find that in addition to subduction zones, transform faults are also capable of producing ETSs. However, given the upper-bounds from our analysis, surface geodetic measurements of this slow slip is likely to remain highly challenging.

5.3 Parkfield seismic bursts

5.3.1 Tremors

We used borehole seismometer data from the High Resolution Seismic Network(HSRN) and Tremor Scope Project(TSP) to locate 2865 tremors between 8/21/2001-6/1/2017 on the SAF beneath the northernmost rupture area of the Mw 7.8 Ft. Tejon earthquake of 1857 (Figure 5.2). Approximately 300 hours of tremor data has been recorded at 20 Hz frequency. Using an envelope cross-correlation method (Nadeau and Dolenc, 2005; Nadeau and Guilhem, 2009), we located tremors to a depth range of $10-40$ km. We find that the tremor durations are exponentially distributed with typical bursts lasting ∼5 to ∼20 minutes.The energy in the 3-8 Hz band is roughly equivalent to a $\sim M_w$ 0.5 to 1.5 Earthquake. In addition, we found that tremors were concentrated in cloud surrounding the locked Cholame segment of the SAF. Our location uncertainties at the 95% confidence level are ±4.7 km and ±4.5 km in horizontal direction and depth respectively (Nadeau and Guilhem, 2009). The location of the tremors is shown in map view in Figure 5.2 with the density of tremor locations with depth and along strike shown in Figure 5.3.

We examine the temporal behavior of the tremors located within the box shown in Figure 5.3 and plot the rate of tremor occurrence in Figure 5.4. We observe that the tremor rate is not constant but shows quasi-periodic bursts of high activity wherein the burst rates exceed the background rate by ∼5 times, where the background rate is calculated as the average rate between the bursts. We interpret these burst to be analogous to the seismic component of ETS in subduction zones likely representing failure of small asperities, and being indicative of slow slip on the plate interface. Using the cross correlation method detailed in Guilhem and Nadeau (2012), we identify 82 burst episodes(Table 5.10), with recurrence intervals ranging from ∼ 30-150 days (Figure 5.5). We find that individual burst episodes last 2 to 10 days. Although the duration of individual tremors in these episodes is comparable to that of background tremors, burst tremors occur with an RMS amplitude of tremor episodes that is ∼ 30% percent higher. These short bursts account for about one third (32.7%) of all tremor detections and correspondingly a similar fraction (30.8%) of the total measured tremor duration.

Besides characterizing the general episodic nature of tremor rate, we also examined specific time-periods near known earthquakes. As described earlier, it has been hypothesized that there may be a physical relationship between ETS and large earthquakes with a causal relationship possible in either direction. We find that following the 2004 Parkfield Earthquake, there was no change in the durations of individual tremors. However, there was a large, and persistent increase in the rate of tremor occurrence. The average tremor occurrence rate increased from ∼1.5 mins/day to ∼5 mins/day during the 100 days following the earthquake. In addition, the peak episode rates increased from 6.64 ± 0.9 to 9.10 ± 1.8 (Figure 5.6a). Finally, the average recurrence intervals between burst episodes decreased from ∼70 days to 31 days directly following and persists for approximately one year following the mainshock.

Even more remarkably, we find that the largest burst of tremor observed in our dataset was in response to the Mw 6.0 2014 Napa Earthquake, located nearly 350 km to the North. The peak rate directly following the mainshock was 23.0 min/day, about 10 times the background rate, and twice the average peak rate (Figure 5.6). The average peak tremor rate slowly decayed at a rate of -0.04 mins/day per day (black curve, Figure 5.6b) while the background tremor rate increased to ∼4 mins/day and remained elevated throughout the observational period. To put these changes in context, it is noteworthy that are significant variations in the background rate prior to the earthquake also. Beginning in 2014, the background rate suddenly increased following a burst event on Jan. 21, 2014, and then in July 2014 it began to steadily increase prior to the occurrence of the 2014 South Napa Earthquake. We interpret this sudden change in tremor rate as a large number of smaller overlapping bursts (Figure 5.4; black curve, Figure 5.6b). We find additional peaks in tremor rate to be associated with regional seismicity (distance $\leq$ 350 km) - these are denoted by vertical dashed lines in Figure 5.7. The first dashed line is associated with M_w 4.7 event that occurred ∼210 km away in Central California on Dec. 23, 2013 (Figure 5.7d). This earthquake is associated with a small peak in tremor rate(Figure 5.7a). However, while the earthquake appears to be simultaneously triggering several bursts of tremor across the slow-slip zone, these tremors actually occur prior to the arrival of the surface waves. Thus, we posit that they are likely triggered by bursts of local seismicity which appear to migrate from the outer edges of the slow-slip zone inwards(Figure 5.7c). The second event of interest is a M_w 4.5 event which occurred ∼150 km away in Central California on Nov. 20, 2014 (Figure 5.7b). This event is associated with a large rapid increase in tremor rate (Figure 5.7a), which is spread throughout the slow-slip zone. Finally, the third dashed line is associated with a pair of M_w 4.5 and M_w 4.7 events which occurred approximately ∼4 hours and 50 km apart on Feb. 11, 2014 (Figure 5.7d) approximately 300 km away on the California-Nevada border region. These event doublet generated a large peak of tremor (Figure 5.7a) in the Parkfield section.

5.3.2 Low-Frequency Earthquakes (LFEs)

Low-frequency earthquakes often accompany NVT, occurring in similar locations and frequency content (e.g. Nishide et al., 2000; Ohmi and Obara, 2002; Katsumata and Kamaya, 2003; Hirose and Obara, 2006).Tremor is often thought to represent a superposition of many overlapping LFEs (Shelly et al., 2007). The LFEs used in this study are from the catalog provided by Shelly (2017). Unlike the tremor locations, the LFEs are located on or very close to the SAF fault interface, and are consistent with shear-slip (Figures 5.2, 5.3). The template matching approached used for LFE detection (Shelly, 2009) is reminiscent of the methodology and assumptions used for the detection of repeating earthquakes (Nadeau and Johnson, 1998; Uchida and Matsuzawa, 2013). This suggests that LFEs may represent a deep faulting analog to shallow repeating earthquakes. It is possible that the LFE activity may represent repeating on-fault behavior, with non-repeating and off-fault activity resulting in additional NVT signals with no corresponding âĂIJtemplateâĂİ. We find that most of the detected tremor bursts contain at least one LFE (Figure 5.10). Comparing the 88 template families with the NVT catalog from 2002 to 2017, we find that 98% of the tremors contain an LFE, and that on average a given tremor contains 30 LFEs. However, only 8% of LFEs are contained within an NVT burst.

We examine the temporal behavior of the LFEs located within the box shown in Figure 5.3 and plot the rate of LFE occurrence in Figure 5.8. Similar to our results for the tremor behavior, we observe that the LFEs exhibit quasi-periodic bursts of high activity, with the burst rates exceeding on average 5 times the background rate. However we also note that the episodicity is highly variable, and the LFE distribution is more continuous with depth, suggesting less ETS-like accelerations. Additionally, we also observed a persistent increase in the rate of LFE occurrence following the 2004 Parkfield earthquake (Shelly and Johnson, 2011), with the average background rate increasing from $\sim$30 LFEs/day to $\sim$70/day during the subsequent time-period (Figure 5.8). Analogous to the NVTs, we find the largest increase in LFE rate to be in response to the M_w 6.0 2014 Napa Earthquake. The LFE peak directly following the mainshock has an amplitude of $\sim$ 900 LFEs/day, about a 30 times increase over the background rate and twice the average peak rate(Figure 5.10). However, in contrast to the observed increase in background tremor occurrence rate after the Parkfield earthquake, we do not observe an increase in the background LFE rate. Surprisingly, we in fact observe a steady decrease in the background LFE occurrence rate. This decrease culminates in a $\sim$3-month period of quiescence from December 2014 to February 2015, following which the background LFE occurrence rate returns to its pre-Napa levels.

5.4 Quasi-periodic slow-slip episode characteristics

The 82 quasi-episodic episodes identified using cross-correlation (i.e. Guilhem and Nadeau, 2012), represent periods of increased seismic activity (e.g. LFE and tremor occurrence rates) well above the background rate, and are localized in the slow-slip region in Figure 5.3. Both LFEs and tremors are believed to be associated with deep fault deformation, and are thought to represent small embedded asperities which are driven by otherwise aseismic slow-slip within the surrounding fault (e.g. Obara and Hirose, 2006; Shelly et al., 2006; Peng and Gomberg, 2010; Rubinstein et al., 2007).

Due to the similarity of these quasi-periodic bursts with ETS and slow-slip in subduction zones we propose a simple model to explore the mechanics of this process and predict the size of these ETS events.

We start by assuming that the deformation at depth maintains plate rate. The long-term SAF slip rate in the vicinity of the slow-slip zone, at depths below $\sim$14 km, is $\sim$33 mm/yr and is calculated assuming decoupling from the overlying seimogenic zone (Murray et al., 2001; Murray and Langbein, 2006). The total moment release is given as

$$M_0 = \mu A d, \tag{5.1}$$

where μ is the shear modulus (Assume fixed, 30 GPa), A the area of the slow-slip plane, and d is the amount of slip. If the individual ETS events were identical we could simply divide the cumulative slip by the number of episodes. We follow the procedure commonly used to estimate slip-rates from repeating earthquakes (Nadeau and Johnson, 1998), and assume that the amount of slip(d) is equal to the tectonic loading rate($\dot{S}$) times the recurrence interval preceding the slow-slip event (T_R, column 2, Table 5.1)

$$d = T_R * \dot{S}. \tag{5.2}$$

This results in uniform slip (d) over the entire slow-slip region (A) which is exactly equal to the slip deficit accumulated from tectonic loading. Assuming a fixed slow-slip area (25 km by 15 km) of 375 km^2 (black rectangle, Figure 5.3), and constant deep fault slip-rate ($\dot{S}$), the calculated cumulative slip of 512.4 $mm \sim 15.5\ yr \times 33\ mm/yr$) results in a cumulative moment release or 5.8e+18 or 6.4 M_w. This simple back of the envelope calculation suggest that on average, in order to maintain plate-rate, each episode slips $\sim$ 6.2 mm, and an average geodetic magnitude of 5.2M_w. These values strongly depend on the assumed area of the SSE and the amount of slip accomodated by background activity inbetween the 82 events. While the geodetic surface deformation from several millimeters of slip at this depth may be too small to detect from a single individual event ($5.2 \pm 0.2\ M_w$) , we may be able to observe the cumulative geodetic moment release through proper stacking to utilize the full moment release.

Since the duration and amplitude of each tremor peak is not constant, the slow-slip driving the tremor likely varies from episode to episode. It has been observed in both Japan and Cascadia that the geodetic moment release is likely linearly proportional to the cumulative duration of tremor during a slow-slip event Aguiar et al. (2009); Obara et al. (2010). The empirical relation uses the estimated duration of tremor in hours (T_D, column 3, Table 5.1) to estimate the moment release as (Guilhem and Nadeau, 2012)

$$M_0 = T_D \times 5.2e16. \tag{5.3}$$

The total cumulative duration is 151.2 hours, which translates to a cumulative moment release of 7.2e+18 or 6.5 M_w, which is comparable to the estimate based purely on recurrence interval and constant slip area. The estimated moment (M_0) and moment magnitude (M_w) for each episode are given in columns 4 and 5 of Table 5.1. We note that these magnitude estimates are with regard to the inferred slow-slip driving the activity on the small seismic patches hosting the observed seismic tremor rather than the slip and moment of the seismic patches themselves which can be smaller by several orders of magnitude (Kao et al., 2010). While not dramatically different, the slightly larger estimated cumulative moment release estimated from the tremor duration may result from either 1) a variable tectonic loading rate

($\dot{S} \neq constant$), 2) incomplete stress-drop of the slow-slip events over many cycles which was subsequently released following the 2004 Napa Earthquake, 3) variable slow-slip area, or 4) background activity associated with small inter-ETS events. Rather than assuming both slip and area are constant, we instead assume that the total moment is constrained by the moment-duration scaling (Equation 5.3) and estimate the area and slip of each individual event. We first estimate the slip assuming perfect release of stored tectonic strain over a given cycle (Equation 5.2) and solve for the slow-slip area using the determined values for slip and moment in Equation 5.1 (Model 1), and secondly we estimate the slip of each episode using the total expected moment release assuming constant area. If we constrain the slip (d) using Equation 5.2, and the moment using Equation 5.3, we can relax the assumption of constant area and solve for A in Equation 5.1, the results are given in column 6 of Table 5.1. Instead, if we don't make the assumption that the region releases all stored tectonic strain over a single cycle and assume constant area, using Equations 5.1 and 5.3, we can solve for the inferred slip of each event (d_2), which is given in column 7, of Table 5.1.

We additionally consider fixing the mean stress drop rather than the slip or area, and fix the ratio of slip (d) to the characteristic length scale $A^{1/2}$

$$\Delta\sigma = C\mu \frac{d}{A^{1/2}} \tag{5.4}$$

where C is a geometric constant of order unity, and μ is the material's shear modulus. We estimate an average stress drop of $\sim 9.6kPa$ using the estimated averaged slip of 6.2 mm and a constant area of 375 km. Using Equation 5.1 to express the area in terms of the individual event moments from Equation 5.3 we write an expression for the stress drop from the estimated cumulative slip (Σd, Equation 5.2) and inferred moment (ΣM_0, Equation 5.3)

$$\Delta\sigma = C\left(\frac{\mu\Sigma d}{\Sigma(M_0^{1/3})}\right)^{3/2}. \tag{5.5}$$

Using cumulative values of slip ($\Sigma d = 512.4$ mm, Equation 5.2), and moment $(\Sigma(M_0)^{1/3} = 3.62e7Nm$, Equation 5.3), and assuming $C = 1$ and $\mu = 30$ GPa, we obtain a stress drop of 8.5 kPa which is several orders of magnitude smaller than traditional earthquakes. These calculated stress drops ($\Delta\sigma$) are several of orders of magnitude smaller than those of traditional earthquakes but are of similar magnitude of slow-slip events in other tectonics settings. Using Equation 5.2 to estimate the slip, we can use

The inferred slips and areas can be calculated using the assumption of constant stress drop as

$$d = \left(\frac{\Delta\sigma^2 M_0}{C^2\mu^3}\right)^{1/3} \tag{5.6}$$

$$A = \left(\frac{CM_0}{\Delta\sigma}\right)^{2/3}, \tag{5.7}$$

where the $\Delta\sigma = constant$, and M_0 is given in equation 5.3. The resulting slip and area for each individual episode (d_3, A_3) are given in columns 8 and 9 of Table 5.1.

5.5 Expected Surface Deformation

In order to calculate the expected surface deformation associated with these inferred ETS events we will attempt to improve the spatial and temporal resolution of the inferred slip using the LFE catalog. We consider LFEs to be analagous to repeating earthquakes which are thought to occur on small fault zone asperities with failure being driven by aseismic fault slip on the surrounding fault interface (Nadeau and Johnson, 1998; Uchida and Matsuzawa, 2013). We assume that the slip of the region in Figure 5.3 maintains plate rate over the ~ 15.5 year observation period, and calculate the cumulative slip (S_{total}) in a similar manner as Equation 5.2. We then discretize the slipping patch (black rectangle, Figure 5.3) into 5 patches of 5 km in length. Further, rather than using the recurrence interval and empirical magnitude - slip scaling relationship (Nadeau and Johnson, 1998) to obtain a slip estimate for each family as is done with repeating earthquakes on the SAF, we assume that each occurrence of an LFE within a given family represents a constant amount of slip, and the slip of each LFE is normalized such that the cumulative slip from each family is equal to the plate rate times the observational period. We calculate the surface deformation using a rectangular 3D Okada dislocation for each patch Okada (1985); Thompson (2014). We assign slip to the ith patch by weighting the cumulative slip (S_{total}) by the number of LFEs within a given patch (L_i) and the total number of occurrences for the jth family (N_j). Thus the slip assigned to the ith patch associated with an occurrence of the jth LFE family (s_{ij}) is given as

$$s_{ij} = \frac{S_{Total}}{N_i L_j}. \tag{5.8}$$

Using Equation 5.8, and our discretized fault patches, we can calculate the surface deformation associated with the slow-slip episodes. The resulting raw and detrended timeseries calculated at the location of the LBLSM (Figure 5.2) is shown in Figure 5.12. The total cumulative strain associated with the LFE inferred slow slip over the ~ 15.5 year observation period is on the order of micro-strain (top panel, Figure 5.12). While the total cumulative surface strain is not large due to the depth of the inferred aseismic slip, there are significant rate variations that we may expect to be observable at the surface (lower panel, Figure 5.12). Figure 5.13 shows the strain-rate calculated using a 10 day smoothing window. The mean background strain-rate is $5.e-14$ 1/s, and the mean strain-rate of the peaks associated with the inferred slow-slip events are larger by a factor of ~ 3.5, and the maximum strain-rate of $1.2e-13$ is associated with the episode triggered by the 2014 M6.0 Napa earthquake.

5.6 Observed Surface Deformation

We attempt to directly measure the surface strain associated with the deep aseismic slow-slip hypothesized to accompany the seismically observed NVTs and LFEs using the nearby long-baseline laser strainmeters (LBSLSM, Figure 5.2), and borehole strain meters

(BSM, Figure 5.2). Due to the low strain-rates associated with these events, only the BSM and LBLSM are thought to be capable of measuring the surface geodetic signals associated with these slow-slip events (Figure 5.14). Figure 5.14 shows the detection sensitivity of surface geodetic instruments as a function of period (Agnew and Wyatt, 2003), and the blue rectangle represents the range of possible strain-rates and durations estimated for the inferred slow-slip evnents shown in Figure 5.5. The upper bound on the strain-rate is obtained from the largest inferred slow slip event thought to accompany the 2014 M6.0 Napa Earthquake (Figure 5.13) and corresponds to the slip area inferred from the tremor generating region (black rectangle, Figure 5.2), and the lower bound is obtained from the mean peak rate estimated using the slow slip area corresponding to the LFE region rather than the larger tremor region (red rectangle, Figure 5.3). The solid and dashed black lines represent the detection threshold for the LBLSM and BSM instruments respectively, the regions above the line are geodetically observable, while regions at or below the line will not be reliably measured and are lost within the wander of the instrument.

The resulting modeled deformation signal for the 2014 M6.0 Napa Valley earthquake calculated at the location of the LBLSM in Chalome, CA (Figure 5.2) is shown in Figure 5.15 (red and blue curves). This event represents the largest expected geodetic signal and represents our best chance at detecting an observable surface geodetic signal from an individual event (Figure 5.2). However, the LBLSM which has the highest resolution, shows no response coming close to the order of magnitude of the synthetic signal (grey and purple curves, Figure 5.15).

In order to increase our ability to detect the small surface strain signals associated with these events, we bandpass filter the straindata between 0.5 and 10 days, to remove spurious signals and increase the signal-to-noise ratio of the expected signal we are attempting to observe. Further, we stack the strain signals using the inferred slow-slip origin times and take 30 days before and after the origin time. Figure 5.16 shows the stacked and filtered synthetic strain curves, for which the events add constructively and increase the expected observed amplitudes by a factor of 30, from a median peak amplitude of 0.006 micro-strain, to a peak stack amplitude of 0.2 micro-strain. However, there is no evidence of any geodetic deformation associated with these events, on any of the nearby strainmeters shown in Figure 5.2. Figure 5.17 shows the stacked North-South and East-West strain signals measured at LBLSM instruments CHL1 and CHL2 respectively, with neither component showing any of the expected strain signal.

5.7 Discussion

While there is ample micro-seismic evidence (NVTs and LFEs) to support claims hypothesizing large aseismic slip on the deep extent of the SAF beneath the rupture area of the M8.7 Fort Tejon earthquake, there is no observable geodetic evidence to support this inference. Using empirical scaling relations from subduction zones the inferred aseismic slip inferred from the NVT acitivy should be easily observable on nearby BSMs and LBLSMs

(Figure 5.2). The slip area (black rectangle, Figure 5.3) and total moment release (Equation 5.3) estimated from the observed tremor activity would allow individual slow-slip events to be observed in the recorded surface strain signals. In particular the largest tremor burst associated with the 2014 M6.0 Napa earthquake should be clearly visible, however, we observe no evidence for this deformation in the strain signal (Figure 5.15). Further, if the deformation represents repeated failure of the same fault region, then stacking the signals should increase the amplitude of the signal associated with an individual episode by a factor 30 (Figure 5.16), however, no such signal is observed (Figure 5.17).

While it seems unlikely that these seismic signals are not accompanied by slow-slip, their lack of surface geodetic does warrant some discussion. If the slow-slip area is restricted to the area highlighted by the highly episodic LFE families (red rectangle, Figure 5.3) which are only active during the large bursts of tremor and overall LFE behavior (Figure 5.6), the amplitude and rate of the calculated synthetic strain signals are found to be below the detection threshold of the surface geodetic instruments (Figure 5.14) and are not expected to be reliably recorded. In this view, the episodic LFEs are analogous to repeating earthquakes and act as reliable indicators of quasi-episodic deep aseismic slip, where as the non-episodic LFEs represent variable fault slip which are likely driven by the failure of the larger quasi-periodic slip region. The tremor activity in this view likely represents distinct off-fault behavior which is driven by the aseismic slip occurring on the main SAF structure which accommodates the majority of the differential fault motion between the Pacific and North American plates. This interpretation of the observed seismic signals is consistent with the off-fault locations of the NVT, which have been reported to exhibit distinct behavior on either side of the SAF (Nadeau and Guilhem, 2009). This is also consistent with detail analysis of the LFE catalog which finds that the only the most episodic LFE families provide reasonable slip estimates (Thomas and Shelly, 2017).

5.8 Conclusion

We have used borehole seismometer data from the High Resolution Seismic Network(HSRN) and Tremor Scope Project(TSP) to locate 2865 tremors between 8/21/2001-6/1/2017 on the SAF beneath the rupture area of the M7.8 Ft. Tejon earthquake of 1857 with $\sim$ 300 hours of tremor data having been recorded at 20 Hz frequency. We observe that the tremor rate is not constant but shows quasi-periodic bursts of high activity wherein the burst rates exceed the background rate by $\sim$5 times. We interpret these burst to represent seismic signatures of distinct off-fault behavior, which is driven by deformation origining from slow-slip on the plate interface. We find that the largest burst of tremor observed in our dataset represented a ten-fold increase in the tremor ratein response to the 2014 M6.0 Napa Earthquake, located nearly 350 km to the North. We find additional peaks in tremor rate to also be associated with regional seismicity (distance $<$ 350 km). We additionally examine the temporal behavior of the LFEs located beneath the rupture area of the M7.8 Ft. Tejon earthquake, and find that they exhibit similar quasi-periodic bursts of high activity, with the burst rates exceeding on average 5 times their background rate. We identified 82 quasi-period bursts using cross-correlation (i.e. Guilhem and Nadeau, 2012), which represent periods of increased seismic activity (e.g. LFE and NVT occurrence rates) well above the background rate, and are localized to the slow-slip region. The recurrence intervals of these events range from 30 to 150 day, with individual burst durations ranging from 2 to 10 days. Assuming a fixed slow-slip area (A) of 375 km^2 (Figure 5.3), and constant deep fault slip-rate ($\dot{S}$), the calculated cumulative slip of 512.4 $mm \ \sim 15.5 \ yr \times 33 \ mm/yr$) results in a cumulative moment release or 5.8e+18 or 6.4 M_w, however, this back of the envelope calculation likely over estimates the total moment release of these slow-slip events by a factor of 3 to 5. We estimate the surface deformation associated with these events by discretizing the inferred slow-slip zone into 5 patches and use a rectangular Okada dislocation to estimate the associated surface strain. We use the LFE behavior to roughly estimate the spatio-temporal slip history in a manner commonly used for repeating earthquakes, and find that if the slow-slip area is set by the footprint of tremor that the surface strain should be readily detectable by both the borehole strainmeters and the nearby long-baseline laser strainmeters, however, we do not observe any reliable surface strain signals associated with these bursts, suggesting that they are below the detection threshold. If the slow-slip area were isolated to the region containing highly episodic LFE families we estimate that they would remain undetected. We conclude that while non-volcanic tremor and low-frequency earthquakes are intimately related, these two phenomena represent distinct faulting behaviors, and suggest that the repeating low-frequency events directly record slip on the plate interface, whereas non-volcanic tremor likely represents distinct off-fault behavior which occurs in response to the deformation associated with the quasi-periodic slow-slip events occurring on the fault interface.

5.9 Figures

Figure 5.1: Location of well documented slow slip and shallow creep observed globally (e.g. Beroza and Ide, 2011; Schwartz and Rokosky, 2007; Harris, 2017) . The red rectangles denote the location of quasi-episodic slow slip, and the yellow circles denote location of shallow creeping faults.

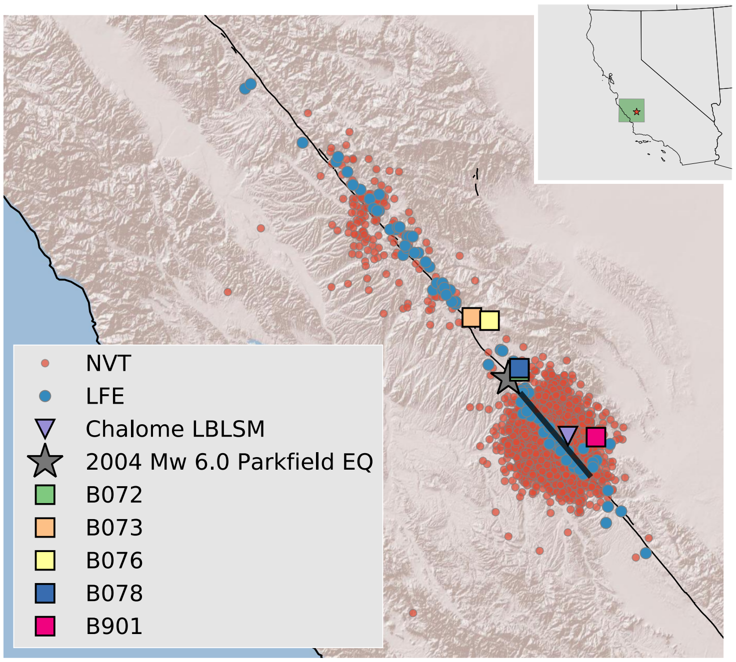

Figure 5.2: Map view view of inferred Parkfield slow-slip region. The red circles denote the location of NVTs and blue circles denote the location of LFEs. The black line represents the surface trace of the inferred slow slip region. The grey star denotes the location of the 2004 Parkfield Earthquake. The triangle symbol denotes the location of the long-baseline laser strainmeters CHL1 and CHL2. The colored rectangles denote the location of PBO borehole strainmeters.

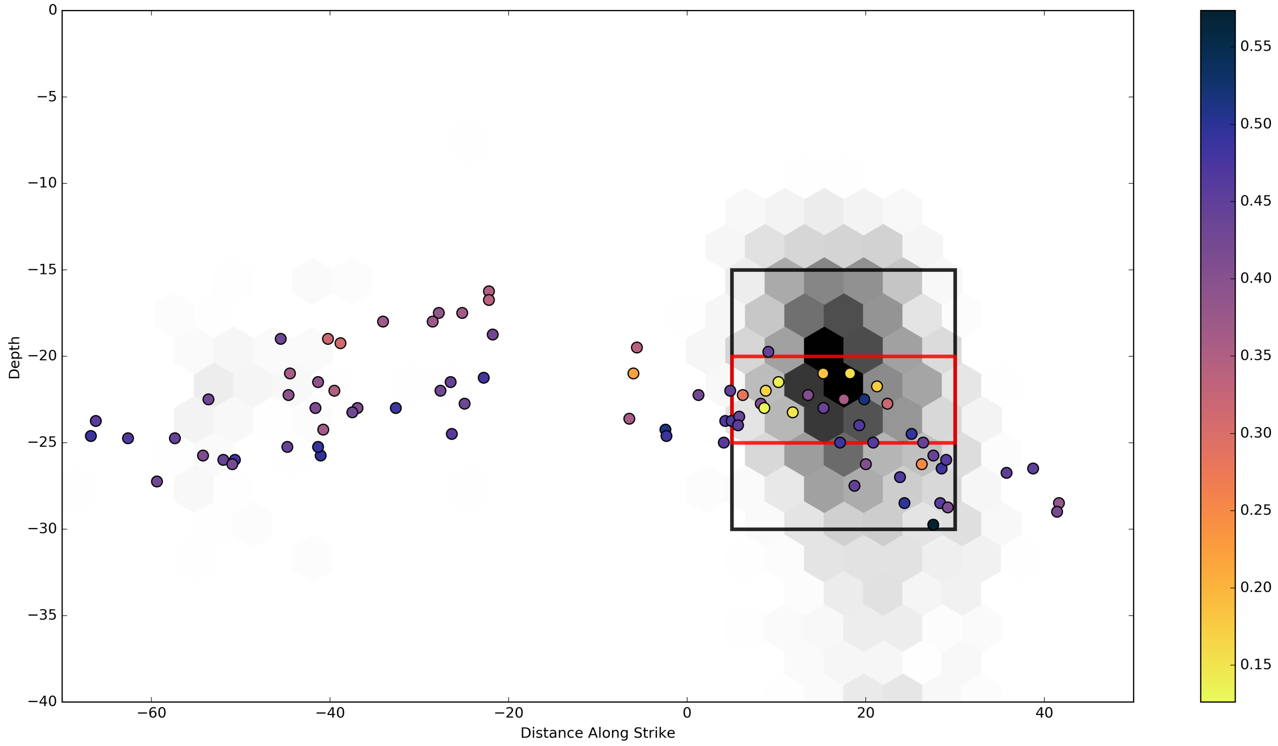

Figure 5.3: Fault transect view of inferred Parkfield slow-slip region. The x-axis denotes distance along strike, with the origin at the location of the 2004 Parkfield Earthquake, and the y-axis denotes depth. The black and red rectangles denote the slip areas (A) in the main text. The grey hexagons represent tremor density with darker regions denoting higher tremor density. The circles represent the location of LFEs, with color denoting episodicity as measured by the minimum fraction of days which contain 75% of the tremor activity. Light colors (e.g. yellow) indicate highly episodic families, where as darker colors (e.g. black) denote more continuous behavior.

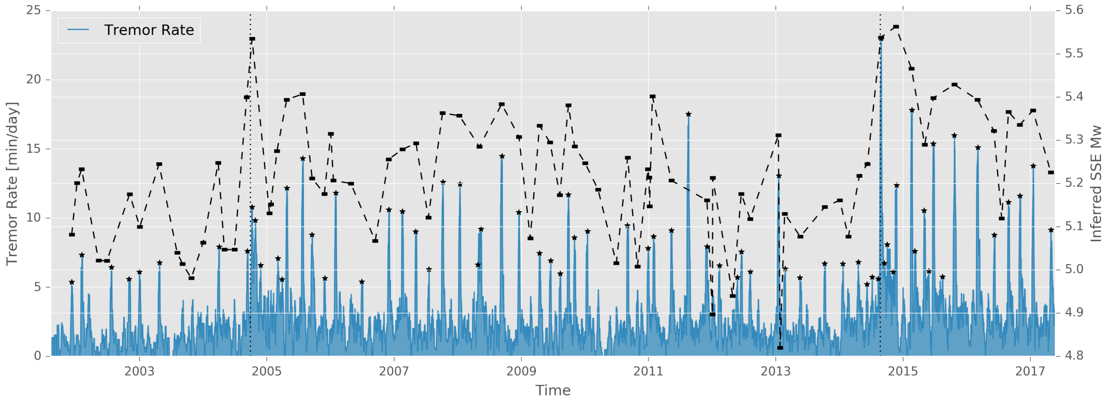

Figure 5.4: Tremor rate, total duration of tremor per day calculated using a 10 day smoothing window, and inferred slow-slip event magnitude timeseries. The blue curve represents a 10-day moving average of the tremor rate [min/day]. The black stars indicate identified peaks. The dashed curve represents the magnitude of the inferred slow-slip events.

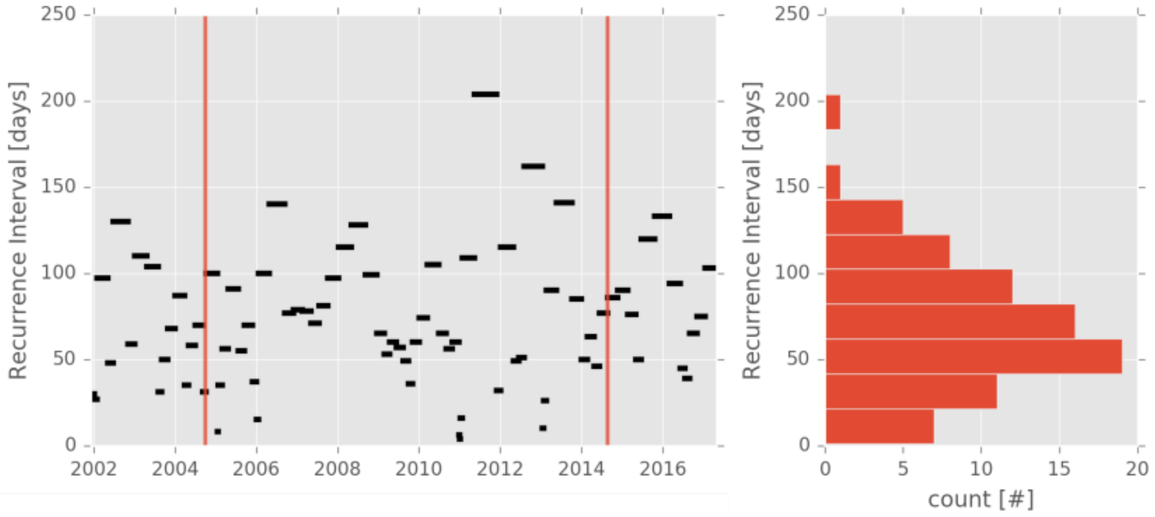

Figure 5.5: Inferred slow-slip recurrence intervals. The recurrence intervals is calculated simply as the number of days since the previous the event. a) The black lines span the time between two consecutive events with the height denoting the number of days between them. The vertical red lines denote the time of the 2004 M_w6.0 Parkfield Eq. and the 2014 M_w6.0 Sputh Napa Eq. b) Histogram of all recurrence intervals.

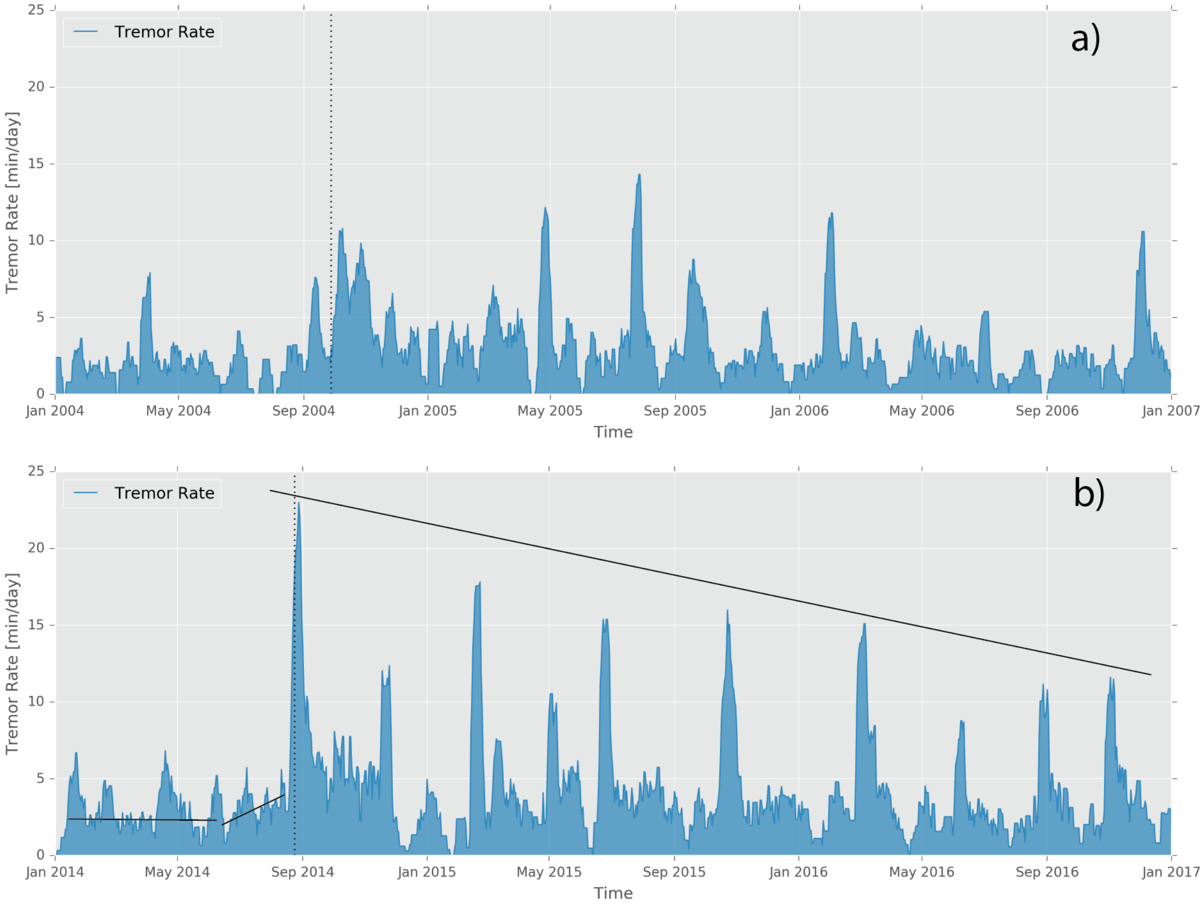

Figure 5.6: Tremor rate response to the 2004 M_w6.0 Parkfield Earthquake(panel a) and 2014 M_w6.0 South Napa Earthquake(panel b). The blue curve denotes the tremor rate calculated using a 10-day moving window. The black vertical dotted lines denote the time of the Parkfield and South Napa Earthquakes, Sept. 28, 2004 and Aug. 24, 2014 respectively. The long black line in panel b represents a slope of -0.04.

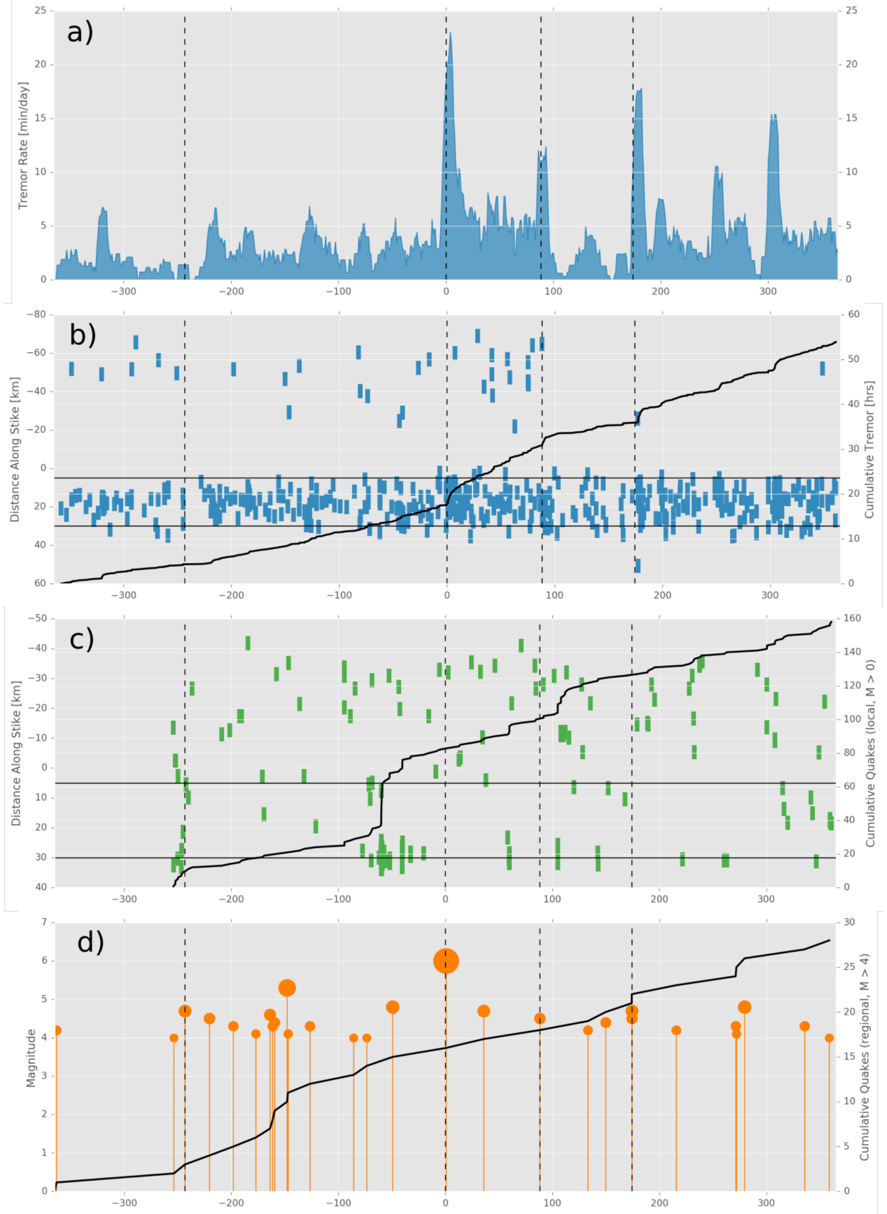

Figure 5.7: Local and regional seismicity one year before and after the 2014 M_w6.0 South Napa Earthquake. In all panels the vertical dashed lines represent the times large regional earthquakes with interesting tremor responses. The black curve denotes the cumulative curves for all panels present. a) Blue curve represents the rate of tremor in the inferred slow slip region. b) The blue bars represent the location of tremor along strike as a function of time. c) The green bars denote the location of local seismicity ($M_w > 0$). d) The orange circles represent the magnitude and timing of large regional earthquakes ($M_w \geq 4.0$, distance ≤ 350 km.)

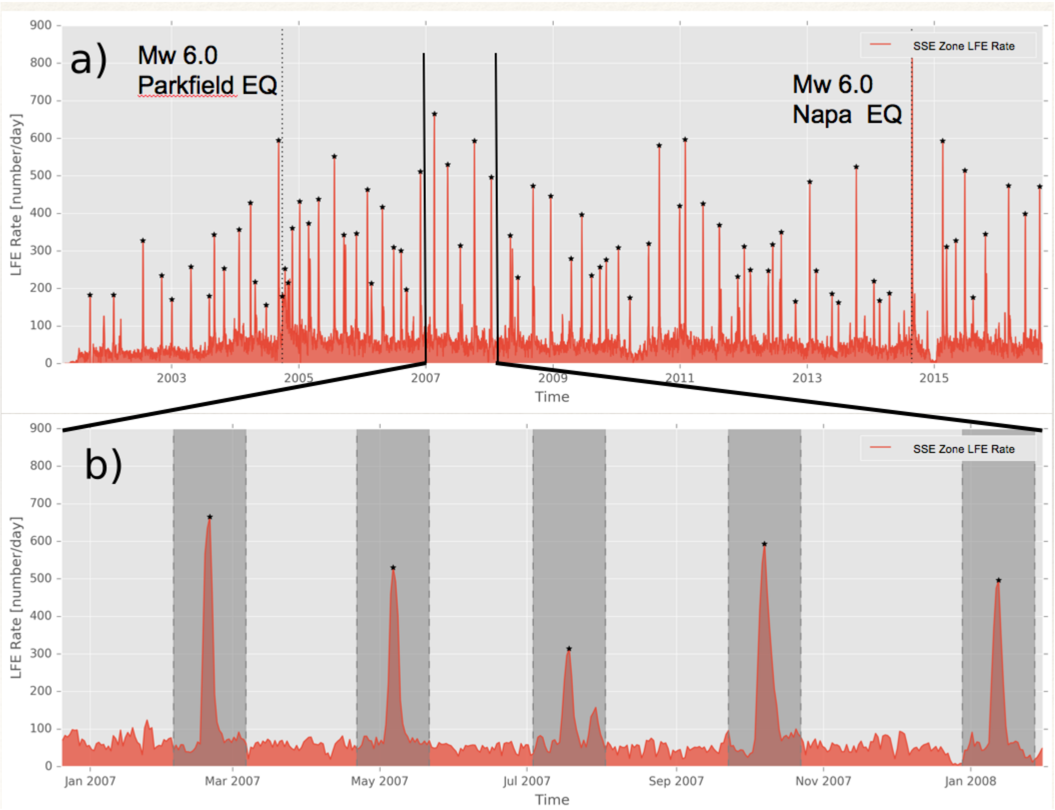

Figure 5.8: LFE occurrence rate timeseries. a) The red curve indicates the rate of LFE occurrence per day calculatedly using a 10-day moving window for all LFEs located within the slow-slip region in Figure 5.3. The black stars represent identified LFE rate peaks. The vertical lines represent the time of the Parkfield and South Napa Earthquakes respectively. b) Zoomed inset of above for 2007. The dark grey regions denote the 10-day window used to define slow-slip bursts.

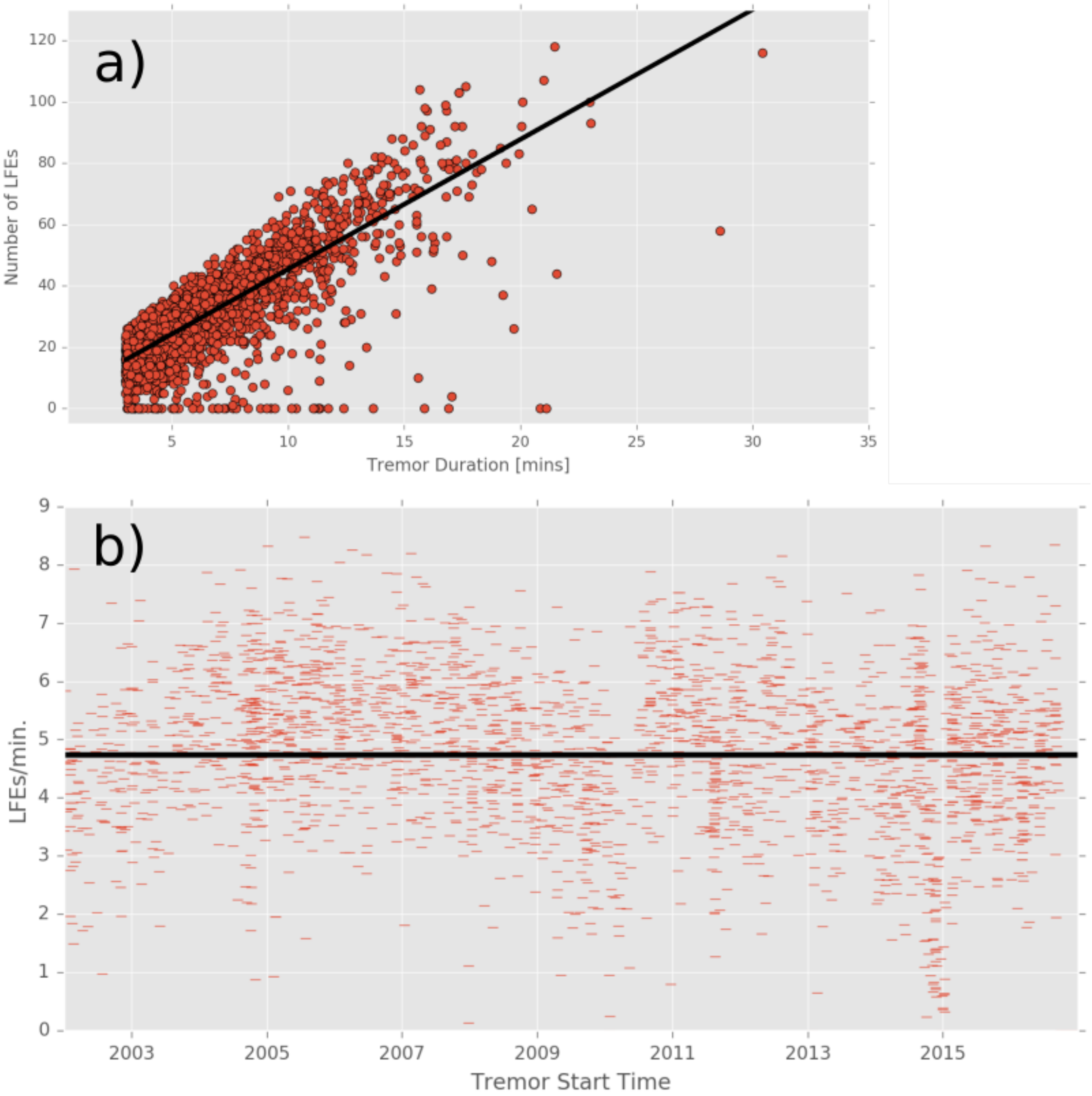

Figure 5.9: LFE and Tremor temporal overlap. a) The red circles indicate the number of LFEs contained within a given tremor burst as a function tremor burst duration. The black line represents a linear regression, with a slope of 4.2 LFEs per minute((note we have ignores all points which contain no LFEs). b) LFE count per tremor burst normalized by tremor burst duration. The black line represents the mean value of 4.7 LFEs per minute.

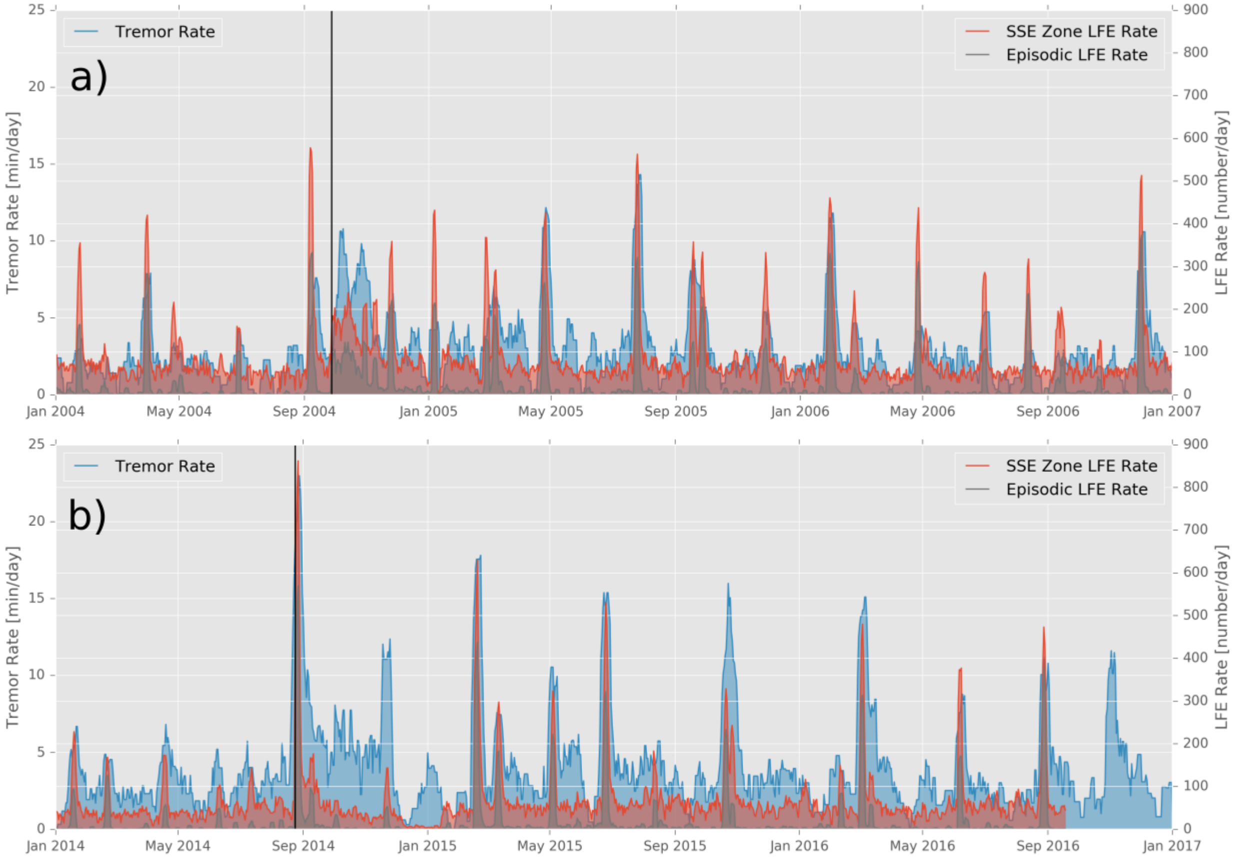

Figure 5.10: Comparison of LFE and tremor rates around the times of the 2004 M_w6.0 Parkfield Earthquake(panel a) and 2014 M_w6.0 South Napa Earthquake(panel b). The blue, red, and grey curves indicates the rate calculated using a 10-day moving window for tremor, slow-slip LFEs (families located with the slow-slip region in Figre 5.3), and episodic LFEs (subset of slow-slip LFEs with MFD75 values below 0.25). The black vertical lines denote the time of the Parkfield and South Napa Earthquakes, Sept. 28, 2004 and Aug. 24, 2014 respectively.

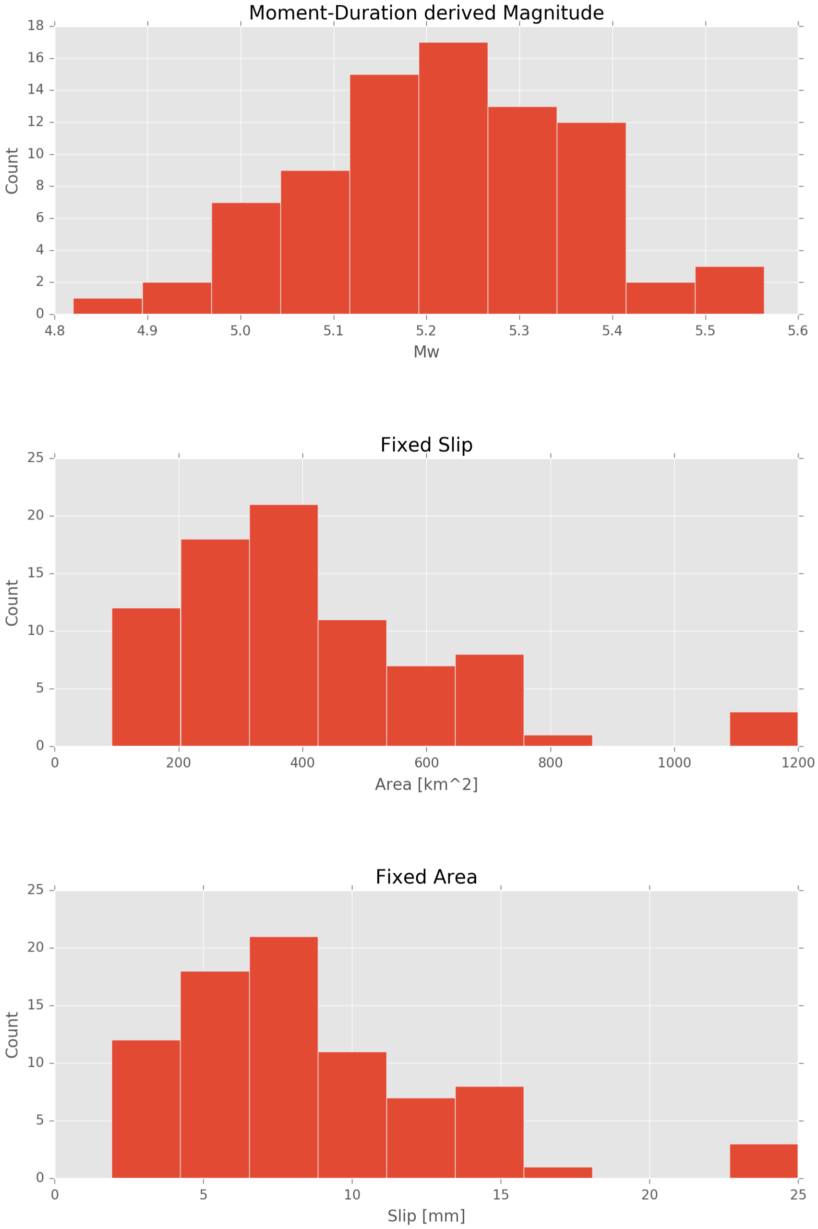

Figure 5.11: Tremor inferred slow-slip episode characteristics. a) Histogram of event magnitudes derived from the duration of tremor and Equation 5.3. b) Histogram of possible areas computed using the moment calculated from Equation 5.1, where M_0 is calculated from Equation 5.3, and d is calculated from Equation 5.2. c) Histogram of slip values calculated from Equation 5.1 assuming $A = 375\ km^2$, and M_0 is calculated from Equation 5.3.

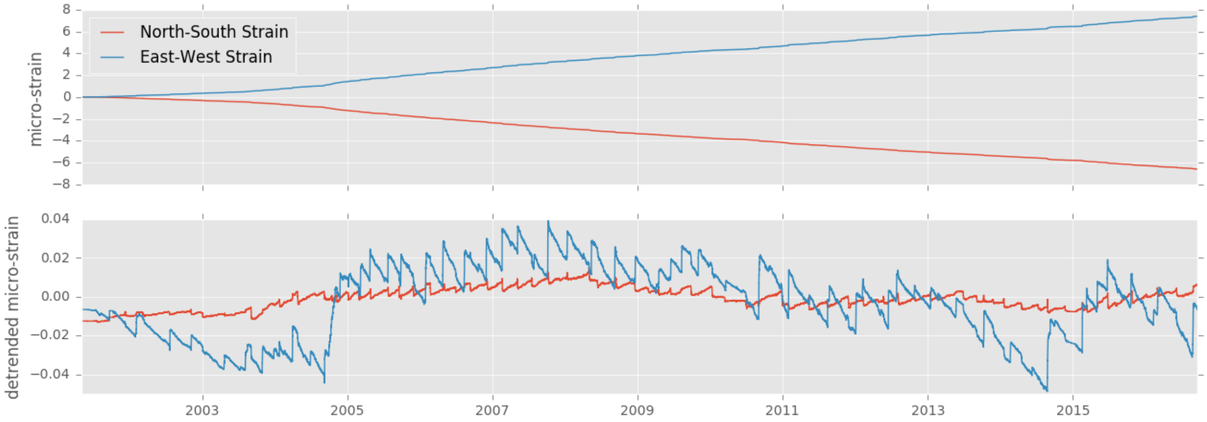

Figure 5.12: Modeled surface strain calculated using 5 rectangular Okada dislocations with slip assigned to each LFE occurrence using equation 5.8. The blue and red curves represent the surface strain in East-West and North-South direction respectively. The top panel shows the raw strain timeseries, and the lower panel shows the detrended timseries.

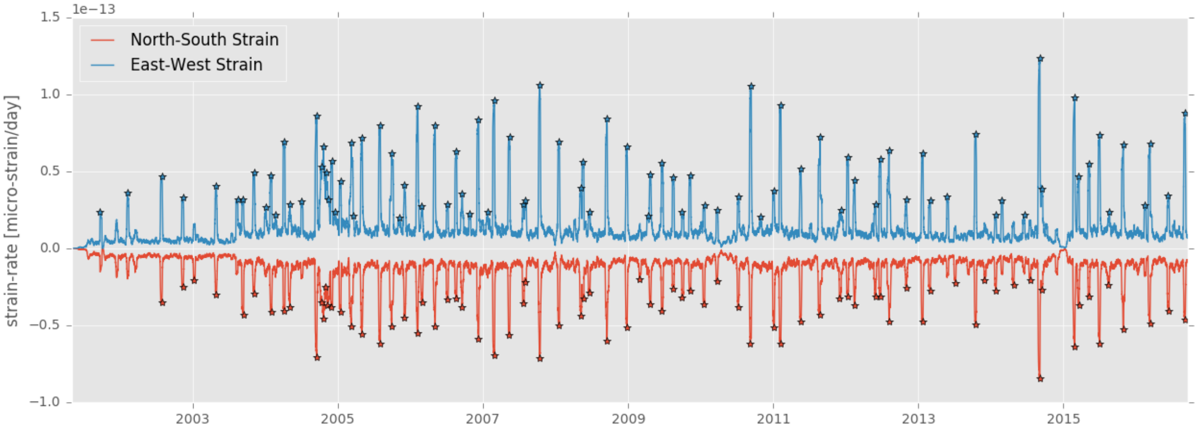

Figure 5.13: Modeled surface strain-rate calculated from the synthetic surface strain shown in Figure 5.12 and calculated using a 10 day smoothing window. The stars represent identified peaks used to estimate episode strain-rates. The stars represent identified peaks associated with the inferred slow-slip events.

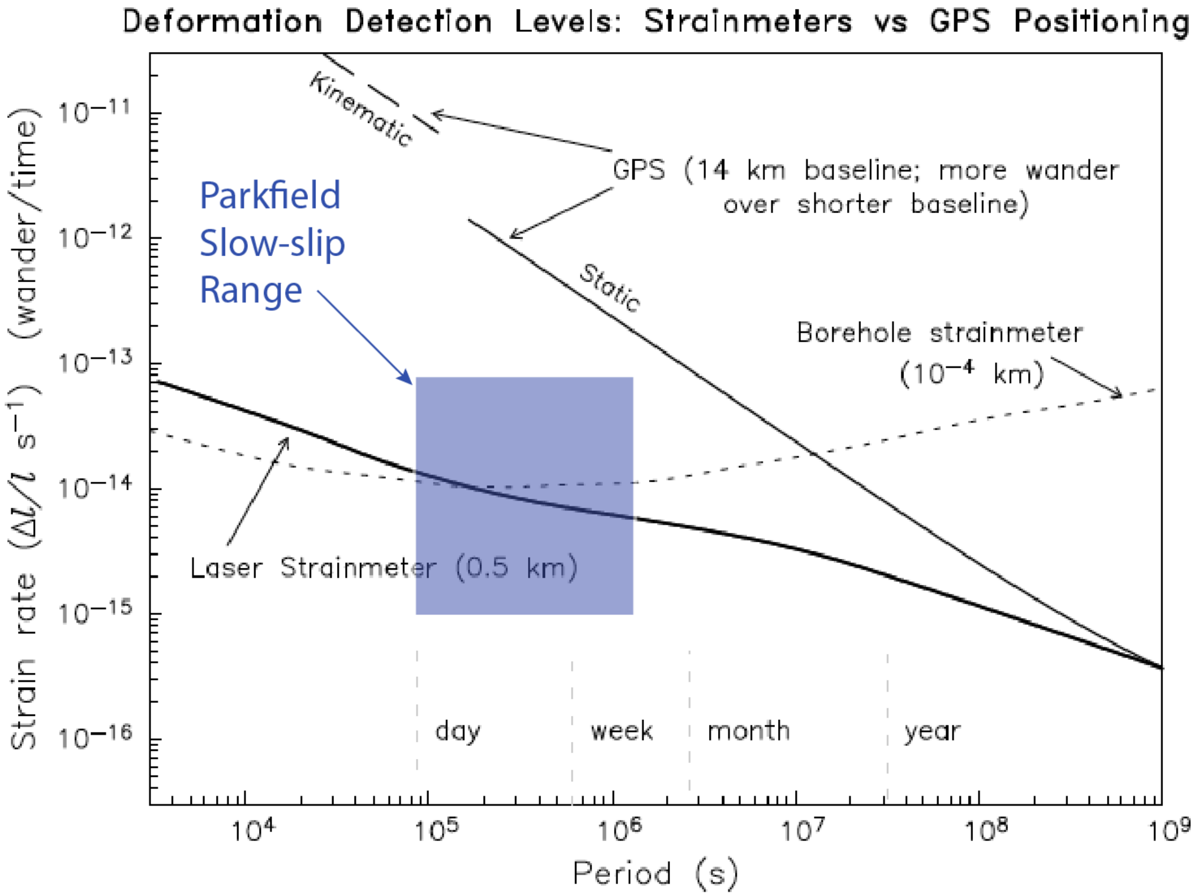

Figure 5.14: Detection/wander threshold as a function of period adapted from Agnew and Wyatt (2003). The blue rectangle represents the range of expected surface strain estimated in section 5.5 from NVT and LFE observations.

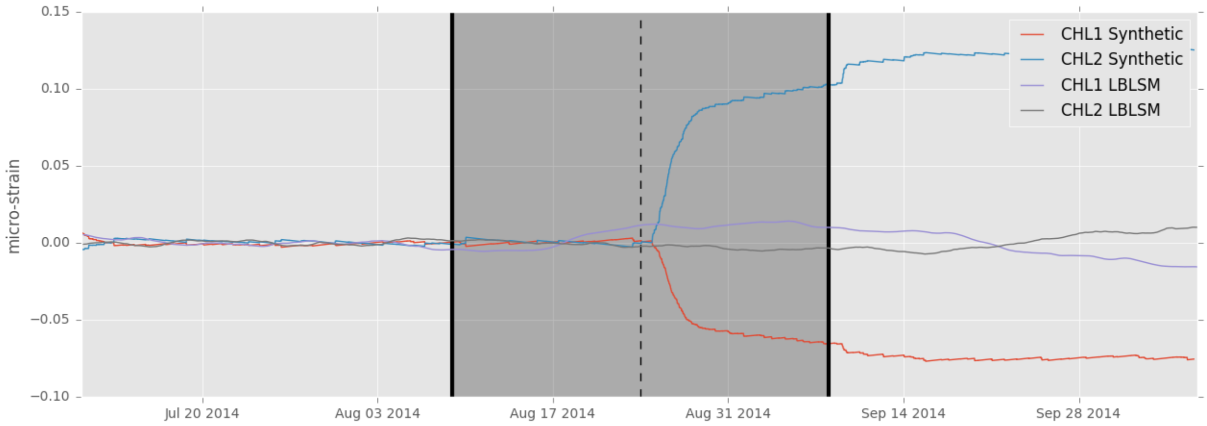

Figure 5.15: Observed and Modeled surface strain from the inferred ETS associated with the 2014 M_w6.0 South Napa Earthquake at the location of the Chalome LBLSM (Figure 5.2), and the black and purple lines are the corresponding observations. The blue and red curves represents the computed East-West and North-South strain respectively. Note that we have fit a linear trend to the signal prior to the mainshock and removed if from the entire series. The vertical dashed line denotes the time of the mainshock. The dark grey region denotes ten days on either side of the mainshock.

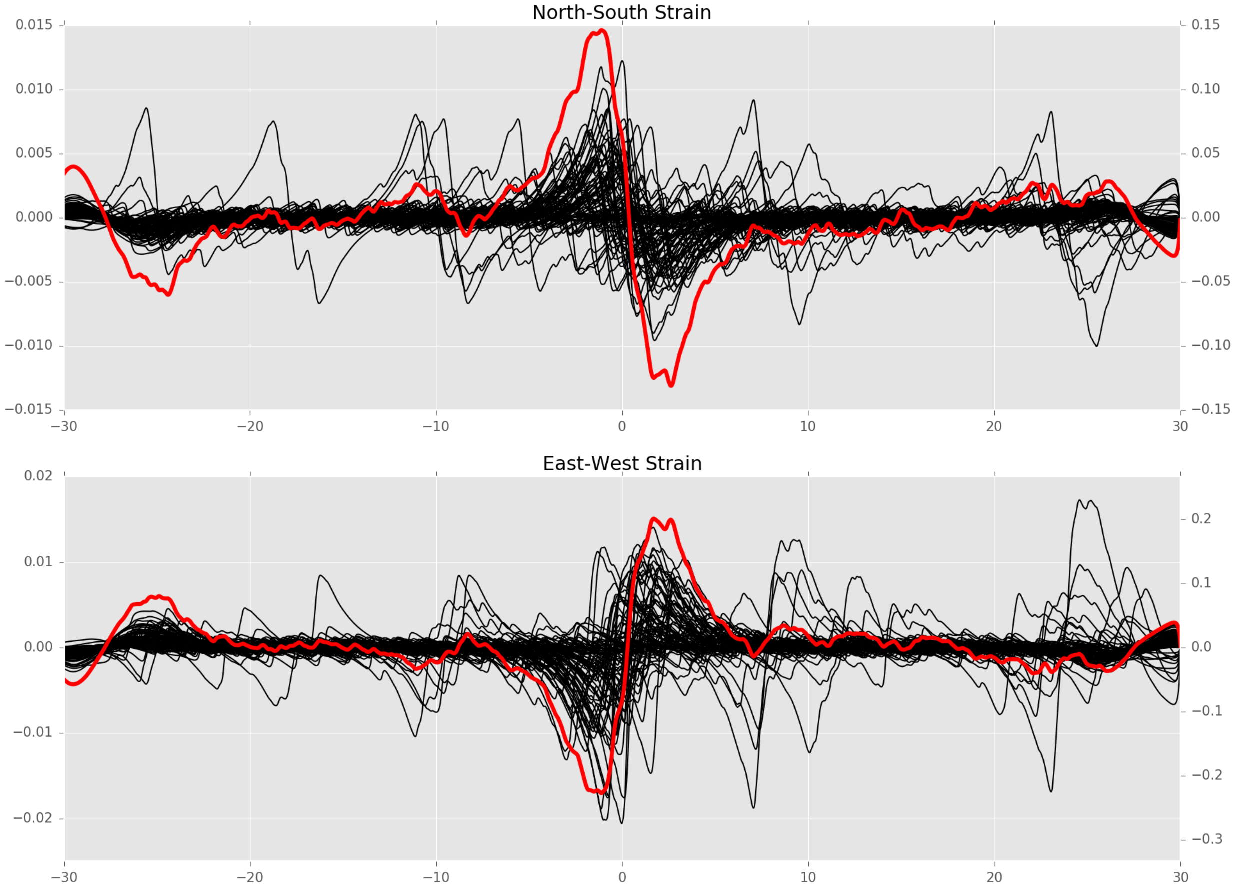

Figure 5.16: Stacked synthetic strain signals for all 82 inferred slow-slip events at the location of the LBLSM (Figure 5.2). The black curves represent the individual episode strain curves and correspond to the left y-axis[micro-strain], and the red curves represent the stacked strain curves and correspond to the right y-axis[micro-strain]. The upper and lower panels corresponds to the calculated strain in the North-south and East-West directions respectively.

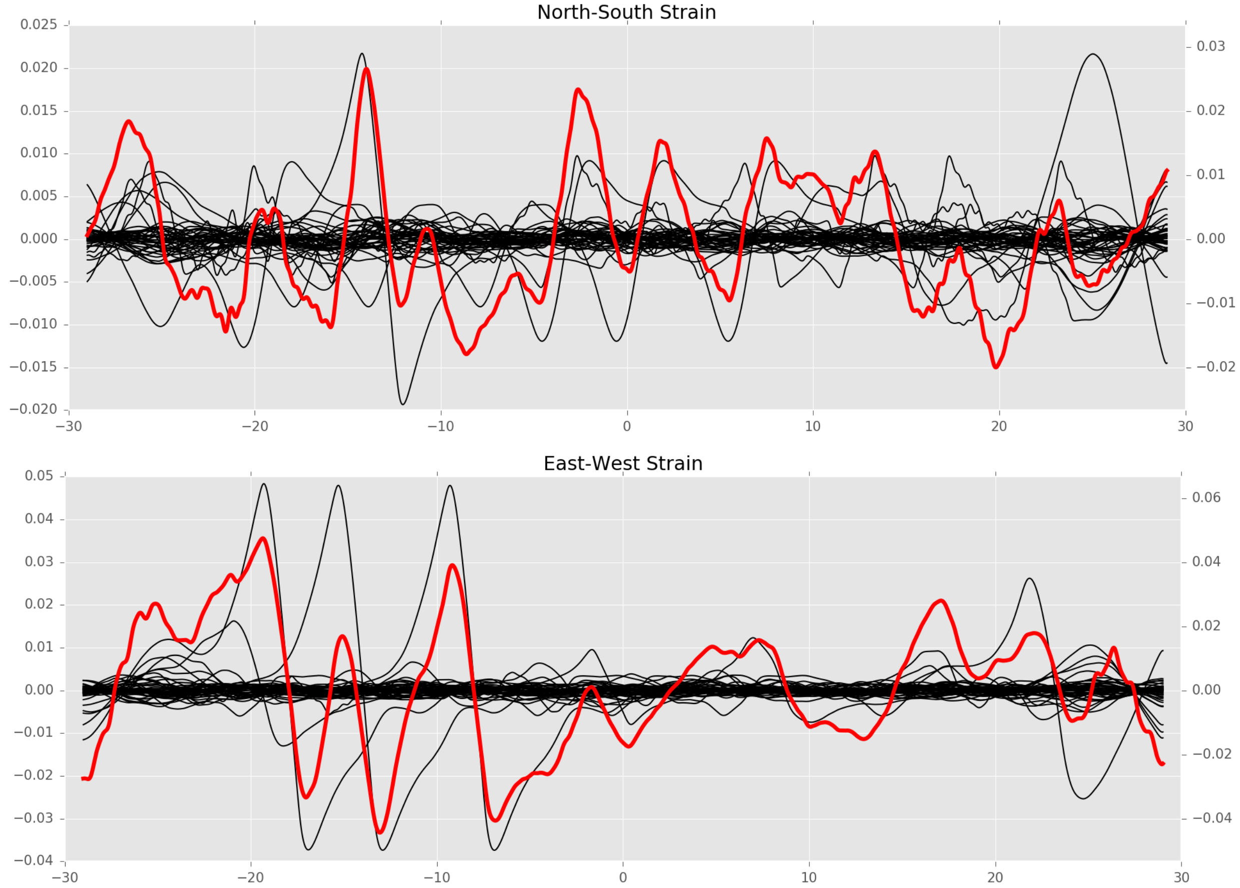

Figure 5.17: Stacked strain signals for all 82 inferred slow-slip events observed at the Chalome LBLSM (Figure 5.2). The black curves represent the individual episode strain curves and correspond to the left y-axis, and the red curves represent the stacked strain curves and correspond to the right y-axis. The upper and lower panels corresponds to the calculated strain in the North-sout (CHL1) and East-West (CHL2) directions respectively.

5.10 Tables

Date	$T_R(day)$	$T_D(min)$	$M_0(Nm)$	M_w	$A_1(km^2)$	$d_2(mm)$	$d_3(mm)$	$A_3(km^2)$
2001-12-08	49.2	61.7	5.346468e+16	5.082	228.07	4.75	6.73	264.75
2002-01-07	36.7	93.2	8.073000e+16	5.201	344.37	7.18	7.72	348.46
2002-02-03	56.9	104.0	9.010732e+16	5.233	384.37	8.01	8.01	374.95
2002-05-11	61.0	50.2	4.349800e+16	5.022	185.55	3.87	6.28	230.73
2002-06-28	47.0	50.0	4.330732e+16	5.021	184.74	3.85	6.27	230.06
2002-11-05	130.3	85.0	7.364068e+16	5.175	314.13	6.55	7.49	327.75
2003-01-03	58.8	65.7	5.694868e+16	5.100	242.93	5.06	6.87	276.13
2003-04-23	110.0	108.2	9.376468e+16	5.245	399.97	8.33	8.12	385.02
2003-08-05	104.7	53.4	4.623668e+16	5.040	197.23	4.11	6.41	240.32
2003-09-05	30.3	48.8	4.232800e+16	5.014	180.56	3.76	6.23	226.58
2003-10-25	50.0	43.5	3.768268e+16	4.981	160.74	3.35	5.99	209.68
2004-01-01	69.1	57.8	5.005868e+16	5.063	213.54	4.45	6.59	253.39
2004-03-28	86.2	109.3	9.477000e+16	5.248	404.26	8.42	8.15	387.77
2004-05-02	35.5	54.6	4.736332e+16	5.047	202.04	4.21	6.46	244.21
2004-06-29	57.8	54.7	4.742400e+16	5.047	202.30	4.22	6.47	244.41
2004-09-07	69.5	184.9	1.602727e+17	5.400	683.68	14.25	9.71	550.43
2004-10-08	31.3	294.9	2.555540e+17	5.535	1090.12	22.72	11.34	751.25
2005-01-16	45.1	73.2	6.340532e+16	5.131	270.47	5.64	7.13	296.63
2005-01-24	108.0	78.6	6.815468e+16	5.152	290.73	6.06	7.30	311.26
2005-02-28	34.8	120.3	1.042253e+17	5.275	444.60	9.26	8.41	413.15
2005-04-25	55.7	180.9	1.568147e+17	5.394	668.93	13.94	9.64	542.48
2005-07-25	46.0	189.2	1.640080e+17	5.407	699.61	14.58	9.78	558.95
2005-09-18	55.1	96.7	8.378068e+16	5.212	357.39	7.45	7.82	357.18
2005-11-27	70.2	85.4	7.403068e+16	5.176	315.79	6.58	7.50	328.90
2006-01-03	63.5	137.9	1.194960e+17	5.315	509.74	10.62	8.80	452.58
2006-01-18	62.1	94.8	8.219468e+16	5.207	350.62	7.31	7.77	352.66
2006-04-28	88.5	92.7	8.036600e+16	5.200	342.82	7.14	7.71	347.41
2006-09-15	78.0	58.6	5.080400e+16	5.067	216.72	4.52	6.62	255.89
2006-12-01	76.4	112.5	9.746532e+16	5.256	415.76	8.66	8.22	395.09
2007-02-18	79.2	122.0	1.056987e+17	5.279	450.88	9.40	8.45	417.04
2007-05-07	77.8	127.7	1.106560e+17	5.293	472.03	9.84	8.58	429.98
2007-07-17	71.2	70.7	6.123868e+16	5.121	261.23	5.44	7.04	289.83
2007-10-06	81.1	162.7	1.409893e+17	5.363	601.42	12.53	9.30	505.34
2008-01-11	97.0	159.4	1.381467e+17	5.357	589.30	12.28	9.24	498.53
2008-05-05	116.0	124.6	1.079520e+17	5.285	460.49	9.60	8.51	422.94
2008-09-10	127.0	175.1	1.517187e+17	5.384	647.19	13.49	9.53	530.67
2008-12-18	99.1	134.8	1.168007e+17	5.308	498.24	10.38	8.73	445.75
2009-02-21	65.1	59.8	5.183532e+16	5.073	221.12	4.61	6.66	259.35
2009-04-15	52.9	147.1	1.275213e+17	5.334	543.97	11.34	8.99	472.63

2009-06-14	60.1	128.6	1.114707e+17	5.295	475.50	9.91	8.60	432.09
2009-08-10	56.8	84.5	7.326800e+16	5.173	312.54	6.51	7.48	326.64
2009-09-28	49.2	173.1	1.500373e+17	5.381	640.02	13.34	9.49	526.74
2009-11-03	35.9	125.0	1.083160e+17	5.286	462.05	9.63	8.52	423.89
2010-01-02	78.9	109.0	9.451000e+16	5.247	403.15	8.40	8.14	387.06
2010-03-17	55.9	88.5	7.667400e+16	5.186	327.07	6.82	7.59	336.69
2010-06-30	105.1	49.0	4.251000e+16	5.016	181.34	3.78	6.24	227.23
2010-09-03	64.1	114.3	9.902532e+16	5.260	422.41	8.80	8.27	399.29
2010-10-29	56.9	47.8	4.141800e+16	5.008	176.68	3.68	6.18	223.32
2010-12-28	59.6	103.8	8.997732e+16	5.233	383.82	8.00	8.01	374.59
2011-01-03	32.6	97.2	8.420532e+16	5.214	359.20	7.48	7.83	358.39
2011-01-07	40.1	77.1	6.685468e+16	5.147	285.18	5.94	7.25	307.29
2011-01-23	97.9	186.1	1.613040e+17	5.402	688.08	14.34	9.73	552.79
2011-05-12	62.3	94.9	8.228132e+16	5.207	350.99	7.31	7.77	352.91
2011-12-02	106.3	80.9	7.013932e+16	5.161	299.19	6.23	7.37	317.28
2012-01-03	80.5	32.6	2.826200e+16	4.897	120.56	2.51	5.44	173.09
2012-01-04	68.3	97.0	8.403200e+16	5.213	358.46	7.47	7.83	357.90
2012-04-28	79.2	37.8	3.273400e+16	4.940	139.63	2.91	5.72	190.90
2012-06-16	48.5	85.3	7.390932e+16	5.176	315.28	6.57	7.50	328.55
2012-08-06	51.0	69.8	6.048468e+16	5.118	258.01	5.38	7.01	287.45
2013-01-15	80.8	136.4	1.182480e+17	5.312	504.41	10.51	8.77	449.43
2013-01-25	109.0	25.0	2.163200e+16	4.820	92.28	1.92	4.98	144.83
2013-02-20	36.3	72.7	6.299800e+16	5.130	268.73	5.60	7.11	295.36
2013-05-21	90.7	60.6	5.248532e+16	5.077	223.89	4.67	6.69	261.51
2013-10-09	31.2	76.8	6.656868e+16	5.146	283.96	5.92	7.24	306.41
2014-01-02	103.0	81.1	7.030400e+16	5.161	299.90	6.25	7.37	317.77
2014-02-21	32.0	60.6	5.249400e+16	5.077	223.92	4.67	6.69	261.54
2014-04-25	62.9	98.7	8.554000e+16	5.218	364.89	7.60	7.87	362.17
2014-06-10	46.6	108.1	9.371268e+16	5.245	399.75	8.33	8.12	384.88
2014-08-26	76.3	297.6	2.579373e+17	5.538	1100.29	22.93	11.37	755.91
2014-11-20	86.1	324.5	2.812160e+17	5.563	1199.59	25.00	11.71	800.74
2015-02-18	89.9	232.2	2.012747e+17	5.466	858.58	17.89	10.47	640.70
2015-05-05	76.2	126.6	1.097460e+17	5.290	468.15	9.76	8.55	427.62
2015-06-24	49.8	183.5	1.590073e+17	5.398	678.28	14.13	9.68	547.53
2015-10-22	120.5	204.6	1.772767e+17	5.429	756.21	15.76	10.04	588.70
2016-03-03	132.3	181.4	1.572307e+17	5.394	670.70	13.98	9.64	543.44
2016-06-05	94.6	141.5	1.226507e+17	5.322	523.19	10.90	8.88	460.51
2016-07-20	45.0	70.2	6.082268e+16	5.119	259.45	5.41	7.03	288.52
2016-08-28	38.2	164.7	1.427487e+17	5.366	608.93	12.69	9.34	509.54
2016-11-01	64.6	148.2	1.283967e+17	5.336	547.70	11.41	9.01	474.79
2017-01-15	75.1	166.4	1.441787e+17	5.369	615.03	12.82	9.37	512.94

2017-04-28	102.8	101.5	8.794932e+16	5.226	375.17	7.82	7.95	368.94

Bibliography

Agnew, D. C., Wyatt, F. K., 2003. Long-base laser strainmeters: a review. SIO Technical Report 2.

Aguiar, A. C., Melbourne, T. I., Scrivner, C. W., 2009. Moment release rate of cascadia tremor constrained by gps. Journal of Geophysical Research: Solid Earth 114 (B7).

Ancey, C., 2007. Plasticity and geophysical flows: a review. Journal of Non-Newtonian Fluid Mechanics 142 (1), 4–35.

Aryal, A., Brooks, B. A., Reid, M. E., 2015. Landslide subsurface slip geometry inferred from 3-d surface displacement fields. Geophysical Research Letters 42 (5), 1411–1417.

Balmforth, N., Craster, R., 1999. A consistent thin-layer theory for bingham plastics. Journal of non-newtonian fluid mechanics 84 (1), 65–81.

Balmforth, N., Craster, R., Sassi, R., 2002. Shallow viscoplastic flow on an inclined plane. Journal of Fluid Mechanics 470, 1–29.

Baum, R., Reid, M., 2000. Ground water isolation by low-permeability clays in landslide shear zones. Landslides in research, theory and practice. Thomas Telford, London, 139–144.

Baum, R., Savage, W., Wasowski, J., 2003. Mechanics of earth flows. In: Proceedings of the International Conference FLOWS, Sorrento, Italy.

Beeler, N., Hirth, G., Thomas, A., Bürgmann, R., 2016. Effective stress, friction, and deep crustal faulting. Journal of Geophysical Research: Solid Earth 121 (2), 1040–1059.

Beroza, G. C., Ide, S., 2011. Slow earthquakes and nonvolcanic tremor. Annual review of Earth and planetary sciences 39, 271–296.

Booth, A. M., Lamb, M. P., Avouac, J.-P., Delacourt, C., 2013a. Landslide velocity, thickness, and rheology from remote sensing: La clapière landslide, france. Geophysical Research Letters 40 (16), 4299–4304.

Booth, A. M., Roering, J. J., 2011. A 1-d mechanistic model for the evolution of earthflow-prone hillslopes. Journal of Geophysical Research: Earth Surface (2003–2012) 116 (F4).

Booth, A. M., Roering, J. J., Rempel, A. W., 2013b. Topographic signatures and a general transport law for deep-seated landslides in a landscape evolution model. Journal of Geophysical Research: Earth Surface 118 (2), 603–624.

Bouchon, M., Marsan, D., Durand, V., Campillo, M., Perfettini, H., Madariaga, R., Gardonio, B., 2016. Potential slab deformation and plunge prior to the tohoku, iquique and maule earthquakes. Nature Geoscience 9 (5), 380–383.

Buckley, S., Rossen, P., Persaud, P., 2000. Roi_pac documentation-repeat orbit interferometry package. JET Propulsion Lab., Pasadena, CA.

Bürgmann, R., Rosen, P. A., Fielding, E. J., 2000. Synthetic aperture radar interferometry to measure earth's surface topography and its deformation. Annual Review of Earth and Planetary Sciences 28 (1), 169–209.

Chleborad, A., Diehl, S., Cannon, S., 1996. Geotechnical properties of selected materials from the slumgullion landslide. The Slumgullion earth flow: a large-scale natural laboratory. US Geological Survey Bulletin 2130, 67–71.

Chleborad, A. F., 1980. Investigations of a natural slope failure in weathered tertiary deposits western powder river basin, wyoming. Open-file report, US Department of the Interior, US Geological Survey.

Coe, J. A., 2012. Regional moisture balance control of landslide motion: Implications for landslide forecasting in a changing climate. Geology 40 (4), 323–326.

Coe, J. A., Ellis, W. L., Godt, J. W., Savage, W. Z., Savage, J. E., Michael, J., Kibler, J. D., Powers, P. S., Lidke, D. J., Debray, S., 2003. Seasonal movement of the slumgullion landslide determined from global positioning system surveys and field instrumentation, july 1998–march 2002. Engineering Geology 68 (1), 67–101.

Coe, J. A., McKenna, J. P., Godt, J. W., Baum, R. L., 2009. Basal-topographic control of stationary ponds on a continuously moving landslide. Earth Surface Processes and Landforms 34 (2), 264–279.

Coussot, P., Proust, S., 1996. Slow, unconfined spreading of a mudflow. Journal of Geophysical Research: Solid Earth 101 (B11), 25217–25229.

Coussot, P., Proust, S., Ancey, C., 1996. Rheological interpretation of deposits of yield stress fluids. Journal of Non-Newtonian Fluid Mechanics 66 (1), 55–70.

Crandell, D., Varnes, D., 1960a. Slumgullion earthflow and earthslide near lake city. Geological Society of America Bulletin 71 (12), 1846.

Crandell, D. R., Varnes, D. J., 1960b. Movement of the slumgullion earth flow near lake city, colorado. U.S. Geological Survey Professional Paper 424-B, US Department of the Interior, US Geological Survey.

Crozier, M., 2010. Deciphering the effect of climate change on landslide activity: A review. Geomorphology 124 (3), 260–267.

Crozier, M. J., 1986. Landslides: causes, consequences and environment. Croom Helm London etc.

Cruden, D. M., Varnes, D. J., 1996. Landslides: Investigation and mitigation. chapter 3-landslide types and processes. Transportation research board special report.

Delbridge, B. G., Bürgmann, R., Fielding, E., Hensley, S., 2015. Kinematics of the slumgullion landslide from uavsar interferograms. In: Geoscience and Remote Sensing Symposium (IGARSS), 2015 IEEE International. IEEE.

Diehl, S., Schuster, R., 1996. Preliminary geologic map and alteration mineralogy of the main scarp of the slumgullion landslide. The Slumgullion earth flow: a large-scale natural laboratory. US Geological Survey Bulletin 2130, 13–19.

Dmowska, R., Rice, J. R., Lovison, L. C., Josell, D., 1988. Stress transfer and seismic phenomena in coupled subduction zones during the earthquake cycle. Journal of Geophysical Research: Solid Earth 93 (B7), 7869–7884.

Fan, W., Shearer, P. M., 2016. Local near instantaneously dynamically triggered aftershocks of large earthquakes. Science 353 (6304), 1133–1136.

Farinotti, D., Huss, M., Bauder, A., Funk, M., Truffer, M., 2009. A method to estimate the ice volume and ice-thickness distribution of alpine glaciers. Journal of Glaciology 55 (191), 422–430.

Fleming, R., Baum, R., Giardino, M., 1999. Map and description of the active part of the slumgullion landslide, hinsdale county, colorado. Open-file report, US Department of the Interior, US Geological Survey.

Goldstein, R. M., Zebker, H. A., Werner, C. L., 1988. Satellite radar interferometry: Two-dimensional phase unwrapping. Radio science 23 (4), 713–720.

Gomberg, J., Bodin, P., Savage, W., Jackson, M. E., 1995. Landslide faults and tectonic faults, analogs?: The slumgullion earthflow, colorado. Geology 23 (1), 41–44.

Gould, J. P., 1960. A study of shear failure in certain tertiary marine sediments. In: Research Conference on Shear Strength of Cohesive Soils. ASCE, pp. 615–641.

Guilhem, A., Nadeau, R. M., 2012. Episodic tremors and deep slow-slip events in central california. Earth and Planetary Science Letters 357, 1–10.

Handwerger, A. L., Roering, J. J., Schmidt, D. A., 2013. Controls on the seasonal deformation of slow-moving landslides. Earth and Planetary Science Letters 377, 239–247.

Hanks, T. C., Kanamori, H., 1979. A moment magnitude scale. J. Geophys. Res. Lett. 84, 2348âĂŞ2350.

Harris, R. A., 2017. Large earthquakes and creeping faults. Reviews of Geophysics 55 (1), 169–198, 2016RG000539.
URL http://dx.doi.org/10.1002/2016RG000539

Hensley, S., Michel, T., Simard, M., Jones, C., Muellerschoen, R., Le, C., Zebker, H., Chapman, B., et al., 2009a. Residual motion estimation for uavsar: Implications of an electronically scanned array. In: Radar Conference, 2009 IEEE. IEEE, pp. 1–5.

Hensley, S., Zebker, H., Jones, C., Michel, T., Muellerschoen, R., Chapman, B., 2009b. First deformation results using the nasa/jpl uavsar instrument. In: Synthetic Aperture Radar, 2009. APSAR 2009. 2nd Asian-Pacific Conference on. IEEE, pp. 1051–1055.

Hirose, H., Obara, K., 2006. Short-term slow slip and correlated tremor episodes in the tokai region, central japan. Geophysical Research Letters 33 (17).

Hogg, A., Matson, G., 2009. Slumps of viscoplastic fluids on slopes. Journal of Non-Newtonian Fluid Mechanics 158 (1), 101–112.

Hough, S. E., 2005. Remotely triggered earthquakes following moderate mainshocks (or, why california is not falling into the ocean). Seismological Research Letters 76 (1), 58–66.

Hu, Y., Bürgmann, R., Uchida, N., Banerjee, P., Freymueller, J. T., 2016. Stress-driven relaxation of heterogeneous upper mantle and time-dependent afterslip following the 2011 tohoku earthquake. Journal of Geophysical Research: Solid Earth 121 (1), 385–411.

Igarashi, T., Matsuzawa, T., Hasegawa, A., 2003. Repeating earthquakes and interplate aseismic slip in the northeastern japan subduction zone. Journal of Geophysical Research: Solid Earth 108 (B5).

Igarashi, Toshihiro, T. M. A. H., 2002. The spatio-temporal change in the activity of the intermediate-depth earthquakes in the pacific plate beneath the northeastern japan arc [in japanese]. Zisin: J. Seismological Society of Japan 54, 465–474.

Ito, Y., Hino, R., Kido, M., Fujimoto, H., Osada, Y., Inazu, D., Ohta, Y., Iinuma, T., Ohzono, M., Miura, S., et al., 2013. Episodic slow slip events in the japan subduction zone before the 2011 tohoku-oki earthquake. Tectonophysics 600, 14–26.

Iverson, R. M., 1985. A constitutive equation for mass-movement behavior. The Journal of Geology, 143–160.

Iverson, R. M., Major, J. J., 1987. Rainfall, ground-water flow, and seasonal movement at minor creek landslide, northwestern california: Physical interpretation of empirical relations. Geological Society of America Bulletin 99 (4), 579–594.

Johnson, C. W., Bürgmann, R., Pollitz, F. F., 2015. Rare dynamic triggering of remote mâĽě 5.5 earthquakes from global catalog analysis. Journal of Geophysical Research: Solid Earth 120 (3), 1748–1761.

Jones, E., Oliphant, T., Peterson, P., et al., 2001–. SciPy: Open source scientific tools for Python.
URL http://www.scipy.org/

Kao, H., Wang, K., Dragert, H., Kao, J. Y., Rogers, G., 2010. Estimating seismic moment magnitude (mw) of tremor bursts in northern cascadia: Implications for the âĂIJseismic efficiencyâĂİ of episodic tremor and slip. Geophysical Research Letters 37 (19).

Kato, A., Obara, K., Igarashi, T., Tsuruoka, H., Nakagawa, S., Hirata, N., 2012. Propagation of slow slip leading up to the 2011 mw 9.0 tohoku-oki earthquake. Science 335 (6069), 705–708.

Katsumata, A., Kamaya, N., 2003. Low-frequency continuous tremor around the moho discontinuity away from volcanoes in the southwest japan. Geophysical Research Letters 30 (1).

Keefer, D., Johnson, A., 1983. Earth flows: morphology, mobilization, and movement. U.S. Geological Survey Professional Paper 1264, U.S. Geological Survey, Reston, Va.

Kelsey, H. M., 1978. Earthflows in franciscan melange, van duzen river basin, california. Geology 6 (6), 361–364.

Kiser, E., Ishii, M., 2013. Hidden aftershocks of the 2011 mw 9.0 tohoku, japan earthquake imaged with the backprojection method. Journal of Geophysical Research: Solid Earth 118 (10), 5564–5576.

Kita, S., 2009. Study for understanding generation mechanisms of intermediate-depth intraslab earthquakes beneath hokkaido and tohoku, northeastern japan. Ph.D thesis of Tohoku University.

Kita, S., Okada, T., Hasegawa, A., Nakajima, J., Matsuzawa, T., 2010a. Anomalous deepening of a seismic belt in the upper-plane of the double seismic zone in the pacific slab beneath the hokkaido corner: Possible evidence for thermal shielding caused by subducted forearc crust materials. Earth and Planetary Science Letters 290 (3), 415–426.

Kita, S., Okada, T., Hasegawa, A., Nakajima, J., Matsuzawa, T., 2010b. Existence of interplane earthquakes and neutral stress boundary between the upper and lower planes of the double seismic zone beneath tohoku and hokkaido, northeastern japan. Tectonophysics 496 (1), 68–82.

Korup, O., Densmore, A. L., Schlunegger, F., 2010. The role of landslides in mountain range evolution. Geomorphology 120 (1), 77–90.

Lay, T., Astiz, L., Kanamori, H., Christensen, D. H., 1989. Temporal variation of large intraplate earthquakes in coupled subduction zones. Physics of the earth and planetary interiors 54 (3-4), 258–312.

Lee, J., Strovers, B., Lin, V., 2007. C-20a/giii precision autopilot development in support of nasas uavsar program. In: Proceeding of the NASA Science Technology Conference 2007.

LeVeque, R. J., 2007. Finite difference methods for ordinary and partial differential equations: steady-state and time-dependent problems. Vol. 98. Siam.

Liu, K., Mei, C., 1990. Approximate equations for the slow spreading of a thin sheet of bingham plastic fluid. Physics of Fluids A: Fluid Dynamics (1989-1993) 2 (1), 30–36.

Lupini, J., Skinner, A., Vaughan, P., 1981. THE DRAINED RESIDUAL STRENGTH OF COHESIVE SOILS. GEOTECHNIQUE 31 (2), 181–213.

Mackey, B. H., Roering, J. J., 2011. Sediment yield, spatial characteristics, and the long-term evolution of active earthflows determined from airborne lidar and historical aerial photographs, eel river, california. Geological Society of America Bulletin 123 (7-8), 1560–1576.

Mainsant, G., Larose, E., Brönnimann, C., Jongmans, D., Michoud, C., Jaboyedoff, M., 2012. Ambient seismic noise monitoring of a clay landslide: Toward failure prediction. Journal of Geophysical Research: Earth Surface (2003–2012) 117 (F1).

Malet, J., Maquaire, O., 2003. Black marl earthflows mobility and long-term seasonal dynamic in southeastern france. In: Proc. 1st Int. Conf. on Fast Slope Movements. pp. 333–340.

Malet, J.-P., Maquaire, O., Calais, E., 2002. The use of global positioning system techniques for the continuous monitoring of landslides: application to the super-sauze earthflow (alpes-de-haute-provence, france). Geomorphology 43 (1), 33–54.

Marsan, D., Prono, E., Helmstetter, A., 2013. Monitoring aseismic forcing in fault zones using earthquake time series. Bulletin of the Seismological Society of America 103 (1), 169–179.

Matson, G., Hogg, A., 2007. Two-dimensional dam break flows of herschel–bulkley fluids: the approach to the arrested state. Journal of non-newtonian fluid mechanics 142 (1), 79–94.

Matthews, M. V., Reasenberg, P. A., 1988. Statistical methods for investigating quiescence and other temporal seismicity patterns. Pure and Applied Geophysics 126 (2), 357–372.

Mazzotti, S., Adams, J., 2004. Variability of near-term probability for the next great earthquake on the cascadia subduction zone. Bulletin of the Seismological Society of America 94 (5), 1954–1959.

Meehl, G. A., Stocker, T. F., Collins, W. D., Friedlingstein, P., Gaye, A. T., Gregory, J. M., Kitoh, A., Knutti, R., Murphy, J. M., Noda, A., et al., 2007. Global climate projections. In: IPCC, 2007: Climate Change 2007: the physical science basis. contribution of Working Group I to the Fourth Assessment Report of the Intergovernmental Panel on Climate Change. Vol. 3495. Cambridge University Press, pp. 747–845.

Mei, C., Liu, K.-F., Yuhi, M., 2001. Mud flowâĂŤslow and fast. In: Geomorphological fluid mechanics. Springer, pp. 548–577.

Mei, C. C., Yuhi, M., 2001. Slow flow of a bingham fluid in a shallow channel of finite width. Journal of Fluid Mechanics 431, 135–159.

Milillo, P., Fielding, E. J., Shulz, W. H., Delbridge, B., Burgmann, R., 2014. Cosmo-skymed spotlight interferometry over rural areas: The slumgullion landslide in colorado, usa. IEEE Journal of Selected Topics in Applied Earth Observations and Remote Sensing 7 (7), 2919–2926.

Minchew, B., Simons, M., Hensley, S., Björnsson, H., Pálsson, F., 2015. Early melt season velocity fields of langjökull and hofsjökull, central iceland. Journal of Glaciology 61 (226), 253.

Morlighem, M., Rignot, E., Seroussi, H., Larour, E., Ben Dhia, H., Aubry, D., 2011. A mass conservation approach for mapping glacier ice thickness. Geophysical Research Letters 38 (19).

Murray, J., Langbein, J., 2006. Slip on the san andreas fault at parkfield, california, over two earthquake cycles, and the implications for seismic hazard. Bulletin of the Seismological Society of America 96 (4B), S283–S303.

Murray, J., Segall, P., Cervelli, P., Prescott, W., Svarc, J., 2001. Inversion of gps data for spatially variable slip-rate on the san andreas fault near parkfield, ca. Geophysical research letters 28 (2), 359–362.

Nadeau, R. M., Dolenc, D., 2005. Nonvolcanic tremors deep beneath the san andreas fault. Science 307 (5708), 389–389.

Nadeau, R. M., Guilhem, A., 2009. Nonvolcanic tremor evolution and the san simeon and parkfield, california, earthquakes. science 325 (5937), 191–193.

Nadeau, R. M., Johnson, L. R., 1998. Seismological studies at parkfield vi: Moment release rates and estimates of source parameters for small repeating earthquakes. Bulletin of the Seismological Society of America 88 (3), 790–814.

Nadeau, R. M., McEvilly, T. V., 2004. Periodic pulsing of characteristic microearthquakes on the san andreas fault. Science 303 (5655), 220–222.

Nanjo, K., Ishibe, T., Tsuruoka, H., Schorlemmer, D., Ishigaki, Y., Hirata, N., 2010. Analysis of the completeness magnitude and seismic network coverage of japan. Bulletin of the Seismological Society of America 100 (6), 3261–3268.

Nishide, N., Hashimoto, T., Funasaki, J., Nakazawa, H., Oka, M., Ueno, H., Yamada, N., Sasakawa, I., Maeda, K., Sugimoto, K., et al., 2000. Nationwide activity of low-frequency earthquakes in the lower crust in japan. In: Abstr. Jpn. Earth and Planet. Sci. Joint Meeting, sk-p002.

Obara, K., 2002. Nonvolcanic deep tremor associated with subduction in southwest japan. Science 296 (5573), 1679–1681.

Obara, K., Hirose, H., 2006. Non-volcanic deep low-frequency tremors accompanying slow slips in the southwest japan subduction zone. Tectonophysics 417 (1), 33–51.

Obara, K., Hirose, H., Yamamizu, F., Kasahara, K., 2004. Episodic slow slip events accompanied by non-volcanic tremors in southwest japan subduction zone. Geophysical Research Letters 31 (23).

Obara, K., Kato, A., 2016. Connecting slow earthquakes to huge earthquakes. Science 353 (6296), 253–257.

Obara, K., Tanaka, S., Maeda, T., Matsuzawa, T., 2010. Depth-dependent activity of non-volcanic tremor in southwest japan. Geophysical Research Letters 37 (13).

Ogata, Y., 1992. Detection of precursory relative quiescence before great earthquakes through a statistical model. Journal of Geophysical Research: Solid Earth 97 (B13), 19845–19871.

Ohmi, S., Obara, K., 2002. Deep low-frequency earthquakes beneath the focal region of the mw 6.7 2000 western tottori earthquake. Geophysical research letters 29 (16).

Okada, Y., 1985. Surface deformation due to shear and tensile faults in a half-space. Bulletin of the seismological society of America 75 (4), 1135–1154.

Parise, M., Guzzi, R., 1992. Volume and shape of the active and inactive parts of the slumgullion landslide, hinsdale county, colorado. Open-File Report 92-216, US Department of the Interior, US Geological Survey.

Peng, Z., Gomberg, J., 2010. An integrated perspective of the continuum between earthquakes and slow-slip phenomena. Nature Geoscience 3 (9), 599–607.

Pollitz, F. F., Stein, R. S., Sevilgen, V., Bürgmann, R., 2012. The 11 april 2012 east indian ocean earthquake triggered large aftershocks worldwide. Nature 490 (7419), 250.

Rasmussen, L., 1988. Bed topography and mass-balance distribution of columbia glacier, alaska, usa, determined from sequential aerial photography. J. Glaciol 34 (117), 208–216.

Reasenberg, P. A., Simpson, R. W., 1992. Response of regional seismicity to the static stress change produced by the loma prieta earthquake. Science 255 (5052), 1687.

Rodriguez, E., Martin, J., 1992. Theory and design of interferometric synthetic aperture radars. In: Radar and Signal Processing, IEE Proceedings F. Vol. 139. IET, pp. 147–159.

Roering, J. J., Stimely, L. L., Mackey, B. H., Schmidt, D. A., 2009. Using dinsar, airborne lidar, and archival air photos to quantify landsliding and sediment transport. Geophysical Research Letters 36 (19).

Rogers, G., Dragert, H., 2003. Episodic tremor and slip on the cascadia subduction zone: The chatter of silent slip. Science 300 (5627), 1942–1943.

Rubinstein, J. L., La Rocca, M., Vidale, J. E., Creager, K. C., Wech, A. G., 2008. Tidal modulation of nonvolcanic tremor. Science 319 (5860), 186–189.
URL http://science.sciencemag.org/content/319/5860/186

Rubinstein, J. L., Vidale, J. E., Gomberg, J., Bodin, P., Creager, K. C., Malone, S. D., 2007. Non-volcanic tremor driven by large transient shear stresses. Nature 448 (7153), 579.

Schulz, W., Coe, J., Shurtleff, B., Panosky, J., Farina, P., Ricci, P., Barsacchi, G., 2012. Kinematics of the slumgullion landslide revealed by ground-based insar surveys. In: Landslides and Engineered Slopes: Protecting Society through Improved Understanding–Proc. of the 11th International and 2nd North American Symposium on Landslides and Engineered Slopes. pp. 1273–1279.

Schulz, W. H., Kean, J. W., Wang, G., 2009a. Landslide movement in southwest colorado triggered by atmospheric tides. Nature Geoscience 2 (12), 863–866.

Schulz, W. H., McKenna, J. P., Biavati, G., Kibler, J. D., 2007. Characteristics of slumgullion landslide inferred from subsurface exploration, in-situ and laboratory testing, and monitoring. In: Proceedings of the 1st North American Landslide Conference, Vail, Colorado, June. pp. 3–8.

Schulz, W. H., McKenna, J. P., Kibler, J. D., Biavati, G., 2009b. Relations between hydrology and velocity of a continuously moving landslideï£¡evidence of pore-pressure feedback regulating landslide motion? Landslides 6 (3), 181–190.

Schwartz, S. Y., Rokosky, J. M., 2007. Slow slip events and seismic tremor at circum-pacific subduction zones. Reviews of Geophysics 45 (3).

Shelly, D. R., 2009. Possible deep fault slip preceding the 2004 parkfield earthquake, inferred from detailed observations of tectonic tremor. Geophysical Research Letters 36 (17).

Shelly, D. R., 2017. A 15 year catalog of more than 1 million low-frequency earthquakes: Tracking tremor and slip along the deep san andreas fault. Journal of Geophysical Research: Solid Earth 122 (5), 3739–3753.

Shelly, D. R., Beroza, G. C., Ide, S., 2007. Non-volcanic tremor and low-frequency earthquake swarms. Nature 446 (7133), 305–307.

Shelly, D. R., Beroza, G. C., Ide, S., Nakamula, S., 2006. Low-frequency earthquakes in shikoku, japan, and their relationship to episodic tremor and slip. Nature 442 (7099), 188.

Shelly, D. R., Johnson, K. M., 2011. Tremor reveals stress shadowing, deep postseismic creep, and depth-dependent slip recurrence on the lower-crustal san andreas fault near parkfield. Geophysical Research Letters 38 (13), n/a–n/a, l13312.
URL http://dx.doi.org/10.1029/2011GL047863

Smith, W., 1993. Photogrammetric determination of movement on the slumgullion slide, hinsdale county, colorado. Open-File Report 93-597, US Department of the Interior, US Geological Survey.

Swanson, F. J., Swanston, D. N., 1977. 6 complex mass-movement terrains in the western cascade range, oregon. Reviews in Engineering Geology 3, 113–124.

Ter-Stepanian, G., 1965. In-situ determination of the rheological characteristics of soils on slopes. In: Proc. 6th Int. Conf. on Soil Mechanics and Foundation Engineering. Vol. 2. pp. 575–577.

Thatcher, W., B., R. J., 1984. A viscoelastic coupling model for the cyclic deformation due to periodically repeated earthquakes at subduction zones. J.Geophys. Res. 89, 7631–7640.

Thomas, Amanda M., N., M., R., Burgmann, R., 2009. Tremor-tide correlations and near-lithostatic pore pressure on the deep san andreas fault. Nature 462.

Thomas, A. M., N. M. B. Q. B. R. B., Shelly, D. R., 2017. Using low frequency earthquake families on the san andreas fault as deep creepmeters. Journal of Geophysical Research.

Thompson, B., 2014. okada$_{w}rapper.GithubRepository$.

Trotter, C. M., 1993. Weathering and regolith properties at an earthflow site. Quarterly Journal of Engineering Geology and Hydrogeology 26 (3), 163–178.

Uchida, N., Iinuma, T., Nadeau, R. M., Bürgmann, R., Hino, R., 2016. Periodic slow slip triggers megathrust zone earthquakes in northeastern japan. Science 351 (6272), 488–492.

Uchida, N., Matsuzawa, T., 2013. Pre-and postseismic slow slip surrounding the 2011 tohoku-oki earthquake rupture. Earth and Planetary Science Letters 374, 81–91.

Uchida, N., Matsuzawa, T., Hasegawa, A., Igarashi, T., 2003. Interplate quasi-static slip off sanriku, ne japan, estimated from repeating earthquakes. Geophysical Research Letters 30 (15).

Uchida, N., Yui, S., Miura, S., Matsuzawa, T., Hasegawa, A., Motoya, Y., Kasahara, M., 2009. Quasi-static slip on the plate boundary associated with the 2003 m8. 0 tokachi-oki and 2004 m7. 1 off-kushiro earthquakes, japan. Gondwana Research 16 (3), 527–533.

Van Asch, T. J., Van Genuchten, P., 1990. A comparison between theoretical and measured creep profiles of landslides. Geomorphology 3 (1), 45–55.

Van Asch, T. W., Malet, J., Bogaard, T., et al., 2009. The effect of groundwater fluctuations on the velocity pattern of slow-moving landslides. Nat Hazards Earth Syst Sci 9, 739–749.

Van Zyl, J. J., 2001. The shuttle radar topography mission (srtm): a breakthrough in remote sensing of topography. Acta Astronautica 48 (5-12), 559–565.

Varnes, D., Savage, W., 1996. The slumgullion earthflow: A large-scale natural laboratory. U.S. Geological Survey Bulletin 2130, U.S. Geological Survey, Reston, Va.

Wiemer, S., Katsumata, K., 1999. Spatial variability of seismicity parameters in aftershock zones. Journal of Geophysical Research: Solid Earth 104 (B6), 13135–13151.

Wiemer, S., Wyss, M., 2000. Minimum magnitude of completeness in earthquake catalogs: Examples from alaska, the western united states, and japan. Bulletin of the Seismological Society of America 90 (4), 859–869.

Williams, R. A., Pratt, T. L., 1996. Detection of the base of slumgullion landslide, colorado, by seismic reflection and refraction methods. The Slumgullion Earth Flow: A Large-Scale Natural Laboratory, US Geological Survey Bulletin 2130.

Winter, M., Dixon, N., Wasowski, J., Dijkstra, T., 2010. Introduction to land-use and climate change impacts on landslides. Quarterly Journal of Engineering Geology and Hydrogeology 43 (4), 367–370.

Witze, A., 2015. Mappers rush to pinpoint landslide risk in nepal. Nature News, 133 – 133.
URL http://www.nature.com/news/mappers-rush-to-pinpoint-landslide-risk-in-nepal-1.17525?WT.mc_id=TWT_NatureNews

Yu, B., Wu, Y., Chu, S., 2014. Preliminary study of the effect of earthquakes on the rainfall threshold of debris flows. Engineering Geology 182, Part B (0), 130 – 135, special Issue on The Long-Term Geologic Hazards in Areas Struck by Large-Magnitude Earthquakes.
URL http://www.sciencedirect.com/science/article/pii/S001379521400088X

Zhao, D., Matsuzawa, T., Hasegawa, A., 1997. Morphology of the subducting slab boundary in the northeastern japan arc. Physics of the Earth and Planetary Interiors 102 (1-2), 89–104.